

AD-A124 428

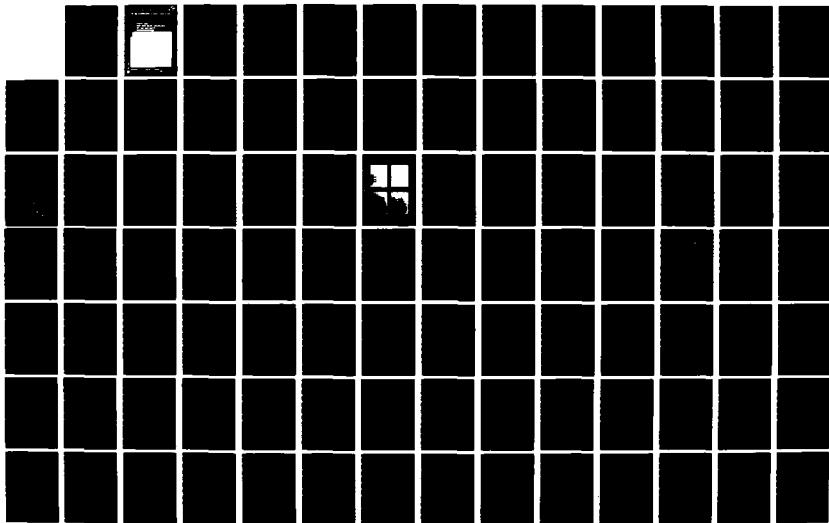
SWEPT LINE ELECTRON BEAM ANNEALING OF ION IMPLANTED
SEMICONDUCTORS(U) ILLINOIS UNIV AT URBANA COORDINATED
SCIENCE LAB K J SODA JUL 82 R-958 N00014-79-C-0424

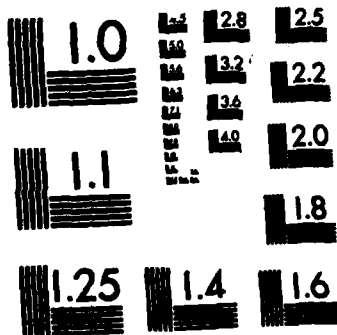
1/2

UNCLASSIFIED

F/G 28/12

NL





MICROCOPY RESOLUTION TEST CHART
NATIONAL BUREAU OF STANDARDS-1963-A

ADA 124428

REPORT DOCUMENTATION PAGE		READ INSTRUCTIONS BEFORE COMPLETING FORM
1. REPORT NUMBER	2. GOVT ACCESSION NO. AD-A124428	3. RECIPIENT'S CATALOG NUMBER
4. TITLE (and Subtitle) SWEEP LINE ELECTRON BEAM ANNEALING OF ION IMPLANTED SEMICONDUCTORS		5. TYPE OF REPORT & PERIOD COVERED Technical Report
7. AUTHOR(s) Kenneth James Soda		6. PERFORMING ORG. REPORT NUMBER R-950 / UILU-ENG 82-2216
8. PERFORMING ORGANIZATION NAME AND ADDRESS Coordinated Science Laboratory University of Illinois 1101 W. Springfield Ave. Urbana, IL 61801		9. CONTRACT OR GRANT NUMBER(s) JSEP-N00014-79-C-0424 ARO-DAAG-29-80-C-0011
11. CONTROLLING OFFICE NAME AND ADDRESS Joint Services Electronics Program Army Research Office		10. PROGRAM ELEMENT, PROJECT, TASK AREA & WORK UNIT NUMBERS
14. MONITORING AGENCY NAME & ADDRESS (if different from Controlling Office)		12. REPORT DATE July, 1982
		13. NUMBER OF PAGES 122
		15. SECURITY CLASS. (of this report) Unclassified
		15a. DECLASSIFICATION/DOWNGRADING SCHEDULE
16. DISTRIBUTION STATEMENT (of this Report) Approved for public release; distribution unlimited.		
17. DISTRIBUTION STATEMENT (of the abstract entered in Block 20, if different from Report)		
18. SUPPLEMENTARY NOTES		
19. KEY WORDS (Continue on reverse side if necessary and identify by block number) Electron Beam Annealing Ion-Implantation		
20. ABSTRACT (Continue on reverse side if necessary and identify by block number) The capabilities of a Swept Line Electron Beam (SLEB) in annealing ion-implanted semiconductors are examined. This technique employs a fixed geometry, line-shaped electron beam through which implanted samples are mechanically scanned. In general, this technique can produce annealing results comparable or superior to those achievable by conventional furnace annealing. Residual point defects in self-implanted amorphous silicon treated by SLEB and furnace processes are examined by Deep Level Transient Spectroscopy.		

20. Despite high temperature treatment, furnace annealed samples show large (10^{16} cm^{-3}) defect concentrations and dopant migration phenomena. This is especially true in the as-implanted amorphous-crystalline transition region. When proper annealing parameters are used, SLEB annealed material shows much reduced point defect concentrations and reduced dopant motion. These relatively thick amorphous layers ($0.5 \mu\text{m}$) are regrown and annealed by SLEB without the use of additional furnace treatment.

Similar studies of BF_2^+ implanted silicon are also presented. Differential resistivity/Hall effect and Secondary Ion Mass Spectrometry analysis are used to show improved electrical activation and only limited dopant motion during SLEB annealing as compared with furnace annealing. The improved electrical activity is especially significant in the original amorphous-crystalline transition region where reduced residual defect densities are observed.

SLEB annealing effectiveness in both direct and indirect band gap composition $\text{GaAs}_{1-x}\text{P}_x$ is also investigated. Photoluminescence emission from nitrogen implanted, beam annealed material is found to be comparable or larger in intensity when compared with optimally prepared furnace annealed material. Photoluminescence profiling and p-n junction studies show that migration of implanted nitrogen and related damage can be limited to the as-implanted profile when SLEB annealing is used.

SWEPT LINE ELECTRON BEAM ANNEALING OF ION-IMPLANTED SEMICONDUCTORS

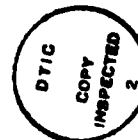
by

Kenneth James Soda

This work was supported by the Joint Services Electronics Program
(U. S. Army, U. S. Navy and U. S. Air Force) under Contract No. N00014-
79-C-0424 and by the Army Research Office under Contract DAAG-29-80-C-0011.

Reproduction in whole or in part is permitted for any purpose of the
United States Government.

Approved for public release. Distribution unlimited.



Accession For	
DTIC GRAAI	
DTIC TAB	
Unannounced	
Justification	
By	
Distribution/	
Availability Codes	
Dist	Avail: and/or Special
A	

**SWEPT LINE ELECTRON
BEAM ANNEALING OF
ION-IMPLANTED SEMICONDUCTORS**

BY

KENNETH JAMES SODA

**B.S., United States Air Force Academy, 1973
M.S., University of California, 1974**

THESIS

**Submitted in partial fulfillment of the requirements
for the degree of Doctor of Philosophy in Electrical Engineering
in the Graduate College of the
University of Illinois at Urbana-Champaign, 1982**

Urbana, Illinois

SWEPT LINE ELECTRON BEAM ANNEALING OF ION-IMPLANTED SEMICONDUCTORS

Kenneth J. Soda, Ph.D.
Coordinated Science Laboratory and
Department of Electrical Engineering
University of Illinois at Urbana-Champaign, 1982

The capabilities of a Swept Line Electron Beam (SLEB) in annealing ion-implanted semiconductors are examined. This technique employs a fixed geometry, line-shaped electron beam through which implanted samples are mechanically scanned. In general, this technique can produce annealing results comparable or superior to those achievable by conventional furnace annealing.

Residual point defects in self-implanted amorphous silicon treated by SLEB and furnace processes are examined by Deep Level Transient Spectroscopy. Despite high temperature treatment, furnace annealed samples show large (10^{16} cm^{-3}) defect concentrations and dopant migration phenomena. This is especially true in the as-implanted amorphous-crystalline transition region. When proper annealing parameters are used, SLEB annealed material shows much reduced point defect concentrations and reduced dopant motion. These relatively thick amorphous layers ($0.5 \mu\text{m}$) are regrown and annealed by SLEB without the use of additional furnace treatment.

Similar studies of BF_2^+ implanted silicon are also presented. Differential resistivity/Hall effect and Secondary Ion Mass Spectrometry analysis are used to show improved electrical activation and only limited dopant motion during SLEB annealing as compared with furnace annealing. The improved electrical activity is especially significant in the original amorphous-crystalline transition region where reduced residual defect densities are observed.

SLEB annealing effectiveness in both direct and indirect band gap composition $\text{GaAs}_{1-x}\text{P}_x$ is also investigated. Photoluminescence emission from nitrogen implanted, beam annealed material is found to be comparable or larger in intensity when compared with optimally prepared furnace annealed material. Photoluminescence profiling and p-n junction studies show that migration of implanted nitrogen and related damage can be limited to the as-implanted profile when SLEB annealing is used.

ACKNOWLEDGEMENTS

The author gratefully acknowledges the support, guidance and encouragement provided by Professor B. G. Streetman which made this effort possible. I am especially grateful for the two great lessons he helped me learn from this experience; to pursue research independently and to write clearly and concisely.

I also thank Professor K. Hess for his theoretical insight and illuminating discussions. For their kind assistance and advice I thank Professor G. E. Stillman and Professor J. E. Greene.

I gratefully acknowledge the contributions of those with whom I have co-authored papers related to this thesis: Dr. T. Yu, R. Y. DeJule, V. Iyer and Dr. S. S. Chan. For their assistance and friendship I thank my colleagues Dr. M. J. Helix, Dr. M. Y. Tsai, Dr. D. S. Day, Dr. J. Oberstar, P. A. Martin, B. Seymour, Dr. S. Shichijo and J. E. Baker.

I owe a special debt of gratitude to my colleague and friend N. Vassos, of the Special Processing Laboratory, whose cooperation was essential to this effort. His lessons of practical experimental techniques are among the most valuable I take away from this experience. Many thanks also to the other members of the Coordinated Science Laboratory professional staff for expert machining, photography, drafting, electronic repair and typing. For their assistance with electron microscopy, I thank the members of the Materials Research Laboratory professional staff.

For his assistance in the preparation of this manuscript, I thank T. G. Ryan of the Rome Air Development Center.

Finally, my special thanks to my wife Nancy and our children Elizabeth and Jennifer for their support, patience and love.

TABLE OF CONTENTS

CHAPTER	PAGE
1. INTRODUCTION	1
1.1 Overview of Beam Processing Technology	1
1.2 Beam-Solid Interactions	3
1.3 Trends in Beam Processing Technology	9
2. EXPERIMENTAL PROCEDURES	13
2.1 Swept Line Electron Beam System	13
2.2 Ion-Implantation	16
2.3 Methods of Characterization	18
2.3.1 SEM Channeling Pattern Analysis	18
2.3.2 Deep Level Transient Spectroscopy	24
2.3.2.1 Overview and Apparatus Description	24
2.3.2.2 DLTS Data Analysis	28
2.3.3 Differential Resistivity and Hall Effect Measurements	31
3. SLEB ANNEALING OF Si^+ -IMPLANTED AMORPHOUS SILICON	34
3.1 Experimental Procedure	37
3.2 Results and Discussion	38
3.3 Conclusions	49
4. SLEB ANNEALING OF BF_2^+ IMPLANTED SILICON	51
4.1 Experimental Procedure	51
4.2 Results	52
4.3 Discussions	58
4.4 Conclusions	63
5. SLEB ANNEALING OF $\text{GaAs}_{1-x}\text{P}_x$	65
5.1 Study of SLEB Annealed $\text{GaAs}_{1-x}\text{P}_x$:N by Photo- luminescence	65
5.1.1 Experimental Procedures	65
5.1.2 Results and Discussion	67
5.1.2.1 Direct Gap Composition, $x = 0.40$	67
5.1.2.2 Indirect Gap Composition, $x = 0.50$	70
5.1.2.3 Indirect Gap Composition, $x = 0.65$	71
5.1.2.4 Optical Depth Profiling	71

5.2	Study of SLEB Annealed GaAs _{0.35} P _{0.65} p-n Junctions . . .	77
5.2.1	Experimental Procedure	77
5.2.2	Results and Discussion: Electrical Characteristics	80
5.2.3	Results and Discussion: Light Emission Characteristics	88
5.3	Summary and Conclusions.	91
6.	SUMMARY AND RECOMMENDATIONS	93
	APPENDIX TRAPSI Program Documentation.	95
	REFERENCES	112
	VITA	122

1. INTRODUCTION

1.1 Overview of Beam Processing Technology

The use of concentrated beams of photons, electrons or ions to prepare semiconductor material has recently become an area of intense research. Although lasers have provided other industrial applications for many years, beam techniques have only recently demonstrated the potential to revolutionize semiconductor device fabrication. In this section, I outline recent developments and applications of beam processing, point out major trends and describe the relationship of my research to the mainstream of technology.

The techniques used for beam processing are distinguished by their beam source and method by which the beam energy is directed onto the semiconductor. To date, six beam processing techniques have been studied. These employ pulsed lasers (PL), raster scanned CW lasers (CWL), pulsed ion beams (PI), area pulsed electron beams (PEB), raster scanned (RSEB) or multi-scanned electron beams (MSEB), and swept line electron beams (SLEB). A general overview of experimental processing parameters is presented in Figure 1.1. Here total average incident energy density is plotted against process duration. In cases of multiple scanning, energy density is summed after many passes by the beam. Data here are by no means all inclusive, but reflect the general range of each processing technique. Several trends are noteworthy. First, there is a tremendous span over which successful beam processing applications have occurred; eleven orders of magnitude in time, seven orders in energy density. Much of the initial experimentation has concentrated on pulsed techniques, particularly pulsed lasers and the SPIRE area PEB machine. (See lower left of Figure 1.1.) Processing is generally

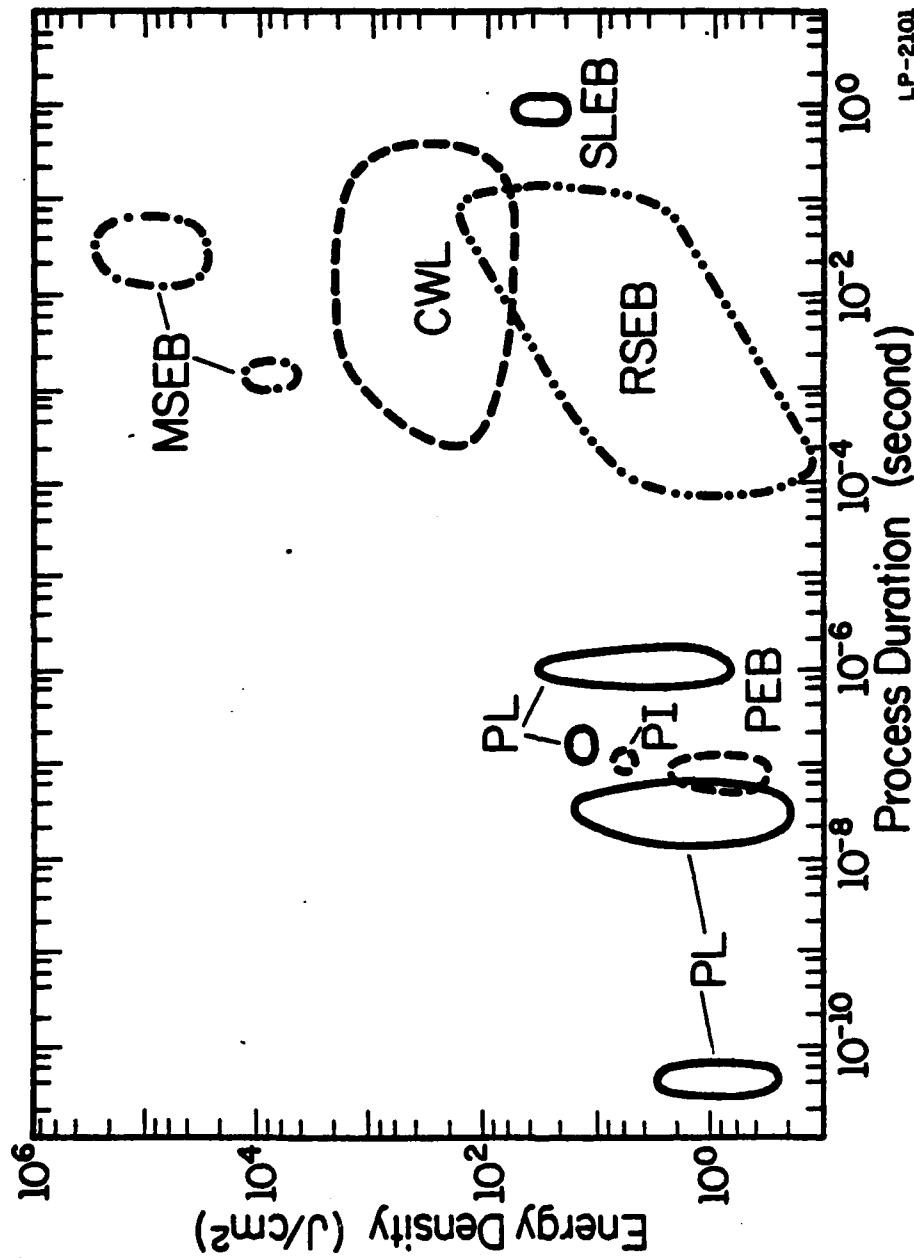


Fig. 1.1. Representative energy density versus process duration parameters for the six major types of semiconductor beam processing. These techniques use: PL - Pulsed Lasers; PEB - Pulsed Electron Beams; PI - Pulsed Ion Beams; MSEB/SLEB - Multi or Raster Scanned Electron Beams; CWL - Continuous Wave Lasers; and SLEB - Swept-Line Electron Beams. Note the eleven order of magnitude range in process duration and seven order of magnitude range in energy density.

performed in a single pulse, thus limiting experimental parameters to the characteristic laser or electron discharge decay. In more recent studies, scanned continuous lasers and electron beams (MSEL, SLEB, CWL) expand the range of study. Scanning speed and repetition rate enter as additional parameters and extend incident energy densities 1000 fold, and process duration 100,000 times.

By far the most widely studied application for all types of beam processing is the annealing of ion-implanted layers in semiconductors. Other applications include induced crystallization of amorphous and polycrystalline layers, pulsed diffusion of dopants directly from a surface layer, contact formation, growth and Q_{ss} reduction in oxides, surface smoothing, circuit customizing, trimming of thin films, scribing device chips, drilling and mesa formation. Recently, beam processing techniques have improved to the point that device fabrication has been attempted. To date, resistors, capacitors, diodes, bipolar transistors, MOSFETs, and solar cells have been fabricated with varying degrees of success. A representative sample of processing applications is presented in Table 1.1.

1.2 Beam-Semiconductor Interactions

Interaction of photons and electrons in solids is in itself an area of active research. However, it is appropriate that we review in general terms the important aspects of photon and electron energy deposition in semiconductors [51-53]. There are three areas of concern: energy deposition depth profile, parameters which affect this profile, and beam-induced effects.

Photons (0.1 - 5.0 eV) transfer energy to a crystalline lattice through induced vibrations of valence electrons. Reflection arises from

TABLE 1.1

EXAMPLES OF BEAM PROCESSING APPLICATIONS

APPLICATION	PROCESS USED	REMARKS	REFERENCES
-Annealing of Ion- Implantation Induced Damage/Dopant Activation			
* Si Crystal Substrates			
**Implanted Species			
In,Al,Ga,P,As,B	Ruby PL		1-4
Ga,Ge,As,Se,In,Sb	Nd:Yag PL		5
Sn,Te,Bi,P,As	CO ₂ CWL	MeV Ion-Implants	6
As	Argon CWL	EBIC Damage Invest.	7,8
B	Krypton CWL		8
P,As,B	MSEB		9-11
* Si Polycrystal			
**Dopant			
B	Dye PL		12
P	Ruby PL		13
* GaAs Crystal Substrates			
**Implanted Species			
Te,Si,Se,Kr,Zn,Mg	Ruby PL		14-21
Si,Te,Se,Kr,Be	SPIRE PEB		16-18,23
-Recrystallization of Silicon			
	Ruby PL	Deposited Si on Xtal	24
	ND:Yag PL	Deposited Si on Xtal & Poly-xtal Subst.	25-27
	Argon CWL	Deposited Si on Xtal, Lateral Epitaxy	8,28-30
	Spire PEB	Deposited Si on Xtal	24
	SLEB	Ion-Implanted Si	31
-Direct Doping from a Surface Layer			
*Si Substrates	CO ₂ CWL	Photo-Induced Zone Migration	32
*GaAs Substrates	SPIRE PEB	From AsSe Layers	33

TABLE 1.1 (Continued)

APPLICATION	PROCESS USED	REMARKS	REFERENCES
-Contact Preparation			
*In Silicon	Ruby PL	Si/CoSi ₂ /Si Contacts	34
	ArgonCWL		8
	PEB, MSEB	Al Contacts	35
*In GaAs	Nd:Yag,		
	Ruby PL	Au:Ge Contacts	36
	Argon CWL	In-Au:Ge Contacts	37
-Beam Induced Oxide Growth			
*Si:SiO ₂ , Si ₃ N ₄	Argon CWL	O,N,C Implanted Si	38
*GaAs:Ga ₂ O ₃	Argon CWL		39
-Oxide Charge Reduction In SiO ₂	Argon CWL		8
-Device Fabrication			
*Si Diodes	Ruby PL		10
	Nd:Yag PL		40
	Argon CWL		40,41
	MSEB		10,42
	PEB		40
*Si Bipolar Transistors	Ruby PL	B,As,P Implanted	46
*Si MOSFETs	Nd:Yag PL	On Poly-Silicon	27
	Argon CWL	Ion-Implanted on Xtal	47
	MSEB	" " "	48
*Si Solar Cells	Ruby PL	P ⁺ Ion-Implanted	49
	Ruby PL	Pulsed Diffused	50

partial reradiation by excited electrons. The remaining energy is transferred to the lattice via electron-atom collisions. For normal incidence, power density absorbed at a depth z in a one dimensional semi-infinite sample illuminated by a beam of intensity I_0 is given by:

$$\phi(z) = I_0(1-R)\alpha e^{-\alpha z} \quad (1.1)$$

where R is the fraction of photons reflected and α the absorption coefficient. Electrons (5-50 keV), on the other hand, may interact either elastically with the atomic nuclei, or inelastically with local electrons. The elastically scattered (backscattered) electrons can reemerge from the sample with as much as 50% of the energy of the incident beam. Inelastically scattered electrons are usually modeled as losing their energy to the lattice in a continuous scattering process:

$$-dE/ds \propto (n_e/E_0) \ln(E_0/J) \quad (1.2)$$

where E_0 is the incident electron energy, n_e is the total density of electrons and J the ionization potential of the material. This formulation applies along the path of each beam electron. Since each electron is scattered many times, deposited energy depth profiles must account for deviation in the electron trajectory due to each collision. The results of these calculations are truncated pseudo-gaussian[52,53] distributions which are relatively independent of the beam energy when plotted as a percentage of extrapolated electron range [53]. For silicon, this range is given by:

$$R_g = 4.57 E_0^{1.75} \quad (1.3)$$

where E_0 is the electron energy in keV, and the R_g is given per unit density of the target material in $\mu\text{g}/\text{cm}^2$. The energy loss distributions become more skewed towards the surface of the sample as the atomic number of the target increases [52].

The probability of photon absorption is related to the density of available initial and final states of a valence electron transition. Hence, both photon absorption and reflection coefficients depend strongly upon the photon wavelength and sample temperature. In crystalline silicon, for example, α has a value of about 10^6 cm^{-1} at wavelengths shorter than $0.4 \text{ }\mu\text{m}$ then falls rapidly to a few times 10^2 cm^{-1} at $2 \text{ }\mu\text{m}$, as the corresponding photon energy falls below bandgap. Most semiconductor bandgaps decrease with increases in temperature, causing the drop off in α to occur at longer λ . The degree to which a sample may have heavy disorder or ion-implantation induced damage will also increase absorption. As indicated in Eqns. 1.1 and 1.2, electron power absorption is generally only effected by material density and atomic number, with far less sensitivity to temperature. In the same way, the backscatter efficiency (η) depends primarily upon the atomic number of the target.

Figure 1.2 demonstrates the relative absorbed power density profiles in crystalline silicon for a 1 J/cm^2 flux of 2.3 eV photons and 20 keV electrons. These energies are typical of beam processing experiments. The photon profile is based upon Eqn. 1.1 with $R = 0.37$ and $\alpha = 8 \times 10^3 \text{ cm}^{-1}$ while the electron profile uses $\eta = 0.174$ and the experimentally verified energy dissipation distributions of Everhart and Hoff [53]. Although the overall depth of penetration is nearly equal, the power dissipated by electrons exceeds that of photons for most of the profile.

Under more intense laser illumination, semiconductor materials display beam-induced effects which significantly affect energy absorption [51]. Free carriers generated by the photon flux can become numerous enough to increase α by direct absorption. At higher energy densities, these

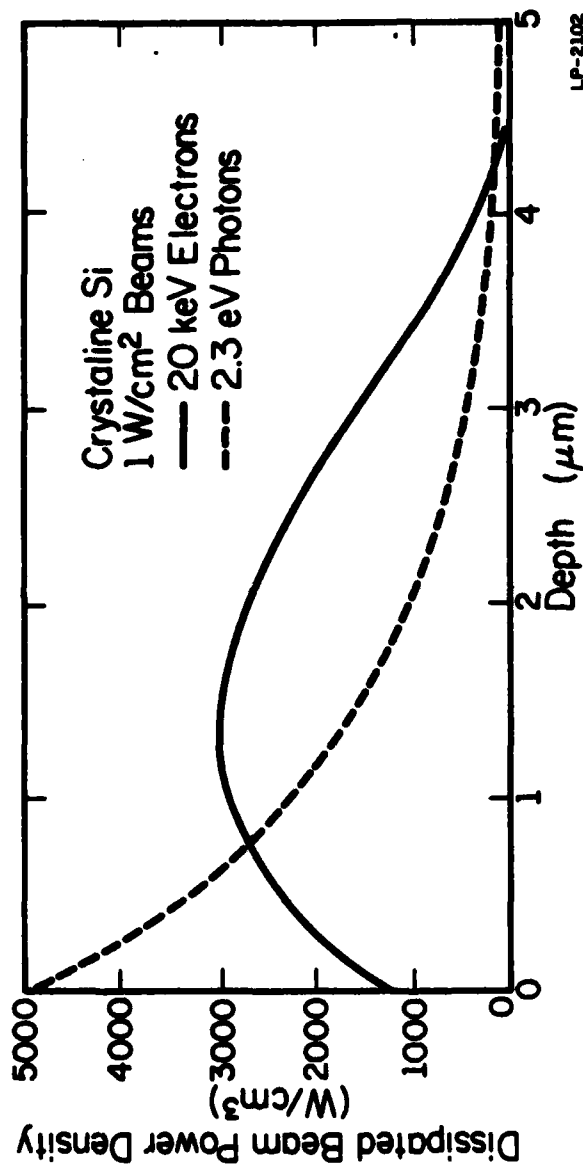


Fig. 1.2. Theoretical energy deposition profiles for 1 W/cm^2 beams of 20 keV electrons and 2.3 eV photons in crystalline silicon. Notice that in the electron beam case, the peak value of energy deposition occurs well within the sample.

carriers can produce impact ionized carriers, further increasing α . If the photons are delivered in a short pulse, electron-hole densities can become high enough to create a reflecting plasma. These hot carriers can also diffuse from the surface, significantly affecting the absorbed power profile. If heated beyond the melting point, both α and R increase, due to the metallic nature of the molten state. Since electron power absorption does not depend upon the density of electron states in the target, analogous high power effects are not significant for electron beams. Photons used in some beam processes have wavelengths equal to major fractional parts of the thickness of dielectric coatings. The result can be constructive interference and severe localized heating. Corresponding electron-dielectric effects are not possible in the scale of integrated circuit structures.

1.3 Trends in Beam Processing Technology

Semiconductor beam processing technology is still very much in a developmental state. However, enough is known about the characteristics of each technique to predict its ultimate industrial applicability. The requirements of each application will be the deciding factor.

Activation of ion-implanted dopants in single crystal semiconductors, although the most studied application, places the most severe restrictions on beam technology. Activation of the implanted species must be efficient. Residual defect concentrations must be low. Conventional sample heating either during or after beam treatment is not desirable. Although most beam processing techniques have achieved activation of dopants, a number of recent studies indicate that pulsed techniques, in which the semiconductor actually melts, produce residual defects which cannot be eliminated without post-processing furnace annealing. One might therefore imagine that

any fast melt-refreeze process would leave residual disorder at the point of furthest advance of the melt front. This seems to be borne out by recent research.

Bentini et al. [54] have demonstrated that MSEB solid phase re-growth in phosphorus implanted silicon produces better minority carrier diffusion lengths than both PEB and melt phase ruby PL processing. Anderson et al. [17] use differential resistivity techniques to demonstrate consistently larger mobility in implanted GaAs layers when CW lasers are employed. Ruby and Nd:YAG PL and the SPIRE PEB machine were compared with argon and Nd:YAG CWL. They suggest that rapid solidification may be accompanied by large concentrations of antistructural defects. They also suggest that highly non-stoichiometric regions can be created by melt phase induced arsenic evolution. Direct evaluation of defects after both melt and solid phase processing has been performed by Benton et al. [55]. DLTS studies on B^+ and As^+ implanted silicon show as many as 100 times (10^{11} vs. 10^{13} cm^{-3}) more residual defects in Nd:YAG PL as in CO_2 CWL processed diodes. In a separate study, Benton et al. [56] use DLTS and TSCAP to identify defects in single crystal material generated directly by Nd:YAG PL induced melting. Boroffka et al. [10] have studied leakage currents in arsenic implanted silicon diodes prepared by ruby PL and scanned e-beam. They observe consistently smaller leakage by the solid phase e-beam process. Likewise, Sandow [40] reports superior I-V characteristics in arsenic implanted, argon CWL annealed diodes compared with both pulsed Nd:YAG and PEB processed devices. He suggests that the differences are due to large concentrations of residual defects remaining after the pulsed processing.

As one might expect, melt phase processing is accompanied by rapid redistribution of dopants [57,58]. This characteristic is not desirable in cases where special profiles have been established by multiple implantation, or where great control of the junction depth is necessary. This taken with the evidence about junction defects makes it unlikely that pulsed beam technology will replace standard furnace diffusion or annealing in applications where high quality or tailored profiles are required. Continuous wave lasers and multi-scanned or swept-line electron beams are the most likely candidates for this application.

In devices requiring dielectric coatings, unintentional spot heating due to laser interference effects can have a devastating effect on surface morphology [59]. These effects are not expected for electron processes. In addition, raster scanned CWL techniques have been shown to produce nonuniformities in annealing quality on the scale of the beam spot. Mizuta et al. [60] have studied As^+ implanted CWL annealed silicon by electron beam induced current (EBIC) analysis. They observe reduced minority carrier charge collection efficiency in banded patterns parallel to the direction of travel of the beam spot. These bands are attributed to laser induced defects formed in uneven patterns beneath the implanted layer. Since spot sizes were of the order of microns, such banding can have serious effects on the characteristics of planar devices. Recently Sheng et al. [7] have extended this EBIC study to include raster scanned electron beam annealing. They demonstrate that the RSEB technique produces even less residual damage than argon CWL treatment, without the banded damage regions.

The facts outlined above seem to indicate the general suitability of electron beams for processing semiconductor material of integrated circuit complexity. When other practical considerations are taken into account, the

SLEB technique has some merit over other electron beam systems. This method relies on a fixed line geometry beam, below which samples are translated mechanically. The requirements for scanning electronics are eliminated as are concerns for maintenance of precise focusing. On an industrial scale, wafer processing speed should be no slower than by pulsed beam processes, since mechanical translation will ultimately limit any automated beam process. Waiting time for system charging is also eliminated since the beam will run in continuous fashion.

In this work, I have explored in some detail the ability of the SLEB technique to reduce residual defects in amorphous layers and to activate ion-implanted dopants and traps. It will be demonstrated that future industrial requirements for high quality junctions are indeed met by this technique.

I do not contend that pulsed melt phase processes will be without future application. E-beam pulsed diffusion or implanted layer annealing may prove important for majority carrier devices where defects are not of concern. Since photon energy absorption can be extremely shallow, the entire area of contacts remains fertile ground for PL techniques. However, at the relative power densities and speeds at which lasers can be directed, I feel it unlikely that rastered laser techniques will ultimately be used to process devices of substantial area. Even scanned CW laser systems require as much as 10 minutes to anneal a 3 inch wafer [61]. Even longer cycle times should be expected of rastered beam systems which have significant charging times between pulses.

2. EXPERIMENTAL PROCEDURES

In this section, the apparatus and procedures used for annealing, implanting and characterizing semiconductor material will be discussed in detail.

2.1 Swept Line Electron Beam System

The annealing apparatus is shown schematically in Figure 2.1. The electron gun used was an Alloyed General Vacuum Model EGS-101 with modified strip filament. This gun produced a stationary, cylindrically symmetric electron beam. An electrically grounded molybdenum slit was positioned 2.5 cm below the base of the gun magnet. The beam was allowed to strike the slit in an unfocused condition. This arrangement produced a nearly rectangular electron beam spot on the grounded target plate. The shape of the beam spot could be adjusted through a combination of gun magnet setting, slit width and working distance to the target plate. Normally, a spot size of 1.0 x 1.5 cm was used.

Samples were affixed to the graphite coated molybdenum target plate with graphite adhesive suspension. This plate was attached to a 9 kg copper heat sink and placed on a motor driven X-Y translation table. Samples to be annealed under a common set of conditions were arranged in a row, with the long dimension parallel to the long dimension of the beam spot. Each row of samples was annealed in a single continuous motion of the X-Y table. The entire arrangement was enclosed in a stainless steel vacuum chamber. System pressure was reduced to 5×10^{-6} torr prior to annealing.

The electron beam was monitored by a trio of Faraday cups shown in Figure 2.2. These were arranged in a triangular array on the X-Y table. One side of this triangle was parallel to the longitudinal axis of the beam

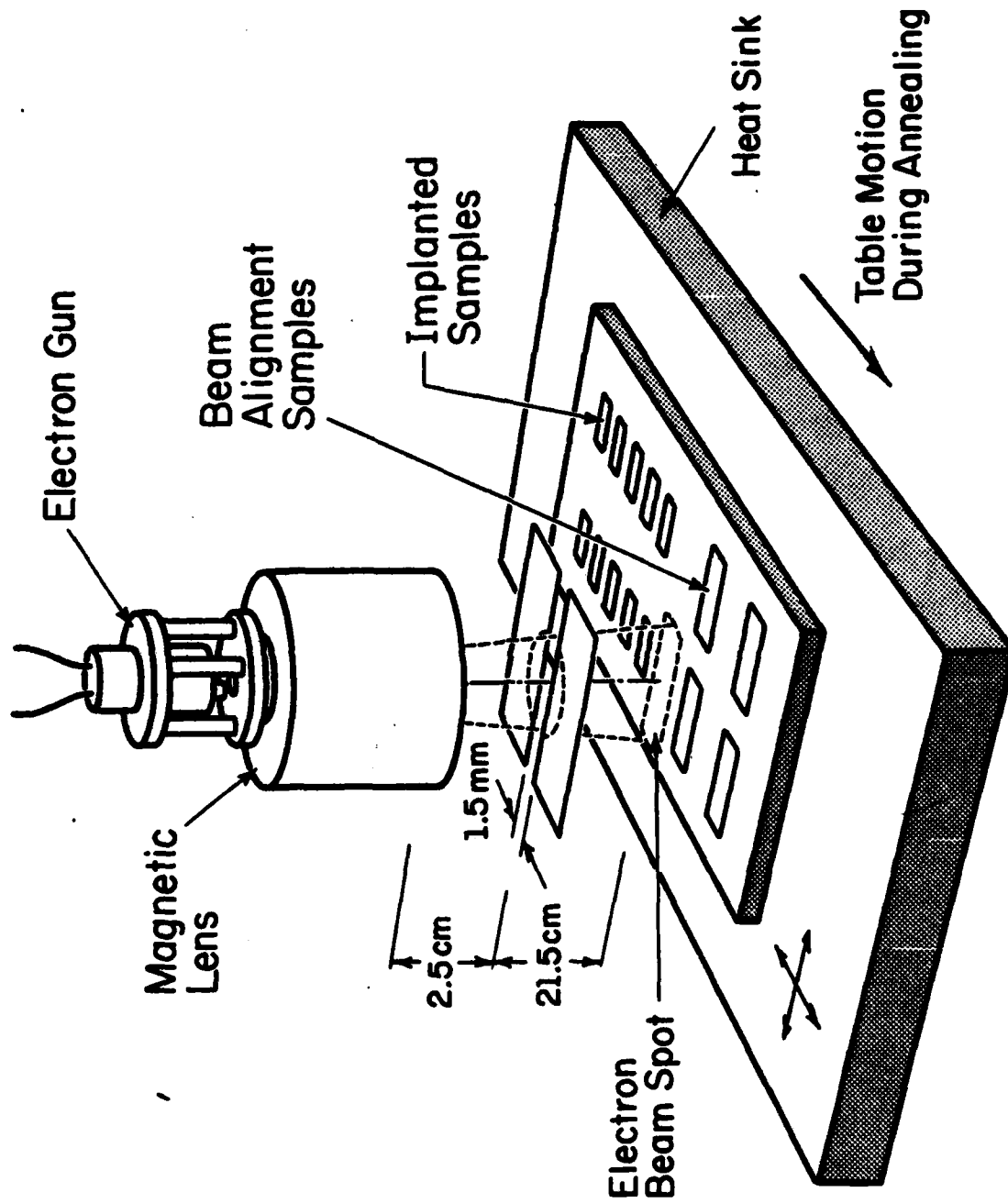
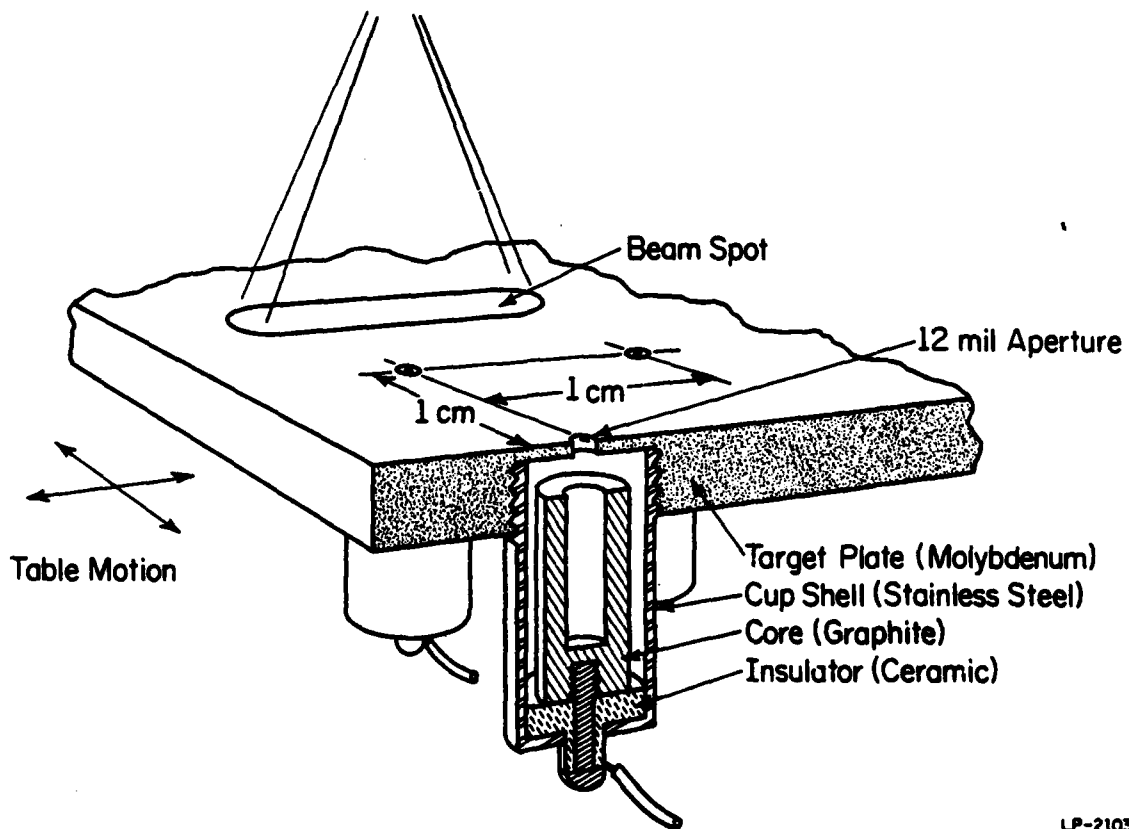


Fig 2.1. Schematic diagram of the Swept-Line Electron Beam Annealing apparatus (not to scale). Slit and target plate are at electrical ground. Alignment samples are used to center each row of experimental samples on the electron beam. (See Yu [91].)

LP-1578



LP-2103

Fig. 2.2. Cut-away view of the Faraday cup beam monitor. Each cup samples a 12 mil wide line as the array is translated through the beam spot. Geometry and materials were chosen so that the cups act as near perfect electron collectors.

spot. During annealing, the array was translated through the beam spot. Collected cup currents were monitored continuously with a Keithley Model 410CR electrometer and strip chart recorder. These records were used to obtain beam energy density profiles and table translation speed.

Each cup was designed to capture nearly all incident electrons [62]. Secondary and backscattered electrons generated within the cups could have introduced considerable measurement error. The secondary electrons, normally defined as those with energy less than 50 eV, [52,63] were easily captured by a small attractive potential applied to the cup cores. The backscattered electrons, however, could have possessed a significant fraction of the incident beam energy [64]. With rough coated graphite for core material, backscattered electron yield was reduced to less than 8% of the incident flux [52]. The re-entrant geometry of the cores ensured capture of most of those actually generated. I estimate no more than 2% of the incident electrons escaped capture.

2.2 Ion Implantation

All implantation was performed on the CSL Accelerators Inc. model 300-MP, shown schematically in Figure 2.3. $^{28}\text{Si}^+$ and $^{11}\text{B}^{19}\text{F}^+$ ions were generated by cold cathode discharge from SiF_4 and BF_3 gas sources respectively. Previous studies have shown that the Si beam created with this source will contain less than 10% residual N_2^+ [65]. This species cannot be removed by mass analysis. A considerably larger percentage of N_2^+ could be expected if the hot cathode and SiH_4 gas source were used. $^9\text{Be}^+$ ions were also generated with the cold cathode, their source being a solid Be canal insert which is continuously sputtered by BF_3 gas discharge. $^{14}\text{N}^+$ ions for GaAsP implantation were generated by hot cathode discharge of N_2 gas.

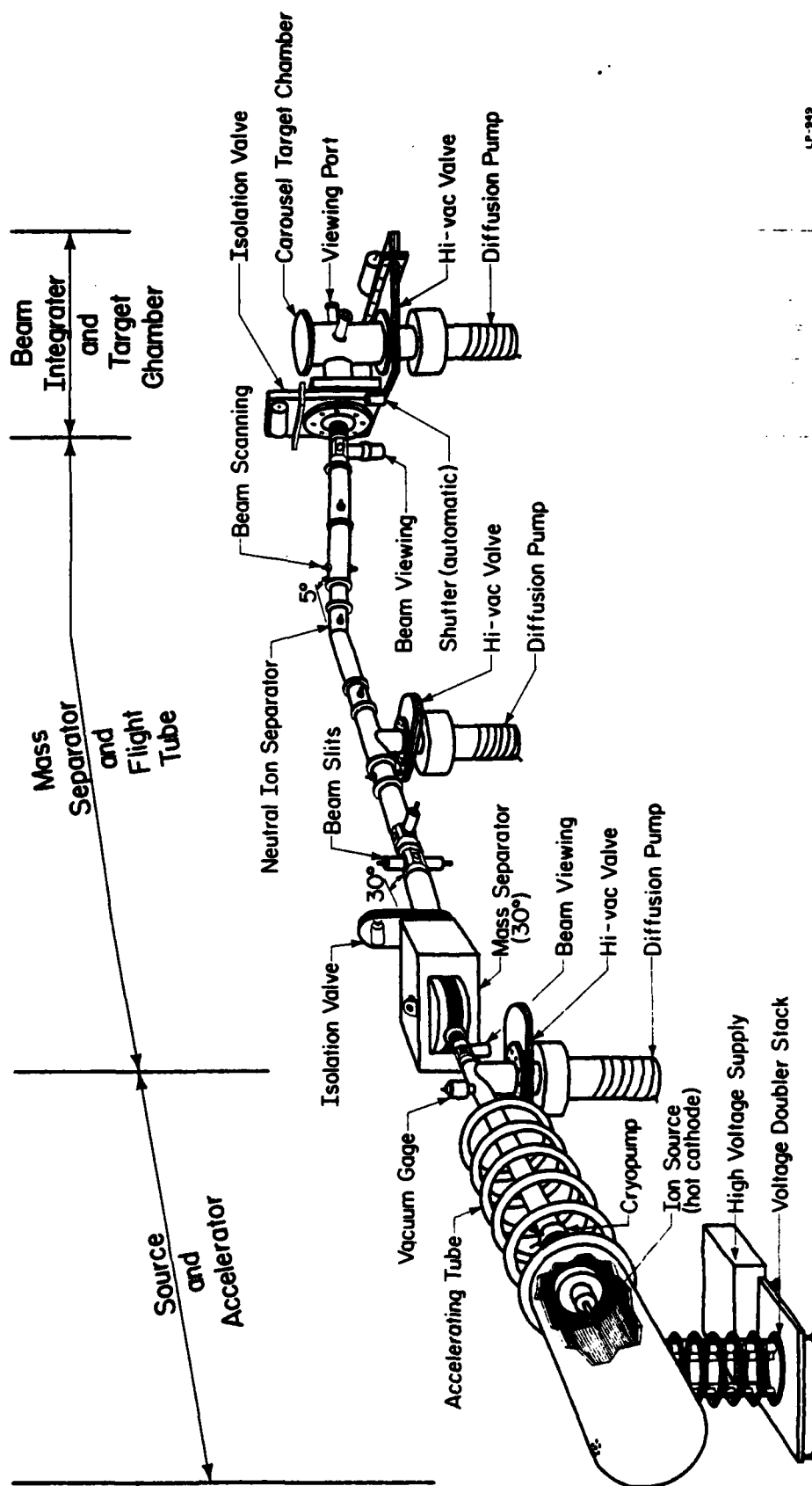


Fig 2.3. Schematic diagram of the Accelerators Inc. MP-300 ion-implantation system. (After Rosa|122|.)

All samples were mounted 7° off beam normal to reduce channeling effects during implantation. GaAsP samples were mounted in the target chamber with conductive paint. Silicon samples were mounted by direct pressure contacts to avoid contamination associated with the adhesive. Si samples amorphized by self-implantation were mounted on a liquid nitrogen cooled finger. The front surface temperature of these samples was monitored with a thermocouple probe.

Perfluorinated polyether diffusion pump fluid was used in the target chamber during all implantations. This fluid was found to reduce surface carbon contamination of implanted material [65]. This was particularly important for low temperature implantation, in which residual gases condense on the cold sample.

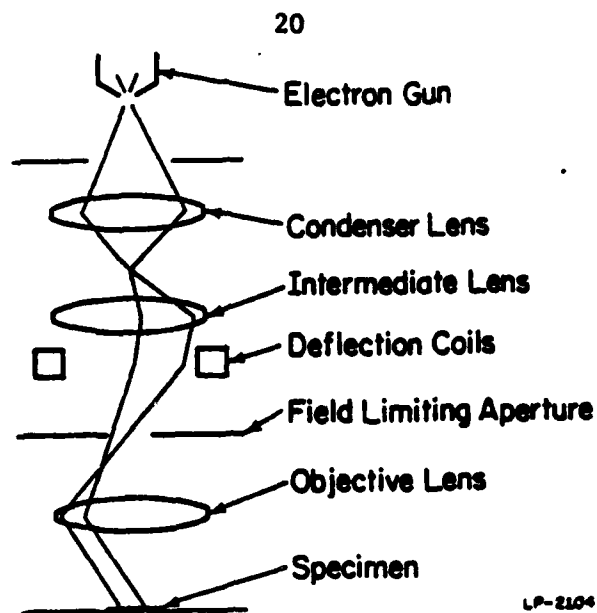
2.3 Methods of Characterization

2.3.1 SEM channeling pattern analysis

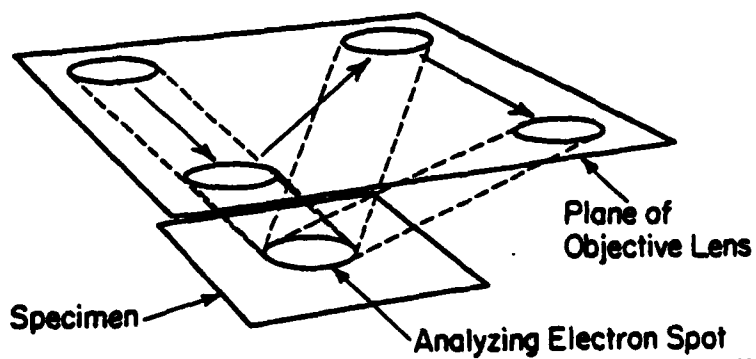
Determination of lattice orientation and qualitative evaluation of crystal perfection were made with scanning electron channeling pattern analysis. A JOEL JSM-35C scanning electron microscope was used. This system was equipped with Selective Area Channeling Pattern (SACP) electronics. Electrons normally used for imaging were analyzed for Bragg backscattering. The resulting patterns represented crystal characteristics only for the area analyzed by the electron spot. Since this spot could be as small as 10 μm diameter, tiny crystallites and disordered regions could be detected.

When operated in the SACP mode, the microscope's electron beam is altered to produce a highly parallel beam [66] (See Figure 2.4a). The beam is rocked and swept about a fixed point as shown in Figure 2.4b. If the specimen is crystalline, the condition for Bragg backscatter will be satisfied

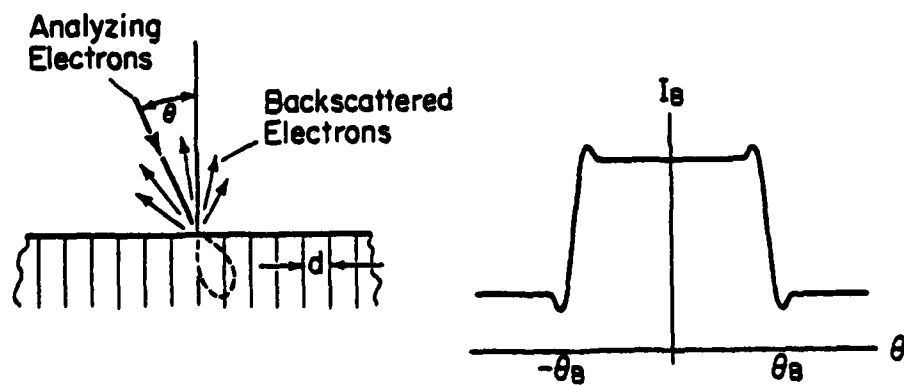
Fig 2.4. (a) Schematic diagram of the JEOL JSM 35C SEM beam optics with channeling pattern electronics activated. Field limiting aperture and lower deflection coils are added. (b) The resulting beam rocking is shown here highly exaggerated. (c) Variation in the first Bloch wave backscattered electron current. A large change in this current occurs when the Bragg condition is met.



(a)



(b)



(c)

at certain points in each scan described by:

$$2d \sin \theta_b = n \lambda_e \quad n = 1, 2, 3, \dots \quad (2.1)$$

Here, d is the crystal plane spacing, λ_e is the electron wavelength and θ_b is the Bragg angle (see Figure 2.4c). The resulting variation in back-scattered electron signal is displayed in conventional video fashion.

The crystallographic orientation of each sample area can be determined from its characteristic channeling pattern [67]. Also, the spacings of lattice planes may be determined from the width of the interference pattern lines as given by:

$$d = c\lambda_e/D \quad (2.2)$$

where D is the SACP line width and c is a constant for fixed SACP mode magnification and electron energy [66].

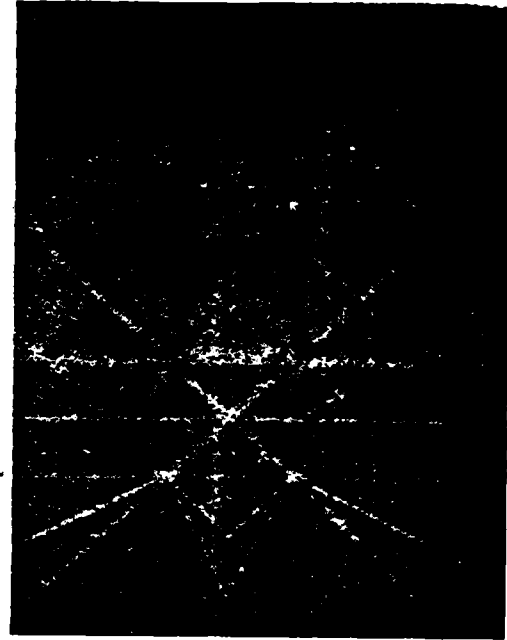
One would expect the quality of a SACP to indicate the degree of a sample's crystal perfection. This is clearly shown in Figure 2.5, which is a succession of SACP's recorded at different points across an amorphous-crystal interface created by partial annealing. As the analyzing spot is moved across the interface (Figure 2.5a to 2.5d), the channeling pattern lines related to the low order crystal planes become visible. In the figure, these are the lines which appear most nearly vertical. Finer detail appears as the beam moves onto undamaged material. The compositional sensing mode of the SEM is used here, which tends to wash out the horizontal interference lines.

It has been shown that an amorphous film as thin as 200 Å, covering an otherwise crystalline sample, will introduce sufficient interference to wash out a SCAP [67]. Physical surface defects such as scratches, stress

Fig. 2.5. Selective Area Channeling Patterns recorded at four points across an amorphous-crystalline interface in silicon. The amorphous material shows no channeling (a). Lower order lattice lines (those most nearly vertical and horizontal appear first (b and c). Finally in crystalline material (d), fine line structure becomes clear.



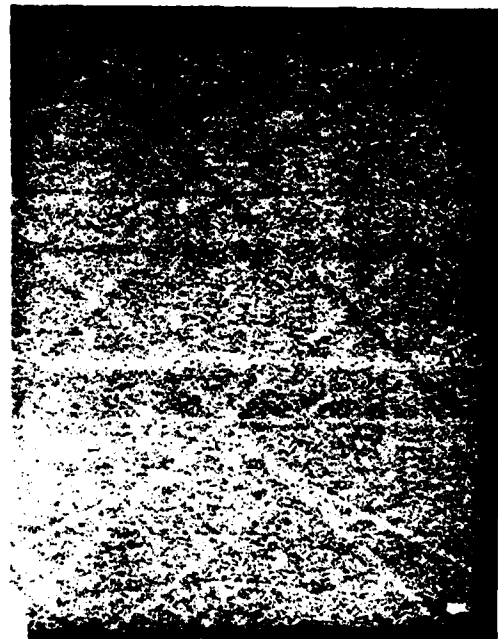
(a)



(b)



(c)



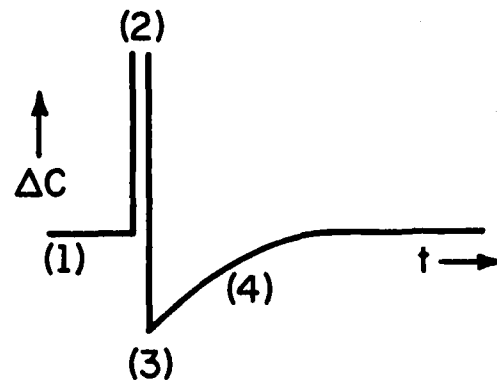
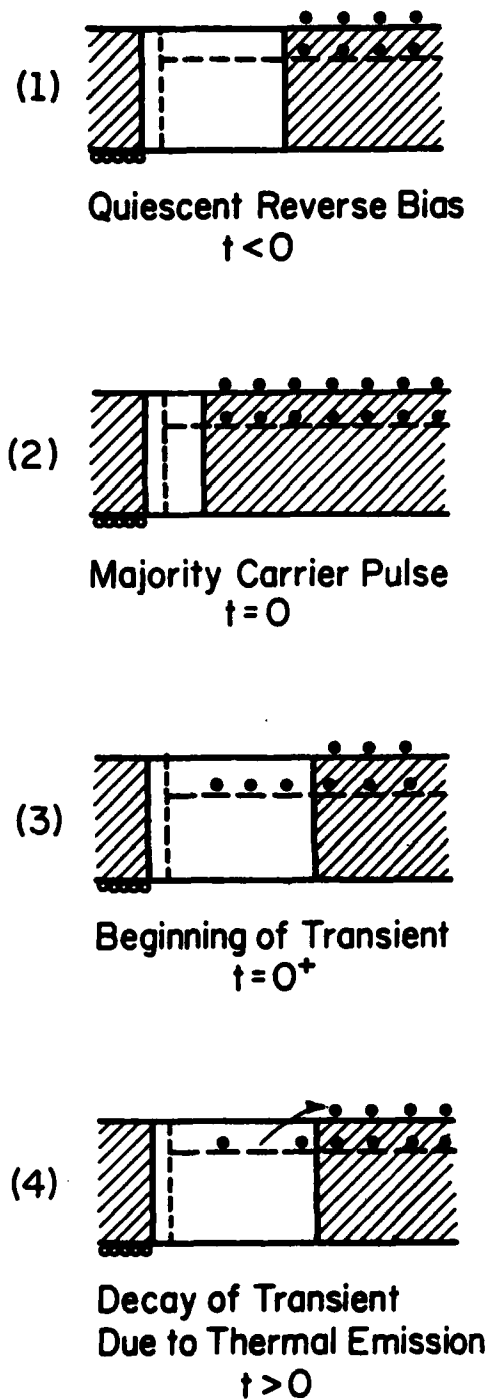
(d)

marks or etch pits also degrade SACP quality. Thus, transient annealed material must have both good crystal order and good surface morphology to produce highly detailed channeling patterns.

2.3.2 Deep level transient spectroscopy

2.3.2.1 Overview and apparatus description

Deep Level Transient Spectroscopy (DLTS) was used in this work to detect and analyze semiconductor defects. The theoretical basis for DLTS has been well established: [68,69] however, I will briefly review the relevant fundamental concepts. Basically, DLTS operates through analysis of transient capacitance decay of a reverse biased diode. An example for majority carrier traps in the depletion layer of a $p^+ - n$ diode is illustrated in Figure 2.6. The device under test is held at a quiescent reverse bias. The traps are initially free of electrons. A short bias reducing pulse is applied which compresses the depletion region, allowing the traps to fill. Immediately after the pulse ends, the junction capacitance falls below its quiescent value C , by an amount ΔC due to the compensating charge of the filled traps. Electrons are then thermally emitted from the traps, and the capacitance returns to its quiescent value. The characteristic time of the capacitance decay depends primarily upon the ratio of the trap activation energy and device temperature. By measuring this decay time as a function of temperature, the energy level of the defect may be inferred. The magnitude of the capacitance change ΔC is a measure of the concentration of defects. By adjusting the magnitude of the bias reducing pulse, one may determine the distribution of a particular defect. The trap capture cross section can be obtained from a measurement of ΔC with varying bias reducing pulse width. If the bias reducing pulse magnitude is increased so as to cause actual



LP-1453

Fig. 2.6. Capacitance transient due to a majority carrier trap in a $p^+ - n$ diode. Inserts labeled 1-4 schematically show the junction depletion layer (shaded region) and charge state of the defect as the transient occurs. (After Lang [68])

injection, DLTS will detect minority carrier traps in the same way. The sign of ΔC determines whether majority or minority carrier traps are being analyzed. It can be seen that DLTS is a powerful technique for the detection and analysis of semiconductor defects.

The DLTS system used in this work was developed by D. S. Day et al. [70] and is shown schematically in Figure 2.7. This system employs a unique two-arm bridge circuit. Each arm contains a diode of similar C-V and I-V characteristic. These are mounted on a common TO-18 header and held within a variable temperature dewar. This arrangement keeps differences in device temperature to a minimum. The bridge is driven by a 20 MHz modulating signal. The device labeled "Test Diode" is driven exactly 180° out of phase with the "Dummy Diode". Shifts in the characteristics of the test device tend to be cancelled by the dummy device, and the entire bridge remains in balance during temperature scanning. Note that the DC quiescent bias is applied to both devices, while only the test device receives the bias reducing pulse. Isolation from this transient pulse is provided by two attenuators, a power splitter, a phase shifter and bandpass filter. We may therefore assume that only the test device produces a ΔC signal.

The bridge signal is demodulated at the HP mixer, amplified and finally detected at the lock-in amplifier. A special gate circuit eliminates the large capacitance overshoot present during the bias reducing pulse. This prevents amplifier overload and keeps system response time limited to less than 1 μ sec. The magnitude of ΔC is displayed on the X-Y recorder as a function of device temperature. A Booton 76-3A standard capacitor is used in place of the diodes to align the bridge to the capacitive mode and to provide calibration.

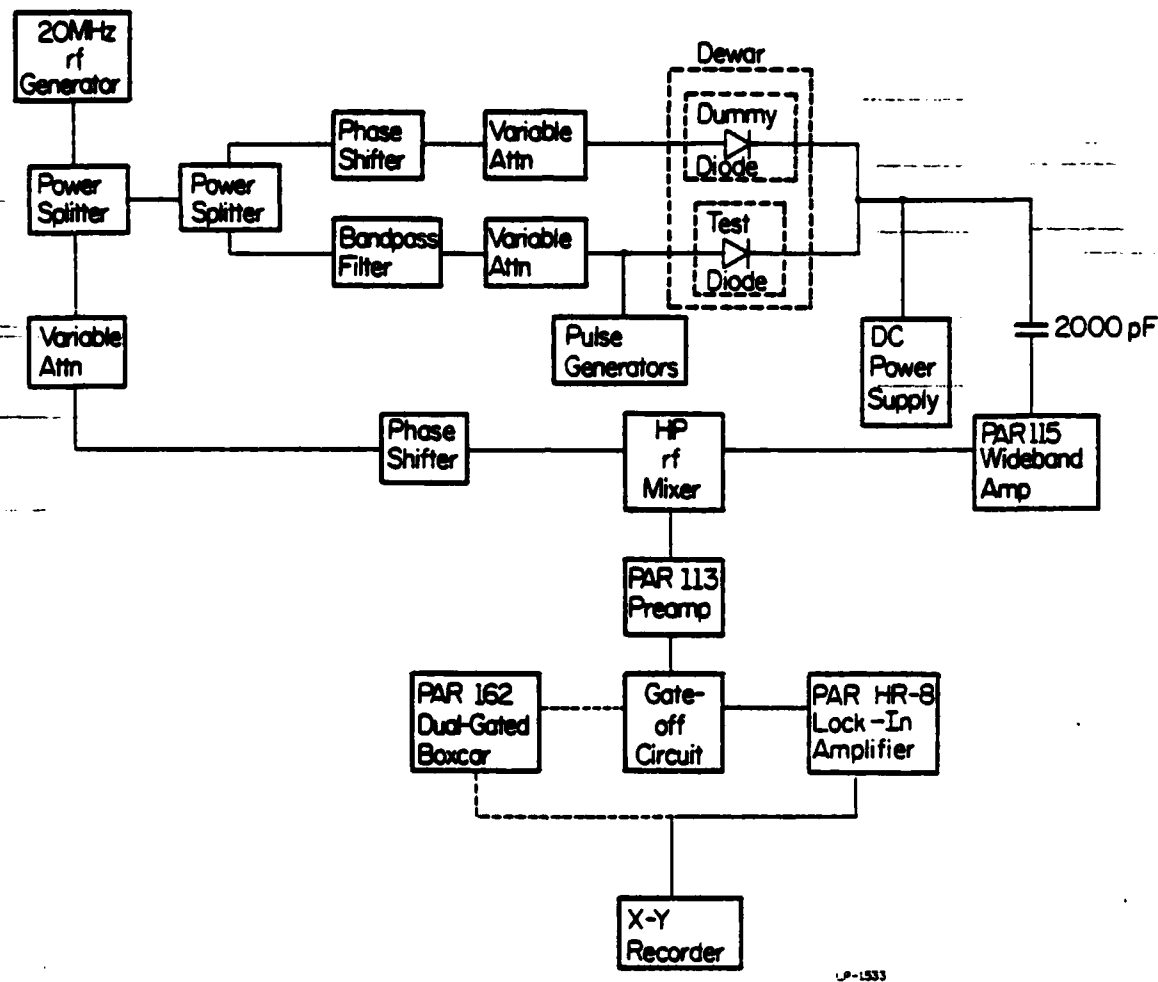


Fig. 2.7. Block diagram of the two-diode DLTS System.
(After Day|70|)

2.3.2.2 DLTS data analysis

In this work, only the energy level of the traps and their concentration profiles were studied in detail. The manner in which this information was obtained from DLTS data is summarized in this section and in Appendix A.

From the principle of detailed balance and carrier statistics, the emission rate of carriers from a trap (e), can be expressed in terms of its capture cross section (σ), the trap degeneracy factor (g), the rms thermal velocity of the captured carrier ($\langle v \rangle$), the appropriate effective density of states (N) and the depth of the trap in the bandgap (ΔE) [69]. For the case of electron traps (and adding appropriate subscripts);

$$e_n = \frac{\sigma_n \langle v_n \rangle N_c}{g} \exp(-\Delta E/k_B T) \quad (2.3)$$

If one assumes no temperature dependence of the capture cross section, (valid for certain types of traps) and using:

$$N_c = 2M_c \left(\frac{2\pi m^* k_B T}{2} \right)^{3/2} \quad (2.4a) \quad \langle v_n \rangle = \left(\frac{3k_B T}{m_e^*} \right)^{1/2} \quad (2.4b)$$

we may write:

$$\frac{1}{\tau_n} = e_n \propto T^2 \cdot \exp(-\Delta E/k_B T) \quad (2.5)$$

where τ_n is the time constant corresponding to this emission rate. Finally,

$$T^2 \tau_n \propto \exp(\Delta E/k_B T) \quad (2.6)$$

Thus a plot of $\ln(T^2 \tau_n)$ vs $1/T$ will yield a line whose slope is proportional through known constants to ΔE . τ_n is determined by the fundamental frequency

set on the lock-in amplifier. T is the temperature at which a trap produces the largest ΔC signal. Each trap can be analyzed at several different frequencies, and least squares fit to these data can then be made to improve accuracy [71].

The actual magnitude of the capacitance transients ΔC must be calculated from the output of the lock-in amplifier. This output is the time average of the product of the input signal and the lock-in's square wave weighting function. Both the shape of the input waveform and its phase with respect to the weighting function will affect the value of ΔC detected. In this work we follow the analysis of Day [71,72]. The input waveform is assumed to be a train of simple exponentially decaying spikes. The weighting function is adjusted to be in phase with the leading edge of the bias reducing pulse (bias-pulse phase reference method). Under this condition, mathematical analysis of the detection process yields the expression:

$$\Delta C = 0.560 \times S_L \times S_B \times V_L \quad (2.7)$$

where ΔC is the transient capacitance in pF, S_L is the lock-in sensitivity in volts, S_B is the calibration factor in pF/V and V_L is the lock-in output in volts.

From these values of ΔC , one may construct a profile of defect density. If one considers the example of a p^+-n diode, Lang has determined [73]

$$\delta \left(\frac{\Delta C}{C} \right) = \left(\frac{\epsilon}{qW^2 N^+} \right) \frac{N_T(x_c)}{N^+(x_c)} \delta V_c \quad (2.8)$$

where C and W correspond to the diode capacitance and depletion width while quiescent reverse bias V is applied. $\delta \left(\frac{\Delta C}{C} \right)$ is the change in the $\frac{\Delta C}{C}$ ratio between two successive measurements, with bias reducing pulse V_c and

$V_c + \delta V_c$. N^+ is the fixed charge concentration (due to ionized donors in our example) at the n edge of the depletion layer. $N_T(x_c)$ and $N^+(x_c)$ are respectively the densities of traps and of fixed charge at the location (x_c) of the depletion layer edge during the bias reducing pulse $(V_c + \delta V_c)$. A trap profile may be constructed via a series of measurements of ΔC while varying V_c , with fixed V . To be valid, $\Delta C \ll C$ and traps must occur only on the n-side of the junction. It must also be assumed that the acceptor and donor concentrations change in the same ratio on both sides of the metallurgical junction. This assumption is valid for linearly graded and step junctions.

The fixed charge profiles were produced via point-by-point capacitance voltage measurements. A Hewlett Packard 6114A precision power supply provided bias to a Boonton 72B capacitance meter for these measurements. A sufficiently small interval in voltage was placed between measurements to estimate dC/dV . The magnitude of fixed charge concentration was determined via the expression:

$$N(x) = \frac{C(V)^3}{\epsilon q A^2 (-dC(V)/dV)} \quad (2.9)$$

The depth x was determined by numerical integration of the fixed charge concentration profile and knowledge of the device geometry (See Appendix A, Section A.2, lines 19800-21800).

Trap profile analysis, including determination of the fixed charge profile, was accomplished by computer. The FORTRAN program TRAPSI was developed specifically for Schottky barrier diodes on n-type silicon. This code is described in detail in the appendix.

2.3.3 Differential resistivity and Hall effect measurements

Profiles of electrically active implanted dopants were established by differential resistivity and Hall effect measurements made in conjunction with chemical layer stripping. The apparatus was developed by McLevige et al. [74], and is shown schematically in Figure 2.8. This double AC Hall system possessed high sensitivity, good noise rejection and inherent averaging of misalignment and thermoelectric effects. During Hall measurements, the samples were placed in an AC electromagnet which was driven at one fourth the basic system frequency (f_1) of 1 kHz. Via a mixer and filter, a $f_1 - f_2$ signal was generated which formed the lock-in reference signal for the Hall voltage. f_1 was used as the lock-in reference for resistivity measurements.

Samples were prepared by the technique described by Tsai [65]. The carrier type of the substrate was chosen so that a p-n junction was formed after implantation and annealing. First a 120 mil square van der Pauw mesa pattern was photolithographically defined and plasma etched. Gold contacts were then evaporated and later sintered at 300°C in flowing dry H_2 . Samples showing good junction characteristics were selected so that only the implanted layer contributed to the measurement. After each measurement, a thin layer of the sample was removed by chemical etching. A series of wax defined mesas were formed on each sample during thinning. The heights of these mesas were later measured by Detak mechanical stylus to establish the depth scale. The thinning and measurement process was continued until the samples became too resistive to measure.

The sheet resistivity (ρ_s), and sheet Hall coefficient (R_s), are calculated from [75]:

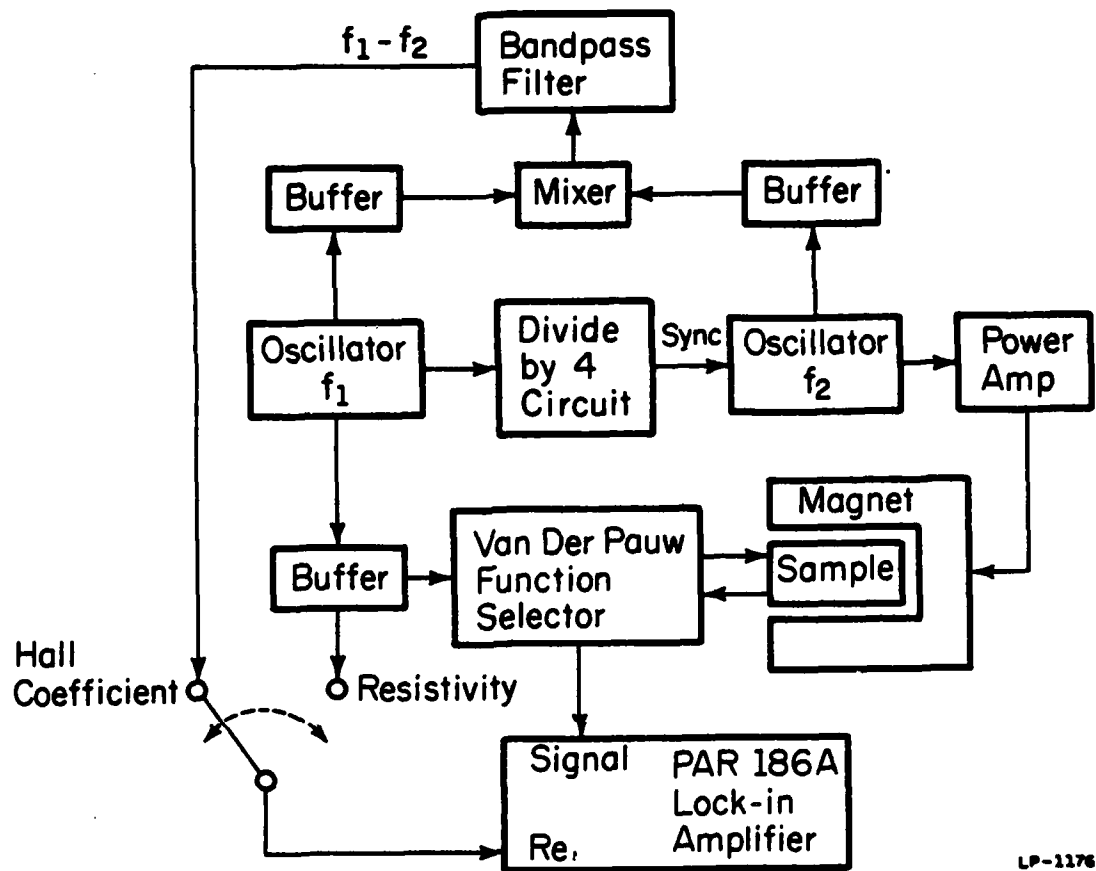


Fig 2.8. Block diagram of the double AC Hall apparatus.
(After McLevige et al. [74])

$$\rho_s = \left(\frac{\pi}{\ln 2} \right) \cdot \frac{V_{ABCD} + V_{BCDA}}{2I} \cdot f \left(\frac{V_{ABCD}}{V_{BCDA}} \right) \quad (2.9)$$

$$R_s = \frac{\sqrt{2} \Delta V_{BDAC}(\text{rms})}{B(\text{rms}) I(\text{rms})} \quad (2.10)$$

Here the designation V_{ABCD} corresponds to the voltage between contacts A and B with current I passing between contacts C and D, and similarly for V_{BCDA} . ΔV_{BDAC} is the change in Hall voltage induced by placing the sample into the magnetic field of strength B. The correction factor $f \left(\frac{V_{ABCD}}{V_{BCDA}} \right)$ has been tabulated by van der Pauw [75].

The average mobility and carrier concentration of a particular layer j of thickness d_j are given by: [76]

$$\gamma \mu_j = \mu_{H_j} = \frac{R_{sj}}{\rho_{sj}} + \frac{R_{sj-1}}{\rho_{sj-1}} - \frac{R_{sj-1} - R_{sj}}{\rho_{sj-1} - \rho_{sj}} \quad (2.11)$$

and

$$n_j = \frac{\frac{1}{\rho_{sj}} - \frac{1}{\rho_{sj-1}}}{e d_j \mu_1} \quad (2.12)$$

The designation j-1 refers to the preceeding layer. γ is the ratio of Hall (μ_{H_j}) and conductivity mobility (μ_j). Its value was taken to be 0.73, which is appropriate for the highly doped p-type silicon layers studied here [77].

3. SLEE ANNEALING OF Si^+ -IMPLANTED AMORPHOUS SILICON

This chapter presents a comparative study of amorphous ion-implanted silicon recrystallized by swept-line electron beam and conventional furnace annealing. Solid phase recrystallization of amorphous silicon has been studied previously using furnace techniques [65,78,79]. Dopants implanted in high doses can be efficiently activated with accompanying recrystallization at relatively low temperatures (approximately 550°C). As demonstrated by Tsai et al. [80], however, electrical profiles of these dopants can include an electrically inactive tail due to heavy residual implantation damage. (See section 4.1) This layer is located between the bulk material not damaged by the original implantation and material which regrows completely during annealing. In a p-n junction, this damage coincides with the depletion region, and will adversely affect leakage currents and minority carrier lifetimes.

Tsai et al [81] have also shown that the location of the residual damage can be pushed well beyond the p-n junction by amorphizing the sample (eg., by Si^+ ion implantation) to a depth beyond the implanted dopant profile. Samples prepared in this manner have completely active dopant profiles. In fact, fluorine migration to defects [81] has shown that the unannealed damage is moved to the tail of the deep amorphizing implantation.

The presence of this damage was further confirmed through a preliminary study using silicon solar cells. This work was undertaken in cooperation with Dr. J. Eguren of the Instituto De Energia Solar, Madrid, Spain. A set of n^+pp^+ back surface field cells was fabricated with and without the use of amorphizing self-implantation. Here the low-hi (pp^+) region is meant to reduce the back surface recombination velocity. The

front surface n^+ layers were formed by conventional furnace diffusion. Some of the samples then underwent multiple low temperature Si implantation to produce a continuous amorphous back surface layer. A single room temperature gallium implant was then made in all the samples to form the back surface p^+ layer. The energy of this implantation was sufficiently low that all gallium atoms remained well within the amorphous layer. After furnace annealing, the solar cells were characterized under Air Mass 1 illumination.

Representative results are shown in Table 3.1. These data show consistently better performance in cells which were not pre-amorphized. Samples 1.2 - 1.4 show generally smaller open circuit voltage ($V_{ocf,b}$) and short circuit currents ($I_{f,b}$) when compared with sample 1.1. Implantation and annealing conditions were such that one would expect a completely active gallium layer in the pre-amorphized cells and only partial activation of gallium in the unamorphized cells. This alone would lead one to expect just the opposite of the observed difference in performance. The result can be explained in terms of reduced cell base lifetime, due to the self-implantation induced damage. The study described below will characterize this damage in some detail.

DLTS is used here to directly evaluate residual crystal damage. The experiment is simplified through the use of Schottky barrier diodes fabricated on recrystallized self-implanted material. Ambiguities of p-n junction dopant-defect complexes are thus eliminated. Since Schottky diodes can be prepared without disturbing the bulk crystal, a direct comparison of SLEB and furnace recrystallized material can be made.

TABLE 3.1
AMI RESPONSE DATA
Ga⁺-IMPLANTED SI SOLAR CELLS

<u>Sample</u>	<u>Pre-damaged</u>	<u>Dose (cm⁻²)</u>	<u>Annealing Temp/Time</u>	<u>I_f (mA)</u>	<u>V_{oc}^f (mV)</u>	<u>I_b (mA)</u>	<u>V_{oc}^b (mV)</u>
1.1	No	3.75x10 ¹⁴	600°C/30 min	31.7	549	4.9	495
1.2	Yes	1.56x10 ¹⁴	550°C/30 min	34.2	459	3.5	352
1.3	Yes	3.75x10 ¹⁴	550°C/30 min	27.1	400	3.1	330
1.4	Yes	3.75x10 ¹⁴	550°C/30 min	26.2	391	2.8	340

Comparative response data for Ga-implanted Si solar cells prepared with and without amorphizing Si⁺-implantation of the back surface. The designations b and f refer to measurements made with back and front surfaces illuminated. Note the generally smaller values of I and V_{oc} observed in the predamaged cells, especially during back surface illumination.

3.1 Experimental Procedure

Devices used in this study were fabricated from 0.24 Ω -cm ($4 \times 10^{16} \text{ cm}^{-3}$), phosphorus doped Czochralski grown bulk silicon. This level of dopant was chosen to provide the best compromise between Debye length limits on profile resolution and the requirement for full depletion of the regrown amorphous layer during measurement [83]. As in the solar cell experiments described above, the samples received four cold ($\lesssim -100^\circ\text{C}$) amorphizing implants with Si^+ ions of energies 32, 91, 158 and 255 keV. These energies and the corresponding doses were chosen to give the best fit to an ideal 0.5 μm deep, flat implanted profile of $1 \times 10^{20} \text{ Si}^+/\text{cm}^3$. Etching experiments [81] determined the depth of the amorphous layer to be $4550 \text{ \AA} \pm 125 \text{ \AA}$.

Samples were then recrystallized either by the SLEB process or by conventional furnace annealing. The electron beam annealing process was described in section 2.1. An electron energy of 20 keV and table translation speed of 0.32 cm/sec were used in this work. A second set of samples was thermally annealed in a quartz-lined furnace tube under a forming gas ambient. Unimplanted material was heat treated simultaneously to detect defects which might be introduced during furnace annealing and unrelated to the implantation.

After annealing, the front surfaces of the samples were anodically oxidized [65] to remove a 200 \AA layer of Si, exposing clean surfaces for Schottky barrier formation. Al Schottky barriers and Au-Sb ohmic back-side contacts were formed by vacuum evaporation through shadow masks. Individual devices were cut, mounted on headers, and thermocompression lead bonded. Sample heating did not exceed 300°C for 10 minutes during this processing.

Defect energy levels and profiles, as well as profiles of fixed charge were measured and calculated by the methods described in section 2.3.2 and the appendix. With the exceptions noted below, measured values of $\Delta C/C$ were between 10^{-2} and 10^{-5} , satisfying the restriction that $\Delta C/C \ll 1$ [68,69].

3.2 Results and Discussion

DLTS spectra are presented in Figure 3.1 as a function of 30-minute isochronal furnace annealing. The DLTS signal is plotted logarithmically, with majority carrier signal increasing along the vertical scale. The peak trap signal decays as the regrowth temperature is increased, as expected. In each case, the spectra are dominated by two defect signals. The lower temperature signal (corresponding to $E_c - 0.22$ eV) appears in all three cases and becomes dominant as annealing temperature is increased. The higher temperature trap signal changes from $E_c - 0.50$ eV to $E_c - 0.35$ eV to $E_c - 0.42$ eV as the annealing temperature is increased. Defects with activation energies within ± 0.02 eV of these four trap signals have been observed in implanted [84], irradiated [85,86], or laser damaged silicon [87]. Defect spectra for control Schottky barriers fabricated on unimplanted but simultaneously annealed Si show no detectable defect signal.

Similar spectra are shown in Figure 3.2 for SLEB samples processed at three peak beam power densities. There is a marked reduction in the peak trap signal from lowest to highest power density. The dominant signal peak of the well-annealed SLEB case (38 W/cm^2) is about a factor of four smaller than the smallest peak in the 800°C case of Figure 3.1. The designation "x2" refers to a sample which was annealed by two passes of the beam. Notice that the double annealed sample at intermediate power density (27.5 W/cm^2) shows the largest over-all defect signal spectra. The thermal

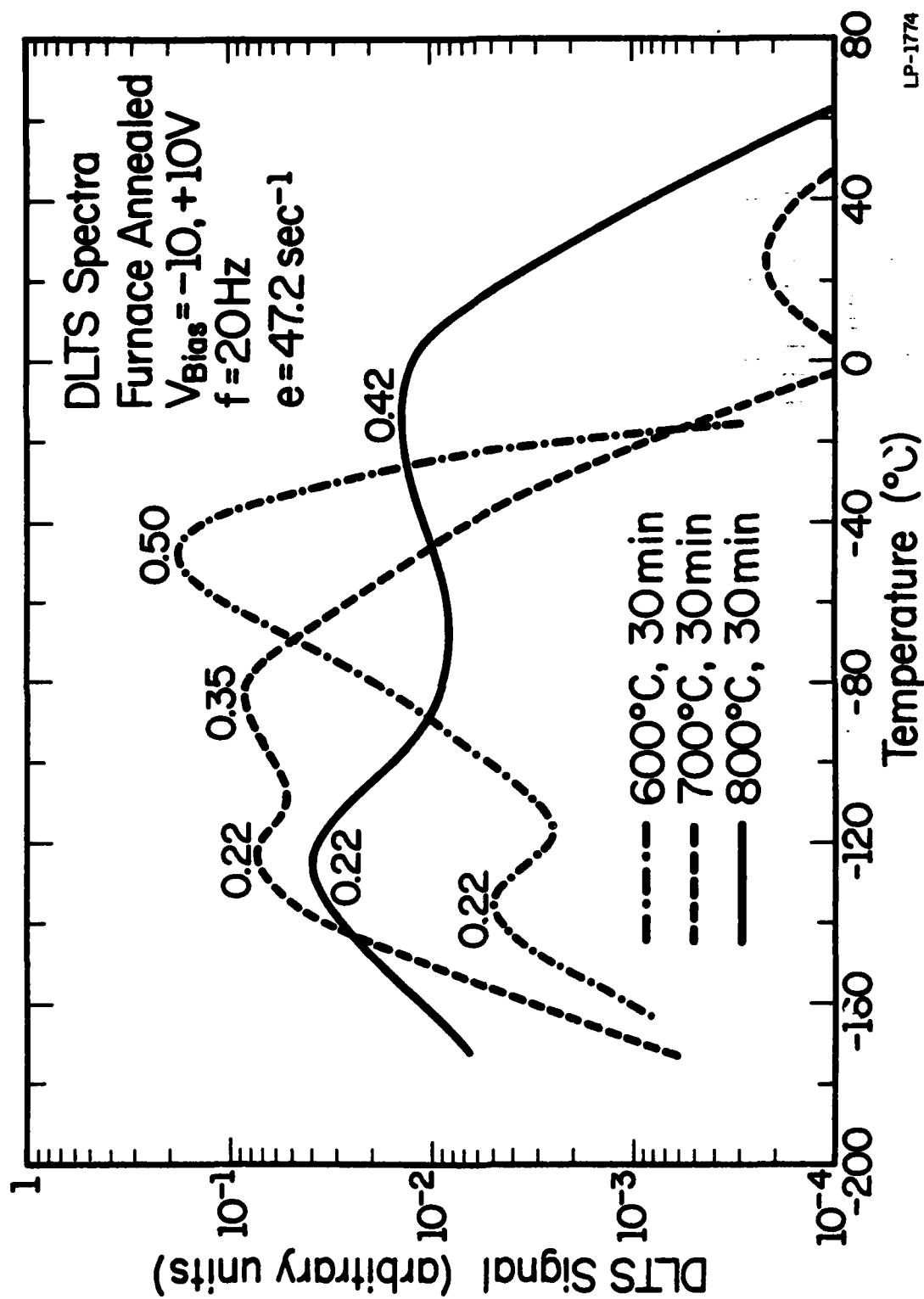


Fig. 3.1. DLTS spectra for Schottky barriers fabricated on furnace annealed silicon. Majority carrier signal is plotted on the logarithmic vertical scale. (See Soda [31].)

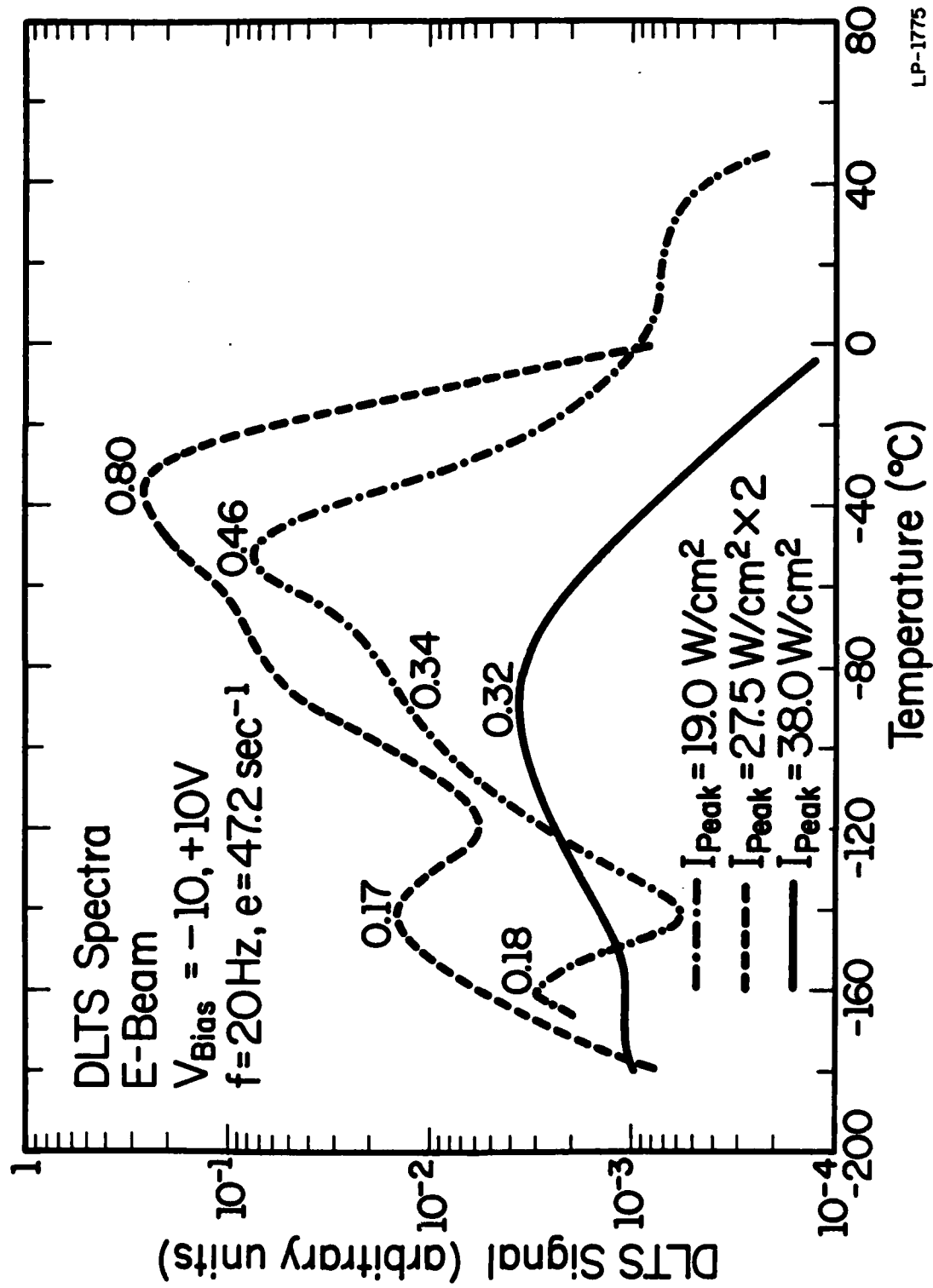


Fig 3.2. DLTS spectra for samples annealed by SLEB for three power densities. The vertical scale has units identical to figure 3.1. (See Soda [31].)

activation energies observed in the SLEB case, with the exception of $E_c - 0.34$ eV, do not correspond to those observed in the furnace case. Activation energies within ± 0.02 eV of the observed levels $E_c - 0.17$ eV, 0.18 eV, 0.34 eV, and 0.46 eV, have been previously observed in implanted [84], irradiated [85,86], or laser damaged [87] silicon. The level $E_c - 0.80$ eV has not been reported previously.

Profiles of fixed charge and defect concentration for the furnace annealed devices are presented in Figures 3.3 and 3.4. In each case, the profiles are dominated by a layer of defects and fixed charge near the original amorphous-crystalline interface (marked by the arrow). The magnitude of these effects decays with increased annealing temperature. Also observed is a relatively small concentration of defects in the near surface regions. This is accompanied by a tendency for fixed charge concentrations to return to values corresponding to the original bulk dopant concentration ($4 \times 10^{16} \text{ cm}^{-3}$).

In the 700°C and 800°C cases, the defect profiles reach a maximum at 0.42 to $0.45 \mu\text{m}$ respectively, corresponding to the measured thickness of the original amorphous layer. This observation verifies the location of damage reported by Tsai et al. [81,82] from their Hall profiling and fluorine decoration studies. Previous studies in irradiated material also indicate that the near surface recrystallized regions tend to have fewer defects [88], as observed here.

The fixed charge profiles presented here must include the contributions of both ionized donors and defects [83]. In regions where the defect concentrations become comparable to the fixed charge profiles, one cannot strictly interpret the latter as a donor profile. Rather, the fixed charge profile represents $N_d + nN_T$, where n and its sign depend upon the charge state

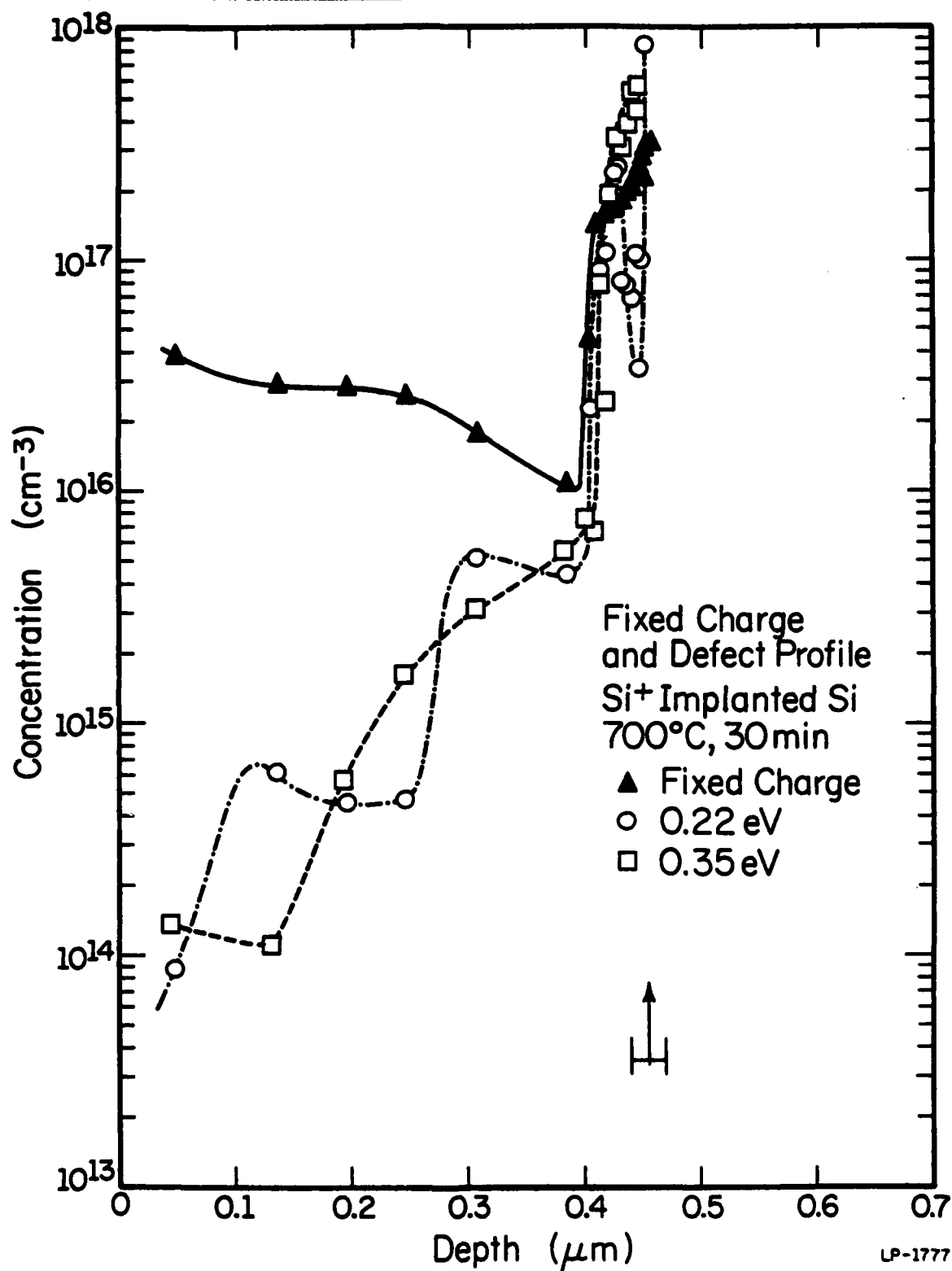


Fig. 3.3. Fixed charge and defect profiles for 700°C furnace processed silicon. The arrow indicates the location of the original amorphous-crystalline transition region. (After Soda [31].)

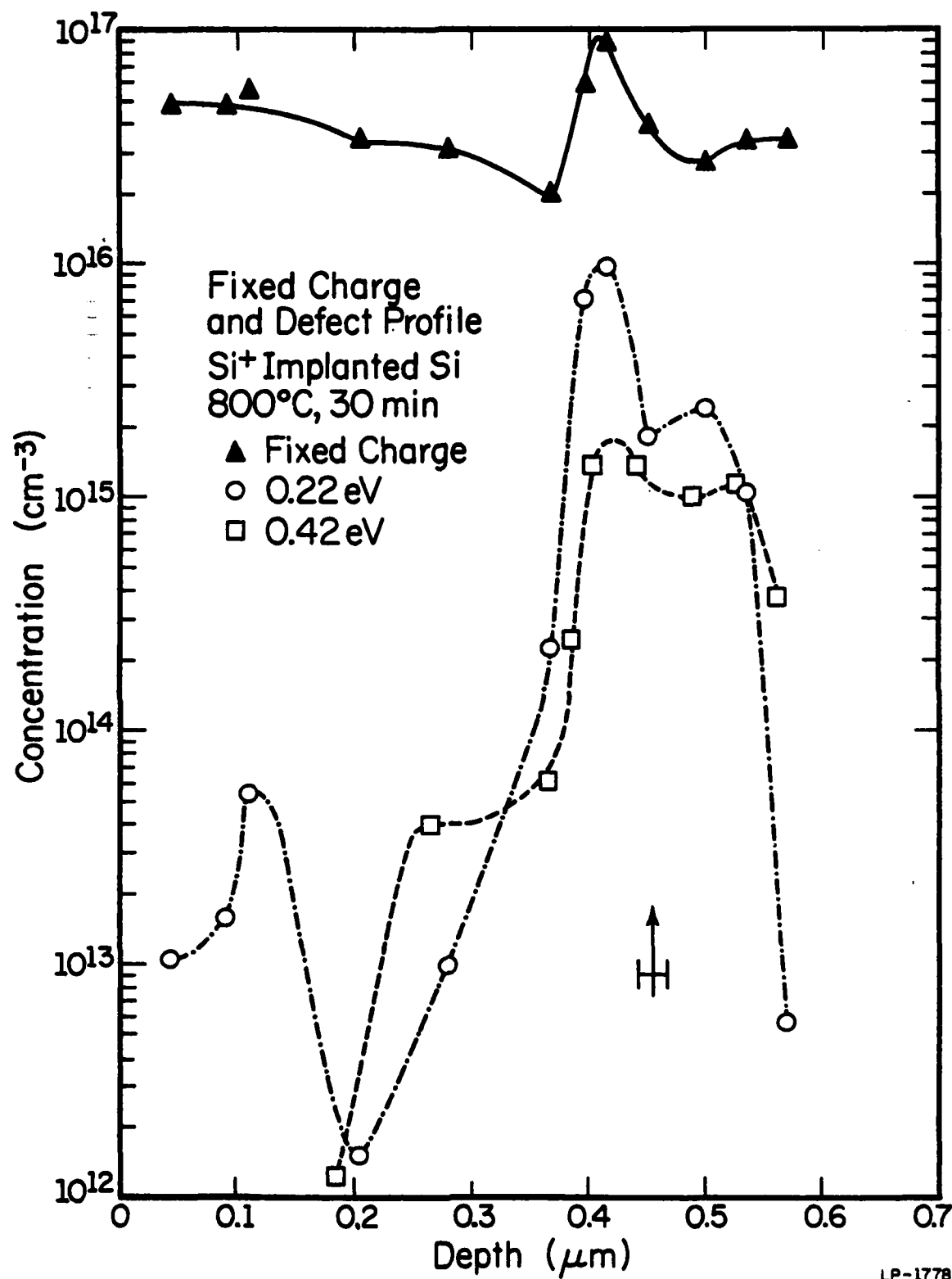


Fig. 3.4. Fixed charge and defect profiles for 800°C furnace annealed material. Note the change in vertical scale from Fig. 3.3. (See Soda [31].)

of the defect. This is important in the 700°C case near the peak damage region. In the 800°C case, however, ionized donor charge predominates and we see definite donor redistribution, particularly in the neighborhood of the original amorphous-crystalline interface. The donor redistribution effect can be understood in terms of a dissociative diffusion process of the type proposed by Baruch [89]. Motion of dopants is explained by a pair of competitive processes in which a defect will first liberate a donor atom from its lattice site, then cause the donor to move by attraction to another defect site. The donor atom undergoes a net motion in the direction opposite the motion of defects. These processes are used to explain bulk dopant redistribution and peaking in proton irradiated silicon [89]. The shapes of the donor profiles in the near-surface region suggest dopant motion toward the interface region.

It is likely that the solid phase regrowth process itself is involved in the redistribution of both defects and donor atoms, especially in the 600°C case (not shown). A reasonable extrapolation of previously determined solid-phase epitaxial regrowth rates [78] indicate that nearly 25% of the total annealing time was required to recrystallize the amorphous layer in this case. The advancing crystal front seems to push defects ahead of it, accelerating the motion of dopant atoms and leaving a bulge in the defect profiles near 0.23 μm . Regrowth times are estimated to be factors of 14 and 370 times faster respectively for the 700° and 800° anneals shown here. No bulge in the defect profile is observed in the regrown regions of Figures 3.3 and 3.4, indicating that either the crystal front has moved too rapidly to push the defects, or they have annealed extensively after regrowth is complete.

Defect and fixed charge profiles for swept-line beam annealed material are shown in Figures 3.5 and 3.6. In both cases, the residual defect concentrations are small enough that one may interpret the fixed charge profiles as due entirely to ionized donors. After a single sweep by a 19 W/cm^2 electron beam, the sample exhibits a series of broad, relatively flat defect profiles (not shown). Surface channeling pattern analysis shows that annealing in this case is insufficient to completely regrow the amorphous layer.

Recent studies of nitrogen implanted $\text{GaAs}_{1-x}\text{P}_x$ [91] have suggested that multiple scanning with SLEB can improve crystal quality without defect migration. This possibility was explored in the 27.5 W/cm^2 sample (Figure 3.5), which was double annealed. In this case, severe dopant redistribution occurs. Electron microscope channeling analysis shows complete recrystallization was not achieved. Since the 0.80 eV defect $\Delta C/C$ signal is so large (≈ 0.1), its profile is doubtful. Some surface dopant out-diffusion is observed. A large misalignment of the defect and donor peaks with the amorphous-crystal interface is observed, probably due to a near surface donor depleted region which cannot be analyzed by C(V) measurements. We believe the depth scale is affected, and that the peaking of defects and charge in Figure 3.5 actually occurs at the original interface (marked by the arrow).

The threshold for complete crystal growth is crossed in the 38 W/cm^2 case (Figure 3.6). SEM analysis shows perfect near surface crystal order. Both dopant redistribution and out-diffusion effects are minimized. The profile of the single defect observed in this case ($E_c = 0.32 \text{ eV}$) occurs

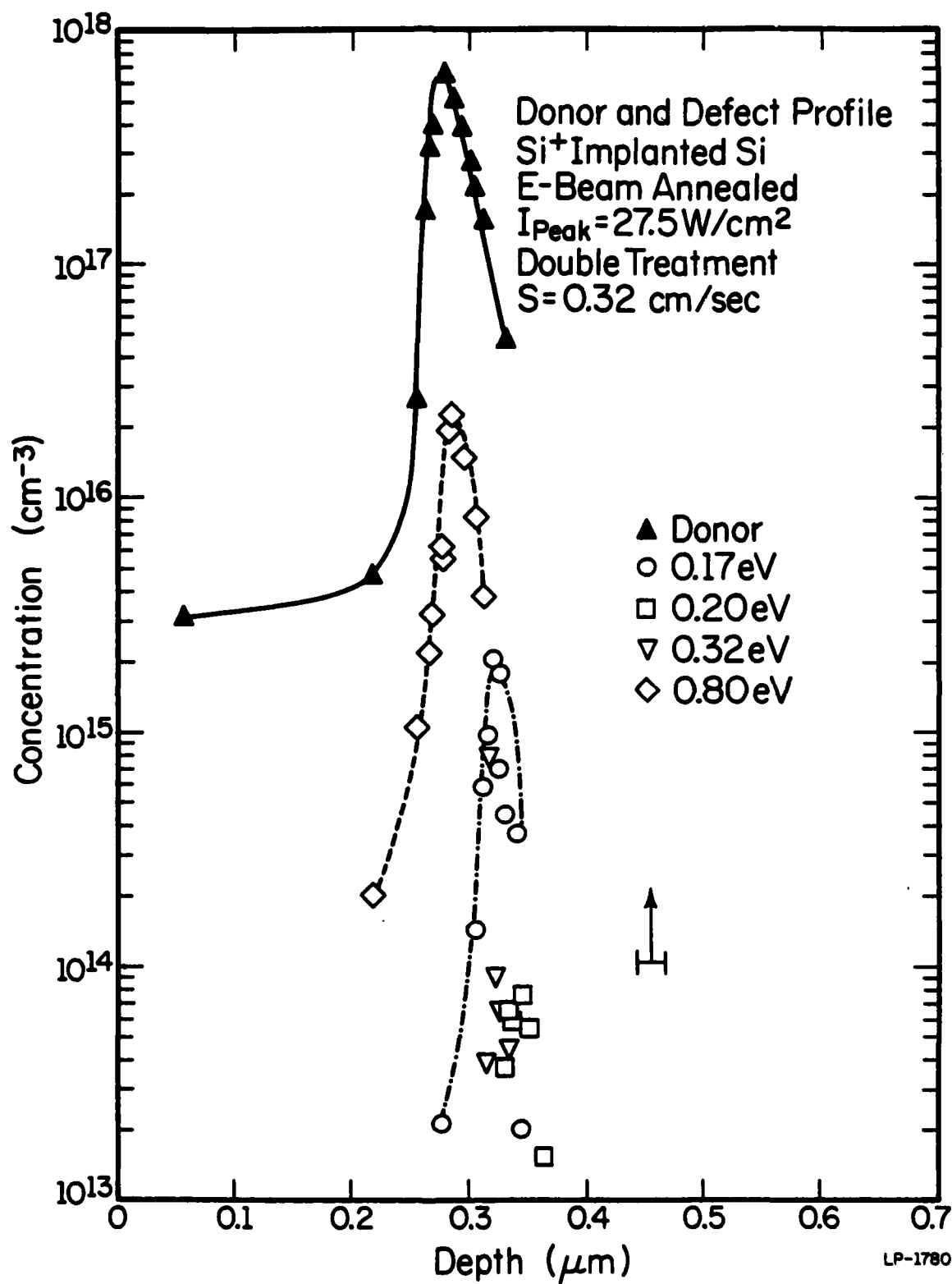


Fig. 3.5. Donor and defect profiles for Si^+ implanted silicon processed with two passes of a 27.5 W/cm^2 beam. (After Soda [31].)

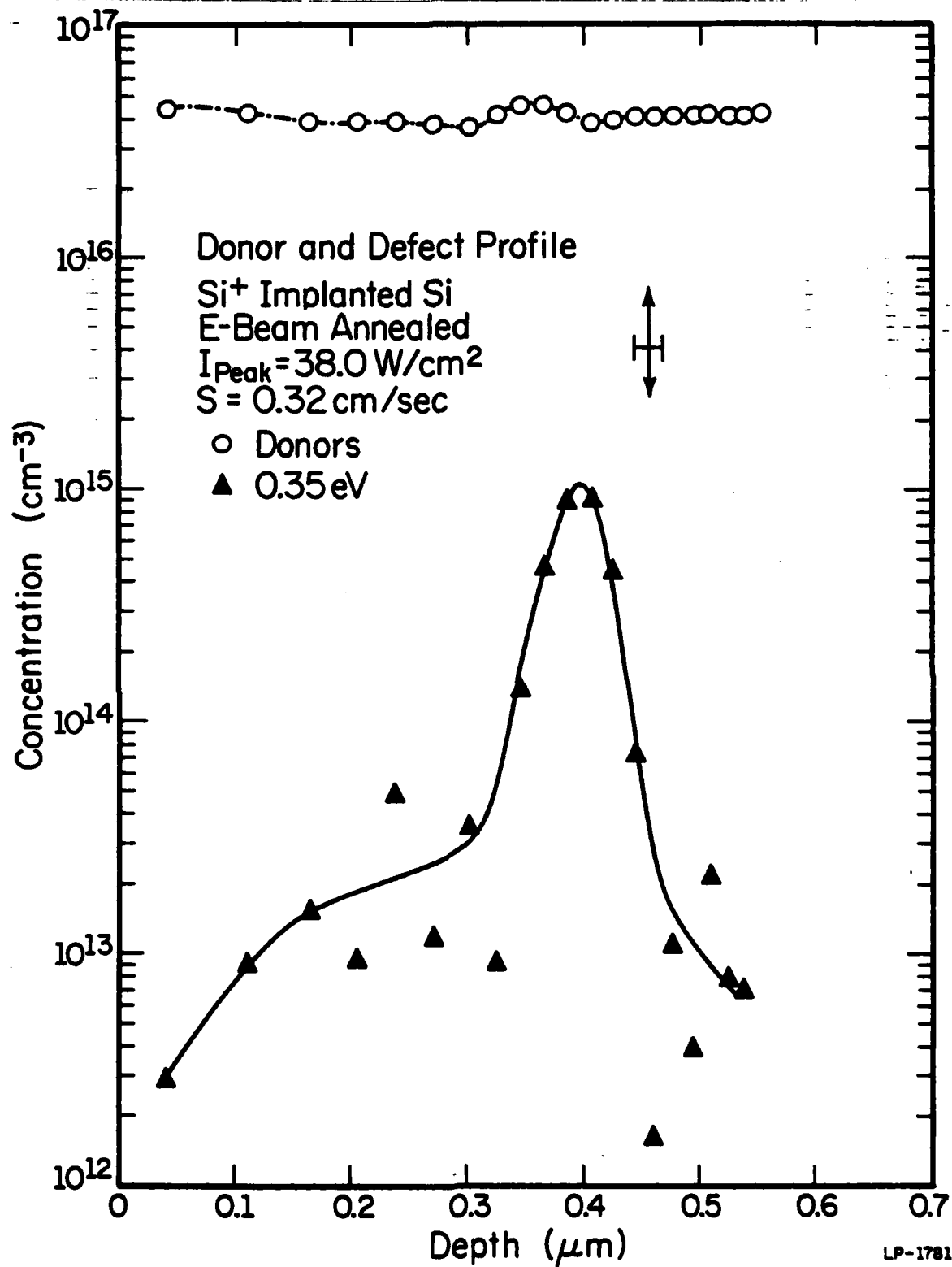


Fig. 3.6. Donor and defect profiles for 38 W/cm^2 SLEB annealed silicon. Note the change in vertical scale from fig. 3.5. (See Soda [31].)

LP-1781

at about the depth of the original amorphous-crystalline transition. Peak defect concentrations are a factor of ten smaller than in the 800°C furnace annealed case, while near surface defect densities are a factor of five to ten smaller.

Other studies of recrystallization of amorphous Si by pulsed E-beam processes [92] explain the regrowth strictly in terms of beam induced heating. In this work, total annealing times on the order of two seconds were used. These are considerably longer than either pulsed [92] or raster scanned [93] E-beam processes. Therefore, the annealing conditions are somewhat more similar to those observed to cause MeV electron or keV proton irradiation induced defect annealing. In these studies, TEM techniques [94,95] and IR absorption [96] are used to observe both crystal regrowth and accelerated defect annealing.

Geranismanko [97] has suggested that point defects generated by higher energy electrons can be responsible for decay of relatively stable defect formations, such as those observed in this work. These defects are thought to compensate or induce migration of the defects responsible for the original amorphous state. He also suggests that the electron induced ionization may change the charge state of the defects, increasing their mobility.

It would seem that generation of point defects by electrons of only 20 keV is a minor effect. The lower limit for electron induced atomic displacements is 145-200 keV [98,99]. However, Hinkley [100] has invoked a two-step energy transfer process to explain subthreshold defect generation in silicon. In this process, incident low energy electrons excite valence electrons, producing plasmons. These plasmons transfer their energy to the

lattice, eventually causing atomic displacements. The plasmon process also explains an experimentally observed [100] reduction in this threshold with increasing sample temperature. Since the SLEB produces sample heating, the plasmon process may contribute to the observed reduction in residual defects, such as observed in Figure 3.6.

Some support for this theory comes from comparison of peak trap concentrations of the beam annealed samples. If a strictly thermal regrowth and annealing process were responsible, one would observe a steady overall reduction in the trap concentration as beam power is increased. Double annealing should accelerate this trend. In fact, the largest peak trap concentrations and significant donor redistribution are observed in the 27.5 W/cm^2 double sweep case, which was certainly warmer during the second beam sweep. In this case, plasmon induced defects could explain the accelerated donor migration. No major donor redistribution effects are observed in samples treated with a single sweep.

3.3 Conclusions

The data show that relatively deeply amorphized Si layers can be recrystallized by swept-line electron beam processing. DLTS analysis shows that SLEB can reduce residual defect densities to levels well below that achievable by conventional furnace annealing. This is particularly true in the transition region between bulk and recrystallized material, where residual damage is resistant to high temperature annealing. It is significant that SLEB recrystallization can be effective without the use of additional furnace treatment. SLEB processes can also reduce bulk dopant redistribution effects which occur during furnace regrowth. These results do not represent the

best quality recrystallized material achievable, but they do demonstrate that SLEB processing can be a viable and effective alternative to rastered spot or pulsed area annealing techniques.

4. SLEB ANNEALING OF BF_2^+ IMPLANTED SILICON

This chapter extends the study of SLEB recrystallized amorphous silicon to include BF_2^+ implanted Si, in which the amorphization is created by the fluorine and acceptor doping is provided by the boron. Hall and Secondary Ion Mass Spectroscopy (SIMS) profiling reveal high electrical activation efficiency and only modest spatial redistribution. Unlike furnace annealed material, active boron is observed in the as-implanted amorphous-crystalline transition region. This can be important to the production of high quality implanted p-n junctions. Distribution effects of implanted fluorine are also explored, and these migration effects suggest that SLEB annealing does not produce crystal damage beyond the original implanted profile.

4.1 Experimental Procedure

The samples used in this study were Czochralski grown, phosphorus doped, $0.24 \Omega\text{-cm}$, $\langle 100 \rangle$ silicon. Implantation of BF_2^+ ions was performed at 150 keV to a fluence of $1 \times 10^{15} \text{ cm}^{-2}$ at room temperature. These conditions have been found sufficient to create an amorphous layer $\sim 1325 \text{ \AA}$ thick [80]. Beam annealing was accomplished as described in section 2.1. Samples of dimensions $1 \times 1.3 \text{ cm}$ were attached to the sample stage and translated at 0.32 cm/sec during annealing. An electron energy of 20 keV was used in this study.

After annealing, gold contacts were applied and a van der Pauw geometry mesa was defined by photolithographic techniques and plasma etching. Each slice accommodated either six or eight Hall patterns. Heat cycling after SLEB annealing did not exceed 300°C for 15 sec. Electrical carrier profiling was accomplished by double AC Hall measurements in conjunction with

chemical layer stripping, as described in section 2.3.3. Etch depths were measured at various points in the profile by using a Sloan Dektak mechanical stylus.

Samples used in electrical profiling measurements are subsequently used in SIMS profiling, to facilitate comparisons between atomic and electrically active profiles. Gold contacts were removed exposing processed implanted silicon which was unaffected by the electrical characterization. A maximum of 65 mils separated the regions which were electrically and chemically profiled. Secondary ion mass spectrometry was then performed using the Cameca AMS 3F ion microprobe. O_2^+ ions of 14.5 keV were employed for sputtering. Mass 11, 19, 28, and 31 signals were monitored during each profile by peak switching techniques. Concentration scales were established through reference to an unannealed standard. A Tencor mechanical stylus was used to measure crater depths and thus establish the depth scale.

4.2 Results

SLEB annealing was performed at power densities of between 19 and 64 W/cm^2 . SEM channeling pattern analysis indicated that all samples annealed in this range attained high quality near surface crystal order. Those annealed at the lowest power density, however, were too resistive to be Hall profiled. The net active carrier profiles for the three electron beam power density conditions are shown in Figure 4.1. The designation "X3" means that the sample was passed below a beam of the indicated power density three times. A ninety second interval was allowed between successive sweeps under the beam. We observe a general increase in the peak active boron concentration as the annealing power density increases from 30 to 64 w/cm^2 . The 64 w/cm^2 profile compares favorably with the as-implanted SIMS atomic

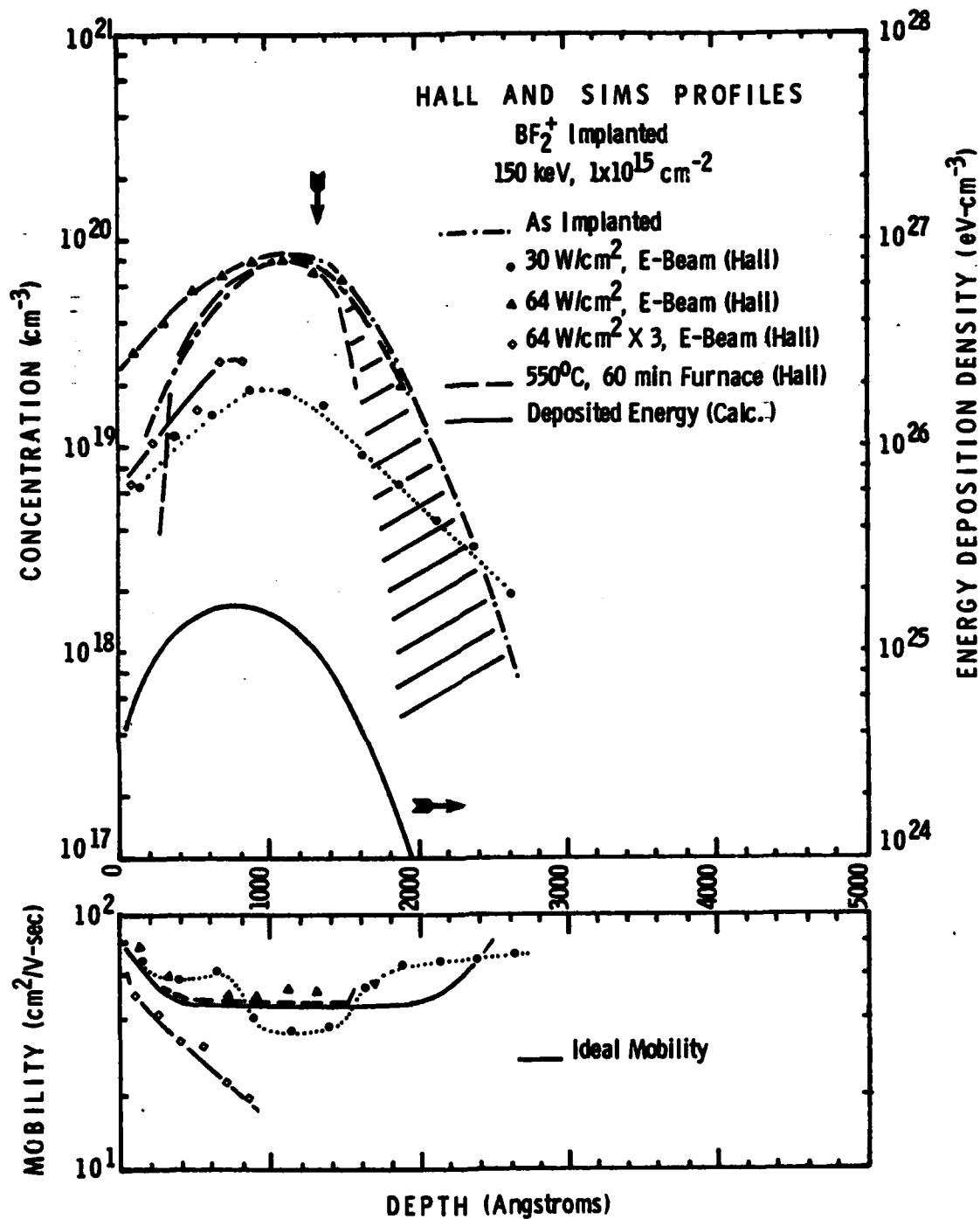


Fig 4.1. Net acceptor concentration and conductivity mobility profiles for BF_2 implanted silicon annealed at three SLEB power densities. Shown for comparison are the as-implanted atomic boron and corresponding "ideal" mobility profile. The furnace annealed profiles are due to Tsai et al. [80]. The calculated energy deposition density due to the implantation is also shown (right hand scale). The arrow marks the as-implanted amorphous-crystalline interface (see text).

boron profile except at depths less than 600 Å, where the electrical profile is larger by a factor of 2-3. After a triple sweep at 64 W/cm², the profile decays and becomes unmeasurable beyond 825 Å. Also shown are conductivity mobilities calculated assuming $\mu_c = 0.73 \mu_H$. The solid curve corresponds to mobilities achieved in bulk material at the concentration of the as implanted atomic profile [77, 101, 102]. Only the triple sweep profile deviates significantly from this bulk mobility profile.

Figure 4.1 includes an electrical profile measured by Tsai et al. [80, 81] in low temperature furnace annealed material, otherwise prepared under identical conditions. In the region beyond about 1400 Å, they observe an inactive tail (shaded region). This tail was found to correspond to the region which was heavily damaged, but not driven amorphous by the implantation. The original amorphous-crystalline boundary is marked by an arrow in Figures 4.1-4.5. In the SLEB annealed sample, relatively high levels of activation are measured out to 1900 Å, well into the inactive tail observed previously. In the 30 W/cm² sample, we find boron activation out to 2600 Å, nearly twice as deep as observed in 550°C furnace annealed material.

The actual distribution of boron is revealed in Figures 4.2-4.4. Here the electrical data of Figures 4.1 are compared with the as-implanted and beam annealed atomic profiles as measured by SIMS. The 30 W/cm² annealed material shows a very definite skewing while the electrical profile indicates poor activation efficiency. Activation becomes nearly complete in the 64 W/cm² case (Figure 4.3), where the SIMS and electrical data come into good agreement. The discrepancy between electrical and atomic profiles at depths shallower than 1100 Å is within combined measurement errors. Note that this atomic boron profile is skewed away from the as-implanted profile much less

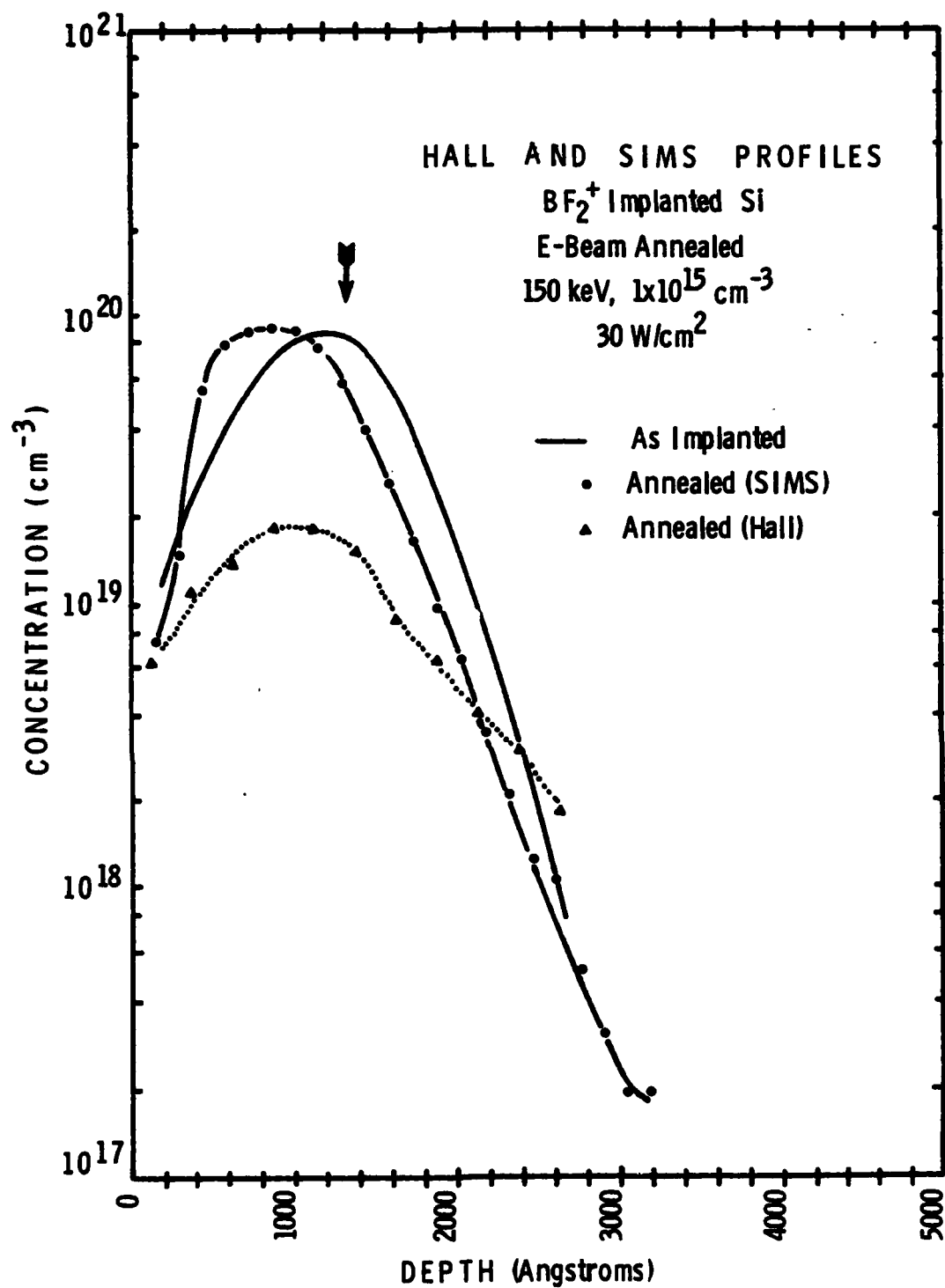


Fig. 4.2. As-implanted and annealed SIMS profiles for material processed at 30 W/cm². The net acceptor profile is included for comparison. Note the poor activation efficiency and shift in the SIMS profile towards the peak of damage.

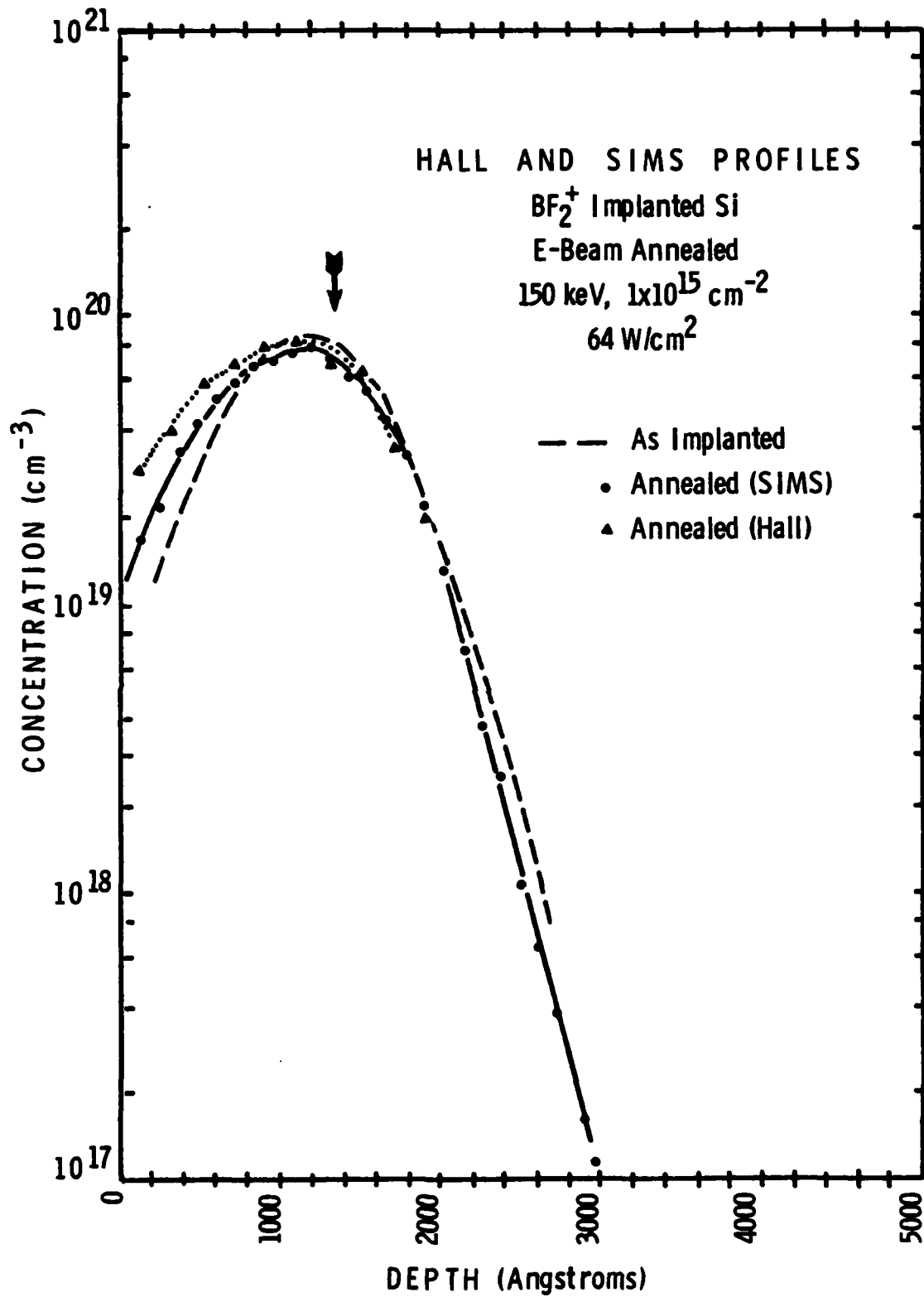


Fig. 4.3. SIMS and electrical profiles as in figure 4.2, but for material processes at 64 W/cm². Activation of boron is nearly complete with only minimal redistribution.

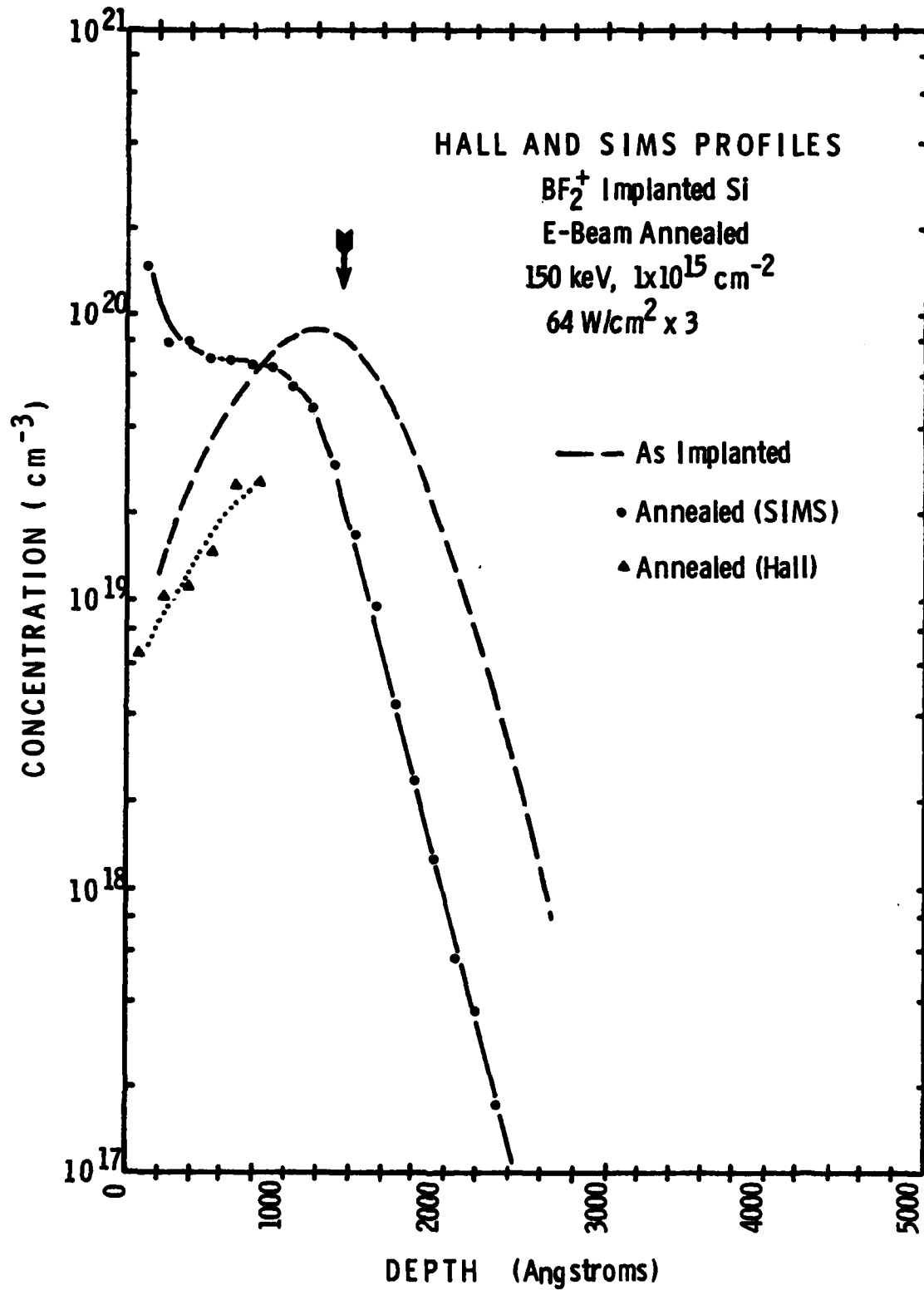


Fig. 4.4. SIMS and electrical profiles as in figure 4.2, but for triple pass, 64 W/cm^2 beam annealed material. Migration becomes significant. Near-surface activation efficiency is poor.

than is the corresponding profile in the 30 W/cm^2 case. Also note that the atomic boron concentration at depths less than 400 \AA actually exceeds the 30 W/cm^2 profile by factors of as much as 2. A much more pronounced surface accumulation effect occurs in the triple sweep case (Figure 4.4). This accumulation is accompanied by a large shift in the tail of the distribution toward the sample surface.

Similar SIMS profiles of implanted fluorine are presented in Figure 4.5. The beam annealed fluorine curves possess the general shapes of the corresponding boron SIMS profiles, with one rather striking exception. The 64 W/cm^2 profile shows an abrupt spike of fluorine, peaking at about 1300 \AA . Also shown is a fluorine profile measured by Tsai et al. [82] in material which was identically implanted but furnace annealed at 900°C for 30 minutes. This furnace annealed sample has a fluorine profile with two peaks, centered about the peak of the 64 W/cm^2 E-beam annealed profile.

4.3 Discussion

Of the effects observed here, the presence of electrically active boron in the original amorphous-crystalline transition region is perhaps the most significant. This can be understood in terms of the study of self-implanted amorphous silicon discussed in chapter 3. The data show that under proper conditions the defect concentration in the transition region can be reduced to levels below that achievable even by high temperature furnace processes. This explains the ability of the SLEB process to activate boron in this damaged region, as demonstrated in the 30 and 64 W/cm^2 cases. Recall from chapter 3 that annealing conditions producing reduced residual damage also produced minimal redistribution of dopant atoms. This accounts for the reduced skewing effects observed in Figure 4.3 as compared with

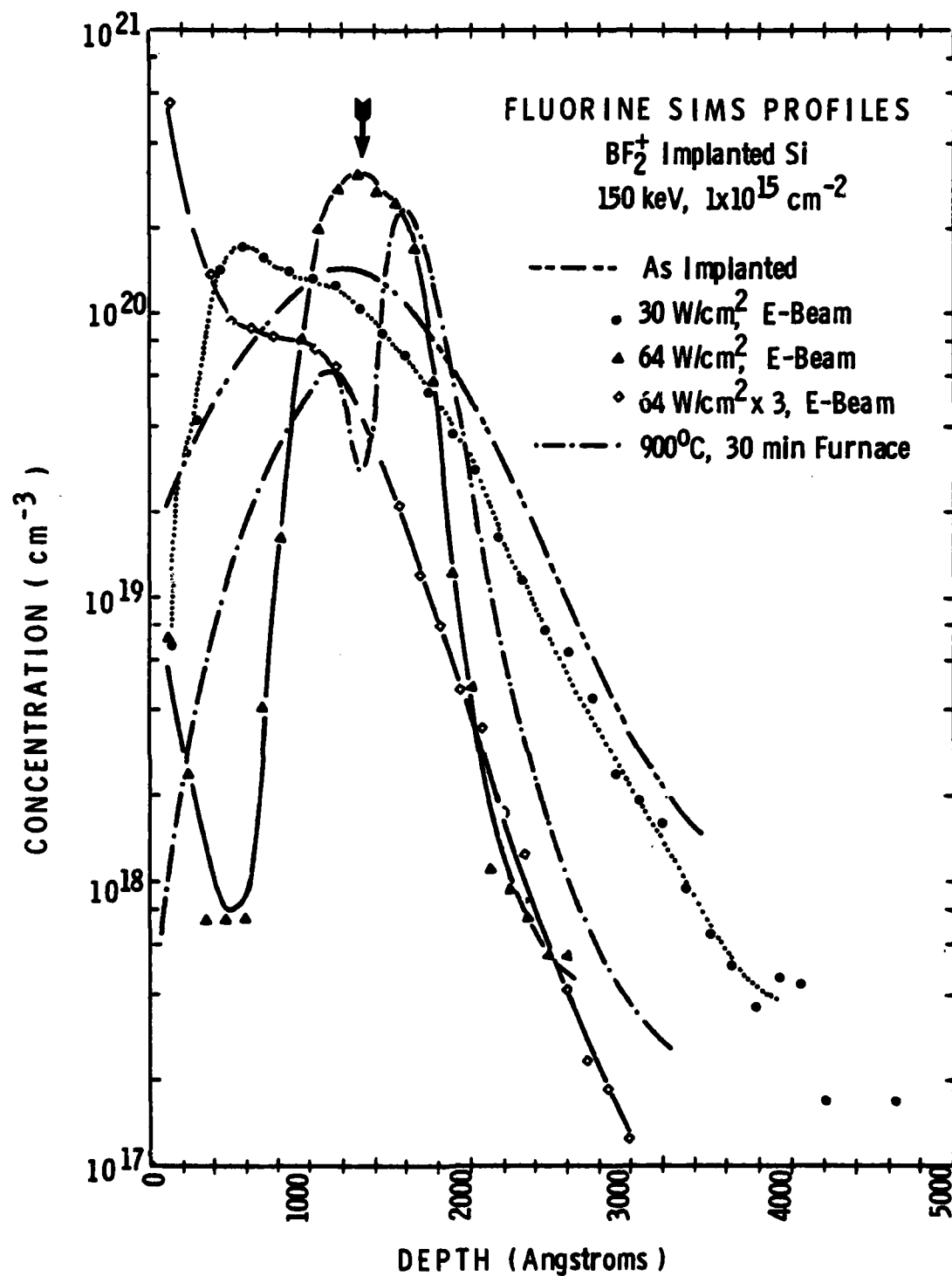


Fig. 4.5. Fluorine atomic profiles for as-implanted and SLEB annealed material. The 900°C, 30 min furnace annealed profile of Tsai et al. [82] is included for comparison. Note the large accumulation of fluorine at the original amorphous-crystalline transition region in the 64 W/cm^2 case.

Figure 4.2. In the latter case, defects have remained more numerous, resulting in the depressed electrical activity and poor mobility observed in the region 600-1600 Å. At even lower power density (19 W/cm^2), defects are so numerous that no activity can be detected at all.

In the 30 W/cm^2 case of Figures 4.1 and 4.2, it appears that the boron activation efficiency increases significantly in the region beyond 2200 Å. This occurs despite depressed boron activity in the regrown region shallower than 1600 Å. This effect can be explained by considering the energy deposition density profile of the implantation [65,102]. (Also shown in Figure 4.1.) At a depth of 2000 Å, the deposited energy has fallen by a factor of 10 from its value at the amorphous-crystalline interface. One should therefore expect a precipitous drop in the pre-annealing defect density in this region. The increased boron electrical activity is thus at least partially due to a local increase in the pre-annealing crystal quality.

It should also be noticed that the calculated peak of the deposited energy profile (and therefore the peak of the as-implanted damage profile) is shallower than the peak of the as-implanted atomic boron profile. (800 Å vs 1390 Å). It was shown in chapter 3 that in both furnace and SLEB annealed silicon, dopant atoms tend to migrate to areas of high defect density. All of the SLEB annealed profiles show a shift toward the peak of the calculated damage profile, the most pronounced effect occurring in the 30 W/cm^2 SIMS profile of figure 4.2. This is expected, since the most residual damage should occur in a sample annealed at lower beam power density. An analogous shift in the furnace annealed profile of Tsai et al. [80,81] is present in figure 4.1. In this case, however, dopant migration is also influenced by the motion of the amorphous-crystalline interface and by residual damage in the original interface region.

The study of self-implanted silicon (chapter 3) shows that large concentrations of defects and heavy migration of bulk dopant atoms into the as-implanted interface region occur in multi-sweep SLEB annealed material. This effect explains the triple sweep profile (figure 4.4). Heavy residual damage results in depressed values of mobility and the large near surface atomic boron concentration, due to migration of boron to this damage. Migrating bulk phosphorus atoms can compensate implanted boron atoms, depressing the active profile.

Verification of phosphorus migration by SIMS is difficult because of a large background mass 31 signal due to SiH. The lower limit of SIMS phosphorus detection is estimated to be $3 \times 10^{20} \text{ cm}^{-3}$. Therefore, effects of phosphorus redistribution during annealing may be studied indirectly. For example, we note that the annealed SIMS boron profile of figure 4.4 falls with increasing depth, while the electrical profile climbs. This alone would imply a general decrease in defect density, which should be associated with an increase in mobility. We observe, for example, that the 30 W/cm^2 mobility profile improves between 100 and 600 Å, and beyond 1600 Å (figure 4.), where the electrical and SIMS profiles are in better agreement. In contrast, the triple sweep mobility profile (figure 4.1) falls continuously. If a significant quantity of electrically active donors were present within the measured profile, compensation of the boron acceptors would occur, along with a decrease in mobility, as observed here. The fact that this effect occurs in the triple sweep case is consistent with the observation in chapter 3 that donor migration is most severe in multi-sweep annealed material.

Fluorine redistribution effects in furnace annealed BF_2^+ implanted silicon have been explained in terms of recrystallization-induced migration,

gettering by radiation damage, and thermal outdiffusion.[82] Since recrystallization times are short in beam annealing processes, one would expect only the latter two factors to be significant in this study. Motion of the amorphous-crystalline interface influenced the damage and dopant profiles of only the lowest temperature furnace annealed sample (section 3.2). The shifting of the 30 W/cm^2 fluorine profile (figure 4.5) can be explained in terms of gettering at the same residual implantation-induced damage we believe responsible for the corresponding boron redistribution. At 64 W/cm^2 , the lack of fluorine at depths shallower than 1100 \AA seems to indicate that much of this implantation-induced damage has been annealed away. The more stable damage at the as-implanted amorphous-crystalline interface dominates the fluorine migration in this case. There is excellent agreement between the location of the SIMS fluorine peak of this work and that of the as-implanted interface measured by Tsai et al.[80-82] (depth 1325 \AA). These authors previously accounted for the two peak nature of the furnace annealed fluorine profile by the motion of the interface region during recrystallization. As mentioned above, we do not observe such dual peak phenomena in E-beam annealed material. Tsai et al.[65] have also demonstrated that fluorine gettering effects are strongest on the bulk side of the as-implanted interface. The slight skewing of the 64 W/cm^2 profile coincides with their observation.

In the multi-sweep case, the same damage-aided diffusion effect responsible for the large surface boron concentrations appears to produce the observed fluorine distribution. Although fluorine outdiffusion appears likely, the present studies do not demonstrate this conclusively. The

flattening of the multi-sweep curve between 500 and 1000 Å tends to indicate that some residual as-implanted interface damage may still be affecting the final fluorine distribution.

Finally, it should be noted that the tails of the fluorine profiles move progressively closer to the surface with increasing E-beam treatment. Furnace annealing studies[81] have shown that radiation damage will effectively getter fluorine, even if it is as much as 3000 Å deeper than the peak of the as-implanted fluorine profile. Therefore, it is unlikely that any significant regions of damage exist deeper than the peak of the as-implanted fluorine profile to the limit of the deepest SIMS analysis (7000 Å). We contend, therefore, that even triple sweep SLEB does not produce bulk damage beyond the as-implanted profile.

4.4 Conclusions

At the lowest power levels studied here, electron beam heating is sufficient only to grossly reorder the lattice. At higher annealing power, the defect density is reduced sufficiently to produce partial electrical activation. The residual damage from the implantation strongly influences the final atomic distributions. Under more intense beam conditions, this residual implantation damage is more completely annealed and diffusion effects become less influential. The more annealing-resistant damage at the original amorphous-crystalline transition region strongly getters implanted fluorine. Finally, under multiple sweep annealing conditions, the beam induces large defect concentrations in the region shallower than the peak of the implanted profile. Damage aided diffusion processes skew the profiles toward the surface. The possibility of some bulk dopant involvement and of actual outdiffusion exists, but cannot be confirmed through this study.

The data are consistent with recrystallization and dopant activation in amorphous, BF_2^+ implanted silicon by swept line electron beam annealing. Under proper conditions, acceptor profiles with good electrical activity and mobility are observed, and redistribution effects are minimized by the use of SLEB annealing. This study also demonstrates that SLEB processing can produce electrical activity in the amorphous-crystalline transition region, which has not been achieved by low temperature furnace processes. The influence of residual radiation damage on the redistribution of the implanted species is consistent with that observed in furnace annealed material. Our results show that SLEB annealing does not produce bulk lattice damage out to 5000 Å beyond the peak of the as-implanted profile.

5. SLEB ANNEALING OF $\text{GaAs}_{1-x}\text{P}_x$

In this chapter the investigation of SLEB annealing is extended to include the $\text{GaAs}_{1-x}\text{P}_x$ system. This technique can effectively activate implanted dopants and the nitrogen isoelectronic trap with minimal redistribution of impurities or implantation related damage. In the first half of the chapter, annealing effectiveness will be explored with photoluminescence techniques. The second half will be devoted to characterization of $\text{GaAs}_{1-x}\text{P}_x$ p-n junctions.

5.1 Study of SLEB Annealed $\text{GaAs}_{1-x}\text{P}_x$: N by Photoluminescence

SLEB annealing effectiveness was studied initially by photoluminescence techniques. This effort was pursued in cooperation with Dr. T. Yu.[91] The relative ease of evaluation allowed a large range of annealing parameters to be explored. The relative strength of band-edge and nitrogen trap related emissions were used as a measure of annealing effectiveness. Stripping techniques were used to evaluate migration of nitrogen and implantation related damage.

5.1 Experimental procedures

All crystals used in this study were Monsanto $\text{GaAs}_{1-x}\text{P}_x$ n-type VPE layers of $\langle 100 \rangle$ orientation, grown on n^+ GaAs (for $x=0.4, 0.5$) or n^+ GaP (for $x=0.65$) substrates. Epitaxial layer thicknesses of approximately 120 μm included a 20-50 μm graded composition region. The surface of the $x=0.4$ and 0.5 material was chemically etched to a depth of 3 μm to ensure uniform crystal composition. The 20 μm just below the surface of the $\text{GaAs}_{0.35}\text{P}_{0.65}$ layers were doped with nitrogen during growth. This

doped layer was etched away on samples to be used in N-implantation studies. The photoluminescence emission from all of the etched surfaces was measured prior to implantation for reference.

Nitrogen ($^{14}\text{N}^+$) implantations were performed at room temperature at 200 keV as described in section 2.2. Ion doses were chosen to produce peak concentrations of $10^{17} - 10^{20} \text{ cm}^{-3}$, as determined by LSS calculations.[104] Prior to electron beam annealing, 1000 Å of SiO_2 was deposited on the implanted surface by the oxidation of silane. Depositions were typically performed at 450°C for 6 min.

Electron beam annealing was performed as described in section 2.1. In this study, the beam energy was maintained at 20 keV, and the table translation speed at 0.25 cm/sec. Actual on-sample beam power densities were not measured. Rather, total electron current leaving the gun (I_b) was used as a relative measure of beam strength.

Conventional furnace annealing was performed on similar samples for comparison. SiO_2 films of thickness 1500 Å were deposited on both sides of these samples to prevent decomposition during high-temperature processing. Annealing was performed in flowing high-purity argon in a silica-lined furnace. Each anneal required 30 minutes at selected temperatures from 600° to 1000°C . These procedures for furnace annealing of N-implanted $\text{GaAs}_{1-x}\text{P}_x$ have been discussed in detail previously.[105-110]

Prior to photoluminescence measurements, the protective oxides were removed with 30% HF. Samples were then mounted in a Janis "Super Varitemp" gas exchange liquid-helium cryostat and held at 5 K. The photoexcitation was provided by the 4880 Å line of a Coherent Radiation 52-G Ar ion laser. An average incident power density of 10^3 W/cm^2 was used.

The front surface luminescence signal was focused onto the slit of a 1/2-m Spex 1302 double grating monochromator, and was detected by an RCA C31034 (extended S-20 response) photomultiplier using lock-in amplifier techniques. The emission spectra are uncorrected for system response.

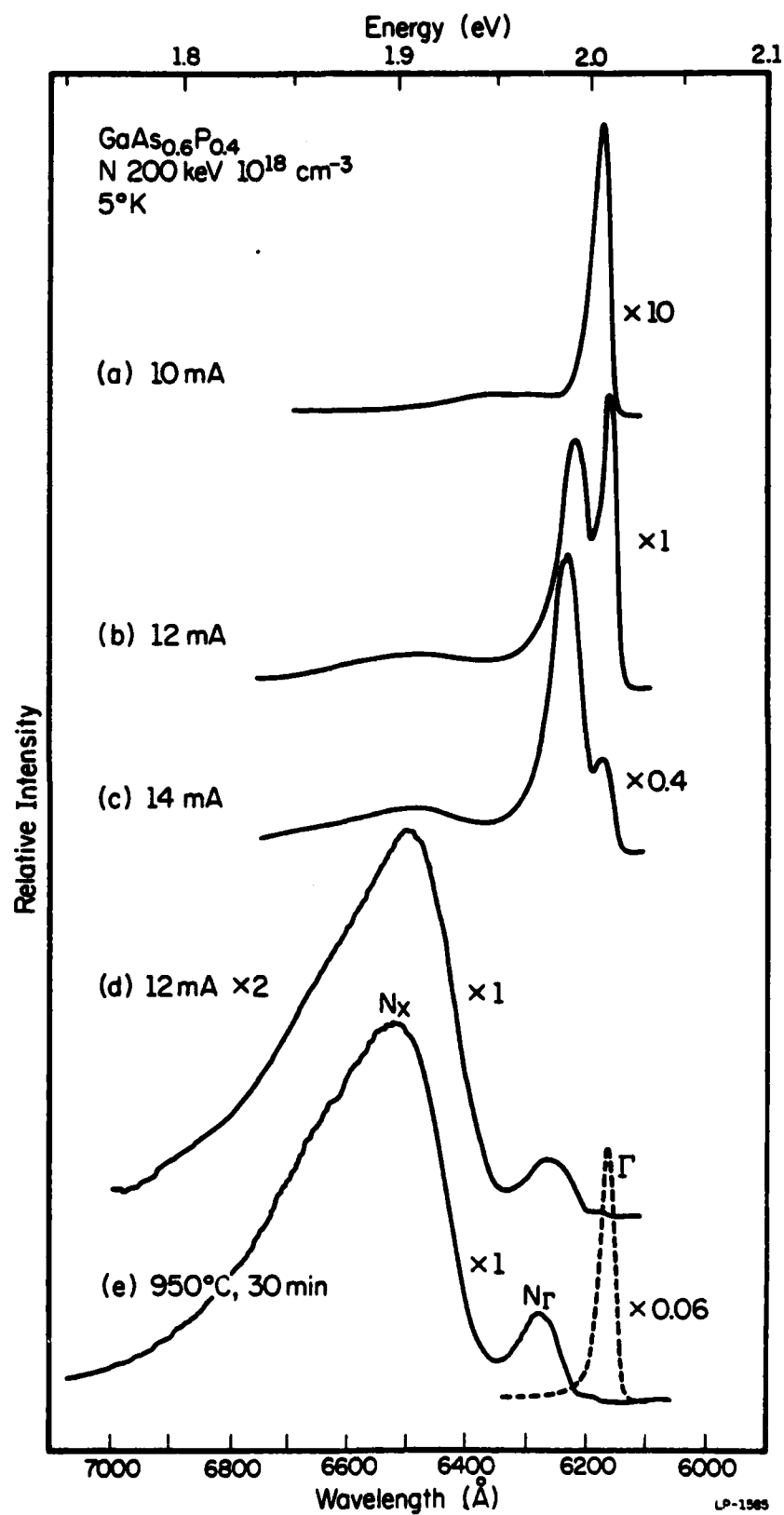
Successive layer removal required for the profiling study was accomplished by chemical etching with a solution of 5 H_2SO_4 : 1 H_2O_2 : 1 H_2O . The etching time was controlled to remove layers $\sim 600 \text{ \AA}$ thick. Actual thicknesses removed were determined by Dektak mechanical stylus measurements of selective etched steps.

5.1.2 Results and discussion

5.1.2.1 Direct gap composition, $x=0.40$

Photoluminescence spectra for 10^{18} cm^{-3} nitrogen implanted samples as a function of annealing electron beam current (I_b) are shown in figure 5.1. We observe as much as a 30 \AA variation of the near band-edge emission across any given sample owing to slight variations in alloy composition. This accounts for the small peak misalignments observed in spectral data. Shallow donor band-edge emission Γ ($\lambda = 6160 \text{ \AA}$) becomes significant after annealing with $I_b = 10 \text{ mA}$ (curve a). As the annealing current is increased, strong nitrogen activation is indicated by an increase in N_Γ ($\lambda = 6250 \text{ \AA}$) [105,106] and N_x ($\lambda = 6500 \text{ \AA}$) [105-108] emission. At $I_b = 15 \text{ mA}$, we observe localized surface melting and a reduction of emission from these melted areas. We observe, however, that significant increases in N_x emission are possible with two sweeps of the beam with $I_b = 12 \text{ mA}$. N_x emission becomes dominant (curve d) and total integrated emission becomes comparable to that of the best furnace annealed samples (curve e). Annealing characteristics of samples with peak nitrogen concentrations of 10^{19} and 10^{20} cm^{-3} are similar.

Fig 5.1. Photoluminescence spectra of $\text{GaAs}_{0.6}\text{P}_{0.4}$ nitrogen implanted to a peak concentration of 10^{18} cm^{-3} and swept-line electron beam annealed at the indicated total beam current (I_p). Emission from unimplanted nitrogen free material is shown for comparison (dashed line). (After Yu [91].)



For peak nitrogen concentrations of 10^{17} cm^{-3} , the maximum emission is observed after a single annealing pass at $I_b = 12 \text{ mA}$. The N-induced emission intensity increases slightly with increasing I_b or multiple sweeping, while the total integrated intensity remains the same. This suggests that much of the lattice disorder introduced by implantation has been removed at $I_b = 12 \text{ mA}$, but that larger I_b is necessary for efficient nitrogen activation.

The data for total integrated emission intensity versus furnace annealing temperature agree generally with those observed by Anderson et al. [109,110]. The integrated intensities from samples electron beam annealed under optimum conditions ($I_b = 12 \text{ mA}$, two passes) are comparable or superior to furnace annealed samples at their individual optimum conditions. This is true for all peak concentrations of implanted nitrogen. A high degree of nitrogen substitution is evident in the case of 10^{19} cm^{-3} for which total integrated emission exceeds that of unimplanted direct-gap materials.

5.1.2.2 Indirect gap composition, $x=0.50$

The annealing characteristics of indirect-gap $\text{GaAs}_{0.5}\text{P}_{0.5}$ are very similar to those obtained for direct gap $x=0.40$ material. A weak D_0^x ($\lambda = 5970 \text{ \AA}$, exciton bound to neutral donor) emission appears after annealing with $I_b = 10 \text{ mA}$. As the annealing current is increased, the N_x emission ($\lambda = 6350 \text{ \AA}$) strengthens until it saturates after a double anneal at $I_b = 12 \text{ mA}$ (curve d). Integrated intensity obtained under this annealing condition is comparable to that obtained from optimum furnace annealing (950°C , 30 min). This trend holds for all nitrogen concentrations studied here.

The spectral shapes observed are essentially the same as furnace annealed samples for all nitrogen concentrations studied.

5.1.2.3 Indirect gap composition, $x=0.65$

Similar annealing studies were performed on $\text{GaAs}_{0.35}\text{P}_{0.65}$ samples. D_o^x emission ($\lambda=5810 \text{ \AA}$) and N_x emission ($\lambda=6010 \text{ \AA}$) become strong under the same annealing conditions as observed in $x=0.4$ and 0.5 material. Again we find optimum E-beam annealing to produce N_x emission intensity comparable to optimum furnace annealed samples. We also find the peak intensity of 10^{19} cm^{-3} implanted material to exceed that obtained from similar material doped with nitrogen during growth. This demonstrates the effectiveness of the electron beam process in nitrogen activation and damage annealing.

5.1.2.4 Optical depth Profiling

Depth profiling studies[91] were performed on $x=0.4$ and 0.5 material with peak nitrogen concentrations of 10^{18} cm^{-3} . The $x=0.65$ material was not studied because of its unsatisfactory etching characteristics. Figure 5.2 shows total integrated emission intensity for both annealed and unannealed profiles with $x=0.4$. Annealing conditions were chosen to produce maximum integrated emission. Variation in intensity was found not to exceed 20% across any etched region.

The unannealed $x=0.4$ material produces no detectable emission until the first $20 \text{ }\mu\text{m}$ have been removed. Band-edge Γ emission is observed to increase until $0.58 \text{ }\mu\text{m}$, where the intensity recovers to the level of the unimplanted material. The damage profile for this implantation is predicted by Brice[103] to have an asymmetrical shape peaking at 2600 \AA . The damage remaining at $0.58 \text{ }\mu\text{m}$ should be only 9% of the peak damage. Our measurements show that the damage profile before annealing is no deeper than predicted. For annealed samples, the total photoluminescence emis-

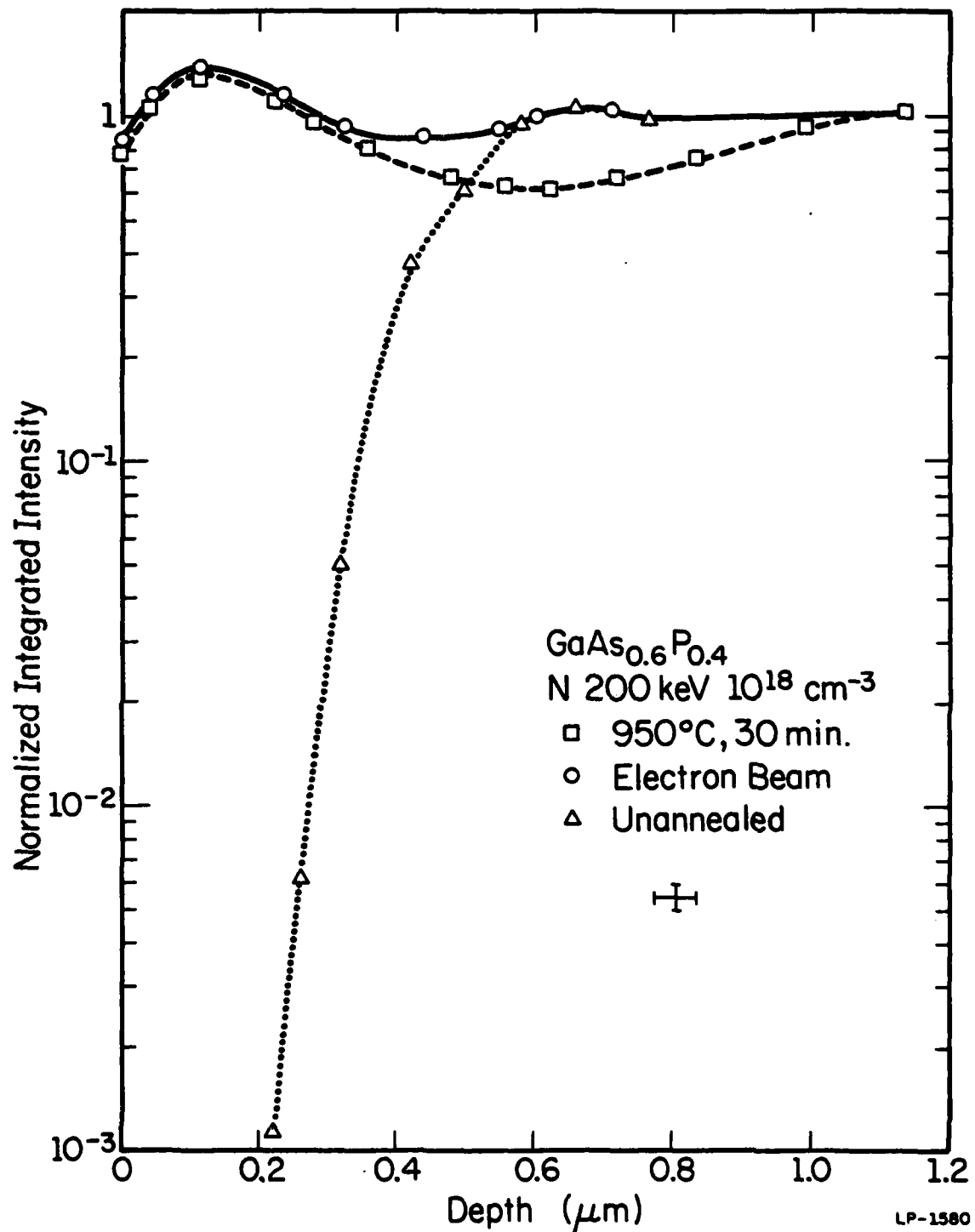


Fig 5.2. Depth dependence of the total photoluminescence intensity (5°K) of GaAs_{0.6}P_{0.4} nitrogen implanted to 10¹⁸ cm⁻³ peak concentration. Dashed curve corresponds to furnace annealed material (950° C, 30 min), and solid line to SLEB annealed material (I_b=12 mA, double pass). Data are normalized to unimplanted, unannealed nitrogen-free material. (After Yu [91].)

sion intensity in the first 0.2 μm is found to be comparable with that of the unimplanted materials, owing to the high concentration of active nitrogen in this region. Beyond this point emission decreases, with recovery to the level of unimplanted material occurring at 0.6 and 1.2 μm , respectively, for the electron beam and furnace annealed samples. The same general trend is found in $x=0.5$ material. These dips are due to a combination of reduced nitrogen concentration and residual implantation-induced damage. The unannealed sample shows no significant emission degradation at depths of 0.6 to 1.2 μm . The degradation of the furnace annealed samples in this same region may therefore be attributed to diffusion of defects. The short duration of the electron beam anneal prevents significant damage diffusion, as demonstrated by the more rapid recovery of emission with depth into the sample.

In addition to providing information about defect distributions, these optical profiling measurements can be used to study the effects of annealing on the implanted nitrogen profile.[109] The photoluminescence intensities obtained after successive etch steps depend upon the overlap of the optically generated excess carrier distribution and the nitrogen profile. The active impurity profiles may be deduced approximately if the excess carrier profile is known. Here we use the expression of $\delta p(x)$ due to Williams and Chapman.[111] For $x=0.4$ material we take $\alpha(\lambda=4880 \text{ \AA}) = 4.2 \times 10^4 \text{ cm}^{-1}$ for 5°K. For $x=0.5$, we take $\alpha(4880 \text{ \AA})$ to be $3.3 \times 10^4 \text{ cm}^{-1}$ at this same temperature.[91] The diffusion lengths are expected to be very short compared to the absorption lengths due to rapid trapping at the

N center and the effects of lattice damage. We use a radiative lifetime for the N-trap to be about 100 ns[112], a surface recombination velocity of $5 \times 10^5 \text{ cm-s}^{-1}$, and a diffusion length of $\sim 0.2 \text{ }\mu\text{m}$.

The measured N_x emission profiles for $x=0.4$ and 0.5 material are shown in figures 5.3 and 5.4 respectively. Also shown are the theoretical N_x emission profiles based on the overlap of the estimated excess carrier distribution and a simple Gaussian as-implanted nitrogen distribution ($R_p=3700 \text{ }\text{\AA}$, $\Delta R_p=1150 \text{ }\text{\AA}$) predicted by LSS theory. This computed profile has a peak at $\sim 1200 \text{ }\text{\AA}$ for both $x=0.4$ and 0.5 compositions. There is good agreement between the theoretical active nitrogen profile and the electron beam annealed profile. The N_x emission in both $x=0.4$ and 0.5 E-beam annealed material ceases abruptly after removal of the implanted layer. This is consistent with the minimal diffusion expected in solid phase transient annealing which has been demonstrated in chapters 3 and 4.

Although active nitrogen profiles for the furnace annealed samples reach a peak at the same depth as the E-beam annealed samples, they display detectable N_x emission to depths of 0.8 and 1.2 μm respectively, for $x=0.4$ and 0.5 material. For $x=0.4$ material, 0.8 μm actually represents the point where we are no longer able to discern N_x emission above the donor-acceptor pair and N_T emission. Since we observe N_T emission to a depth of 1.2 μm in the $x=0.4$ case, it is likely that nitrogen has diffused as deeply as in the $x=0.5$ composition material. Since pair emission is negligible in the case of indirect material and there is no N_T inter-

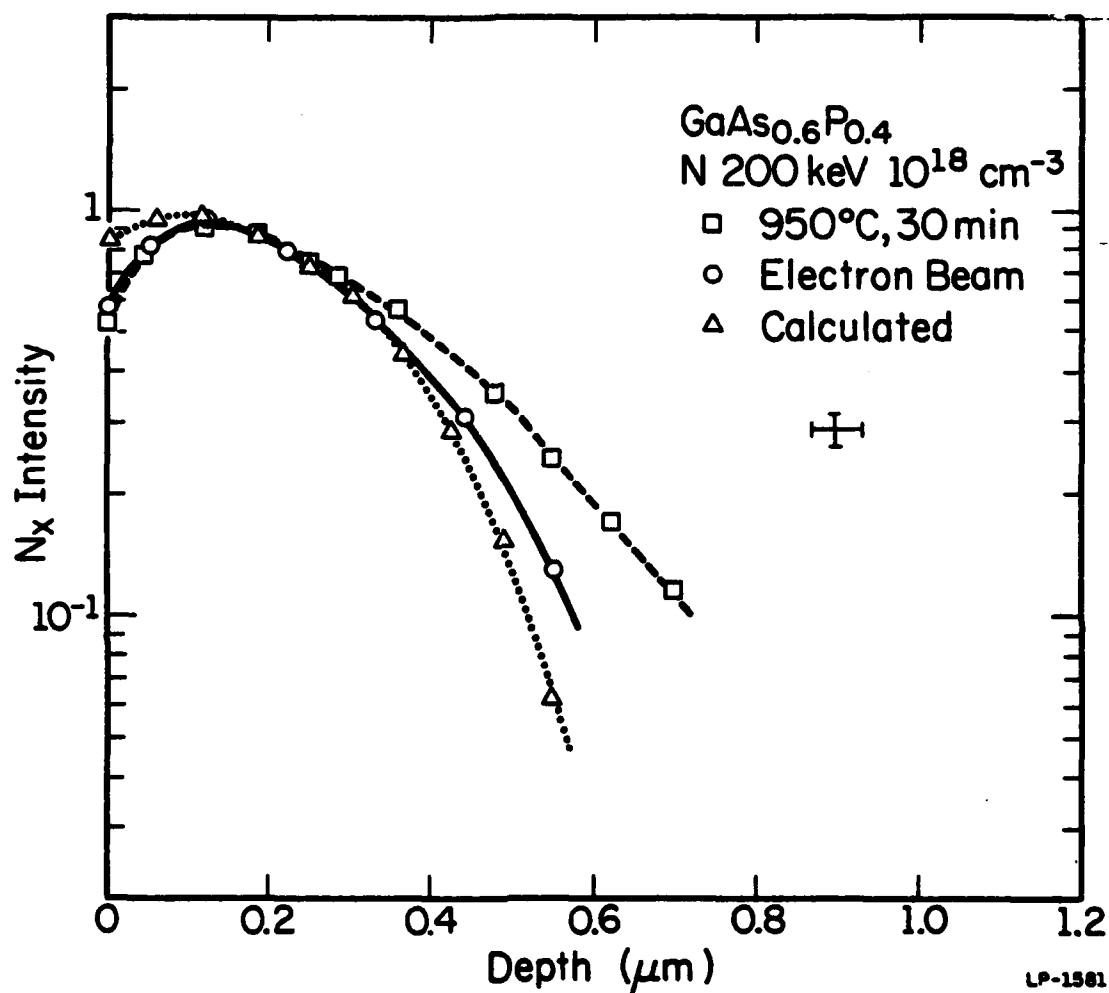


Fig. 5.3. Depth dependence of the N_x emission intensity (5°K) of GaAs_{0.6}P_{0.4} nitrogen implanted to a peak concentration of 10¹⁸ per cm³. The dashed curve corresponds to furnace annealed material (950° C, 30 min), and the solid curve to SLEB annealed material (I_b=12 mA, double pass). The theoretical emission profile (dotted line) is explained in the text. (After Yu [91].)

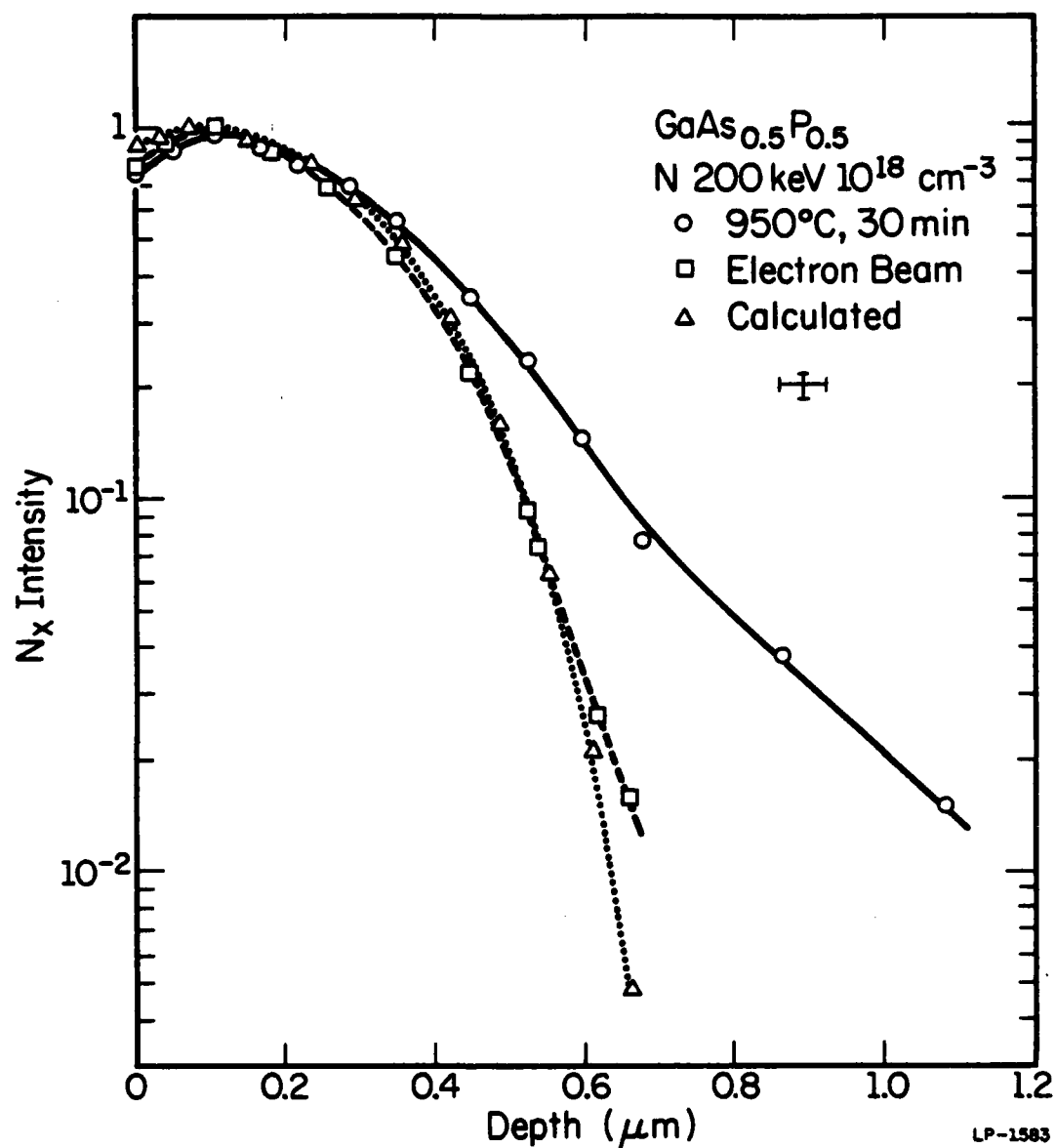


Fig 5.4. N_x emission intensity profiles as in fig. 5.3, for GaAs_{0.5}P_{0.5} (indirect gap composition), nitrogen implanted to a peak concentration of 10¹⁸ cm⁻³. Notice the close agreement between the SLEB profile (I_b=12 mA, double pass) and the theoretical emission profile. Also notice the spreading of the furnace annealed profile. (After Yu [91].)

ference, we can unambiguously define the limit of nitrogen diffusion with the N_x profile. We estimate that the diffusive tails contain about 10% of the total implanted nitrogen for either composition.

5.2 Study of SLEB Annealed $GaAs_{0.35}P_{0.65}$ p-n Junctions

The study described in the preceding section shows the effectiveness of SLEB processing in activating N-implanted $GaAs_{1-x}P_x$. However, in the case of $x=0.65$ composition material, migration of nitrogen and damage migration effects could not be verified. In addition, the N_x intensity profiles discussed above must rely upon a calculated excess carrier profile, rather than some more direct means. To investigate this particular composition further, a series of $GaAs_{0.35}P_{0.65}$ p-n junctions were fabricated which incorporated implanted nitrogen. The electrical and optical characteristics of these devices show that SLEB annealing does indeed reduce migration effects of implantation related damage and nitrogen when compared with conventional furnace annealing.

5.2.1 Experimental procedure

Material used in this portion of the study was identical to the $x=0.65$ composition $GaAs_{1-x}P_x$ used for the photoluminescence experiments. As before, the 20 μm nitrogen doped epitaxial layer was removed prior to processing. After cleaning, samples were subjected to two beryllium implantations of 1×10^{14} ions/cm² at 50 keV and 6.7×10^{14} ions/cm² at 130 keV. A single 3×10^{14} ions/cm², 220 keV nitrogen implantation was then made. The calculated as-implanted distributions are shown in figure 5.5. The Be doses and energies were chosen to produce the retrograde acceptor profile studied by Chatterjee.[113] This distribution was a compromise between a uniform and buried gaussian profile. The former

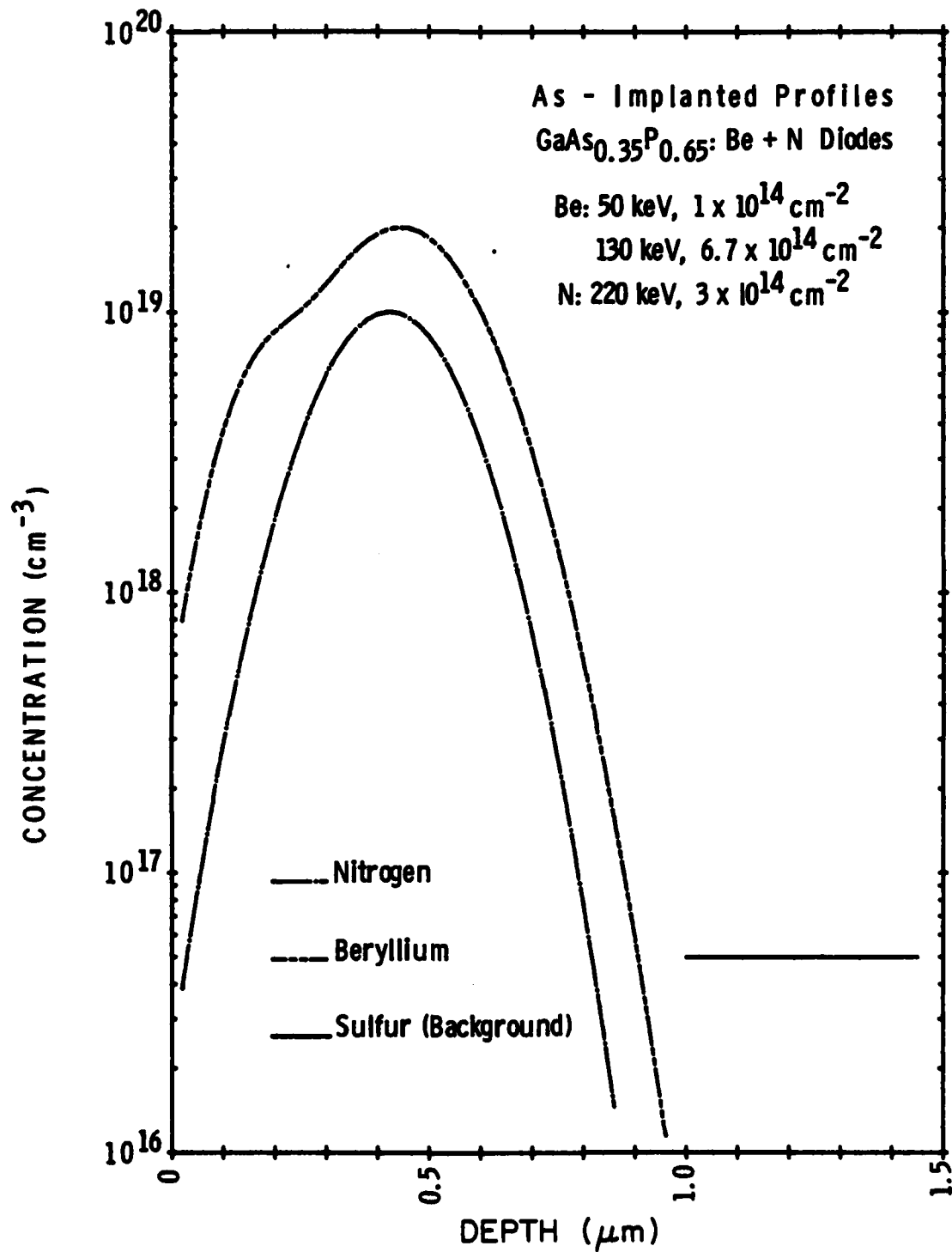


Fig. 5.5. Calculated as-implanted profiles of nitrogen and beryllium for the GaAs_{0.35}P_{0.65} p-n junctions. Also shown is the level of the substrate dopant concentration.

distribution simulates the zinc profile created in conventional furnace diffusion, whereas the latter produces a built-in retarding field for injected electrons, reducing surface recombination effects. Chatterjee's studies have suggested that the retrograde acceptor profile does indeed reduce surface recombination and results in the best light intensity (L) versus current characteristics among similar implanted direct-gap GaAsP light emitting diodes. The as-implanted nitrogen profile in figure 5.5 is entirely contained within the implanted acceptor profile.

Following implantation, samples were cleaned and encapsulated with $\sim 1500 \text{ \AA}$ of rf plasma deposited silicon nitride.[114] Some of the material was then annealed in silica lined furnace tube under flowing high purity argon gas. A 30 minute, 950°C annealing cycle was selected, corresponding to the optimal conditions for annealing nitrogen implanted to this level.[91] Chatterjee[113] demonstrated successful annealing of Be-implanted direct gap GaAsP with these approximate implantation conditions at temperatures about 50°C less than used here. Samples for E-beam annealing were prepared as described in section 2.1. A table translation speed of 0.60 cm/sec was used for these samples. Although a number of different beam power density combinations were tried, the devices described here were processed with five passes of the SLEB with 18 W/cm^2 peak power density.

Prior to annealing, all implanted samples possessed a frosted opaque appearance. After the first pass of the SLEB, the samples returned to their original orange transparent condition. This observation tends to indicate that good crystallinity had returned after this level of annealing. A survey of photoluminescence of this Be + N implanted material agreed with findings of section 5.1. In general, restoration of crystal order

occured after only a single pass of the SLEB, but complete nitrogen activation required more intense and repetitive E-beam treatment.

After annealing, samples were solvent cleaned and stripped of nitrides. Al contacts were then defined on the implanted surface by AZ photoresist lift-off technique. On the back surface, Au-Ge contacts were produced with Ni overlay by double evaporation through a shadow mask. The samples were then sintered in flowing H_2 for a total of approximately 90 secs. Maximum temperature reached during the contact processing did not exceed $400^\circ C$. Individual devices were formed by scribing and cleaving. Devices were mounted in pairs on T0-18 headers and thermocompression lead bonded.

5.2.2 Results and discussion: electrical characteristics

Current-voltage measurements were made on these devices with a computer controlled Hewlett Packard 69321 B power supply and a Keithley Model 480 Picoammeter. Temperature dependent measurements were made in a vacuum chamber equipped with an Air Products closed-cycle He refrigerator unit. Room temperature current density (J) versus voltage characteristics of the best furnace and SLEB annealed devices are shown in figure 5.6.

In the low forward bias region, both devices display conduction with an ideality factor n of 2.* The furnace annealed device shows a marked departure from this behavior at $J=10^{-5} A/cm^2$, and yet further bend-over occuring at forward bias exceeding 2.5 volts. This departure from

* n is the ideality factor commonly used in the diode expression

$$J = J_s \exp(qV/nkt)$$

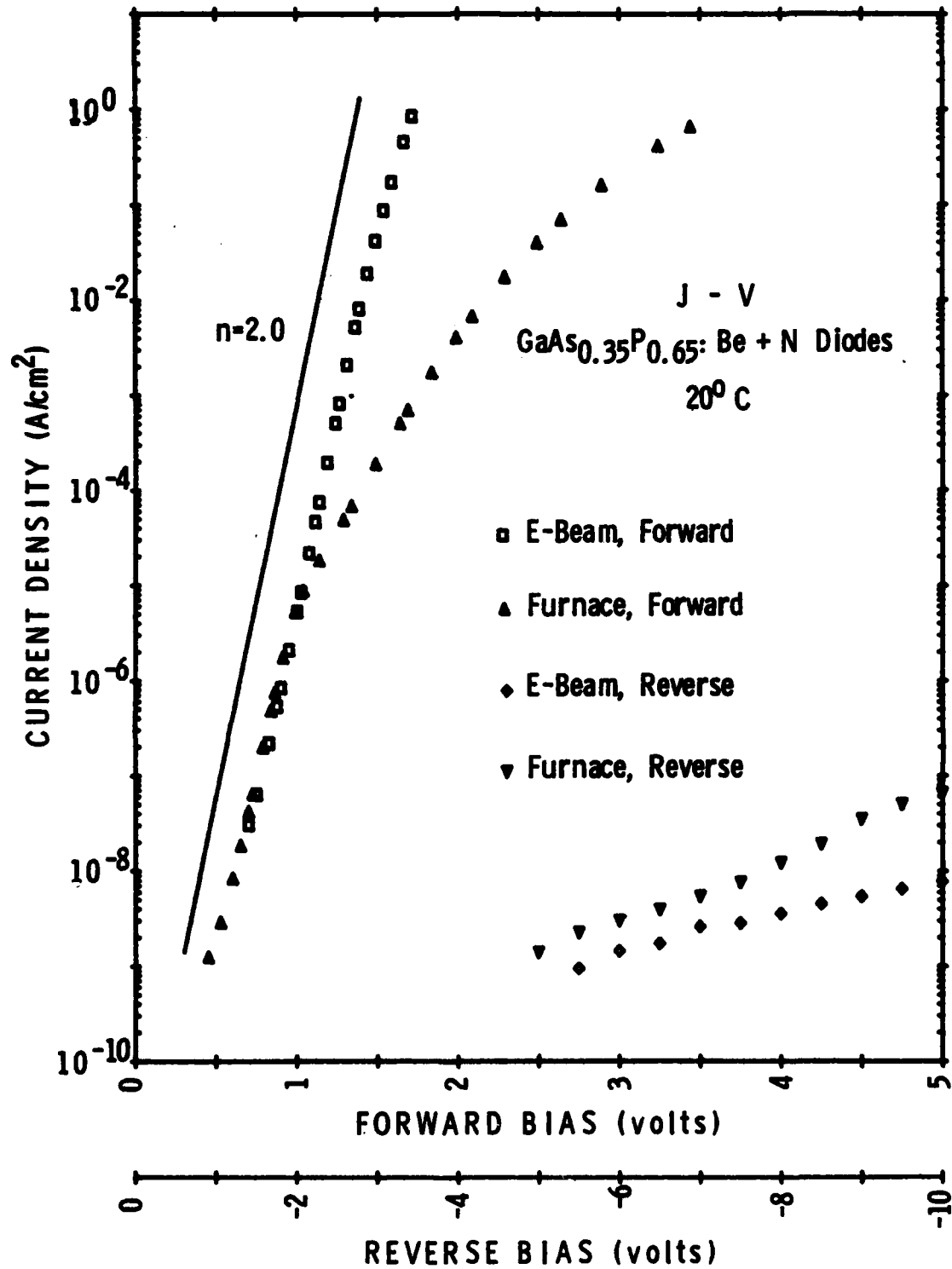


Fig. 5.6. Current density versus voltage characteristics for the best GaAs_{0.35}P_{0.65}:Be + N diodes annealed by SLEB and furnace techniques.

$n=2$ conduction occurs consistently for all 5 furnace processed devices between 10^{-5} and 10^{-6} A/cm². The e-beam device characteristic shows $n=2$ conduction nearly to the limit of current measurement. Some slight roll-off is seen at the highest measured currents, presumably due to series resistance effects. All but one of the eight beam processed devices show a predominance of current due to recombination in the space charge layer. The characteristics of the furnace annealed devices indicate the presence of series resistance in the junction.

Eliminating the worst device from each set, the average $V_r=10$ V reverse current density is about 4×10^{-7} A/cm² in the furnace annealed devices and 6×10^{-8} A/cm² in the SLEB case. In general, the furnace annealed devices show a softer reverse bias characteristic.

Temperature dependent J-V data for devices T4B (furnace) and ElB (SLEB) are presented in figures 5.7 and 5.8 respectively. Notice in figure 5.7 a set of parallel lines has been drawn through the approximate straight line portion of each curve, beginning just above the "knee" discussed earlier. The obvious temperature independence indicates conduction predominated by tunneling mechanisms.[115,116] One would therefore expect a relatively large number of states to be available within the bandgap at the n-type edge of the space charge region in these devices. The doping level of the substrate material is not sufficiently large to expect valence bandtail effects.[117] A similar set of parallel lines obviously cannot be drawn through the data of device ElB. Calculated ideality factors of the beam annealed device vary around 2 for all temperatures studied.

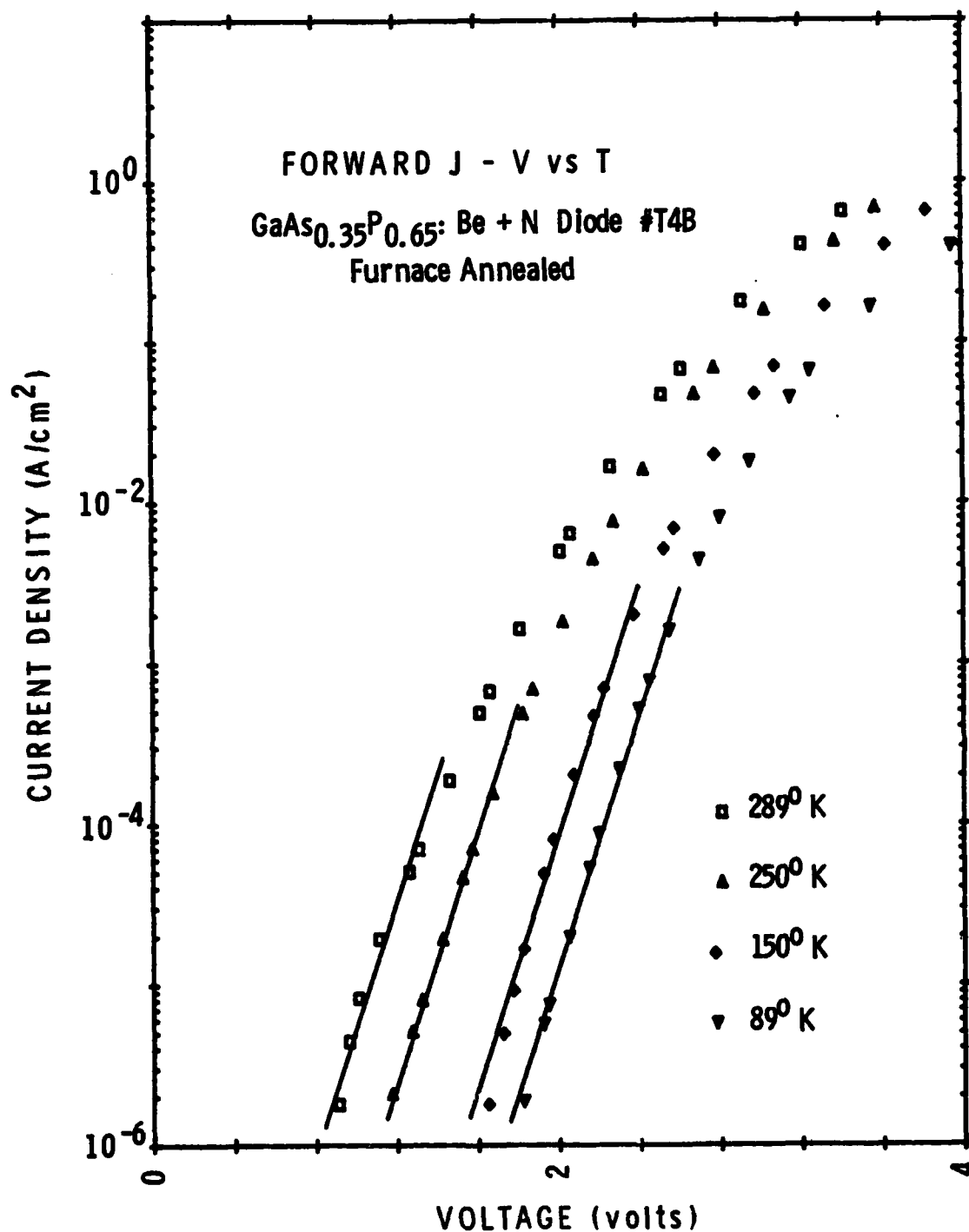


Fig. 5.7. Temperature dependent current density versus voltage characteristics for furnace annealed $\text{GaAs}_{0.35}\text{P}_{0.65}:\text{Be}+\text{N}$ diode #T4B. The solid lines drawn through the low current density portion of each curve are exactly parallel to one another.

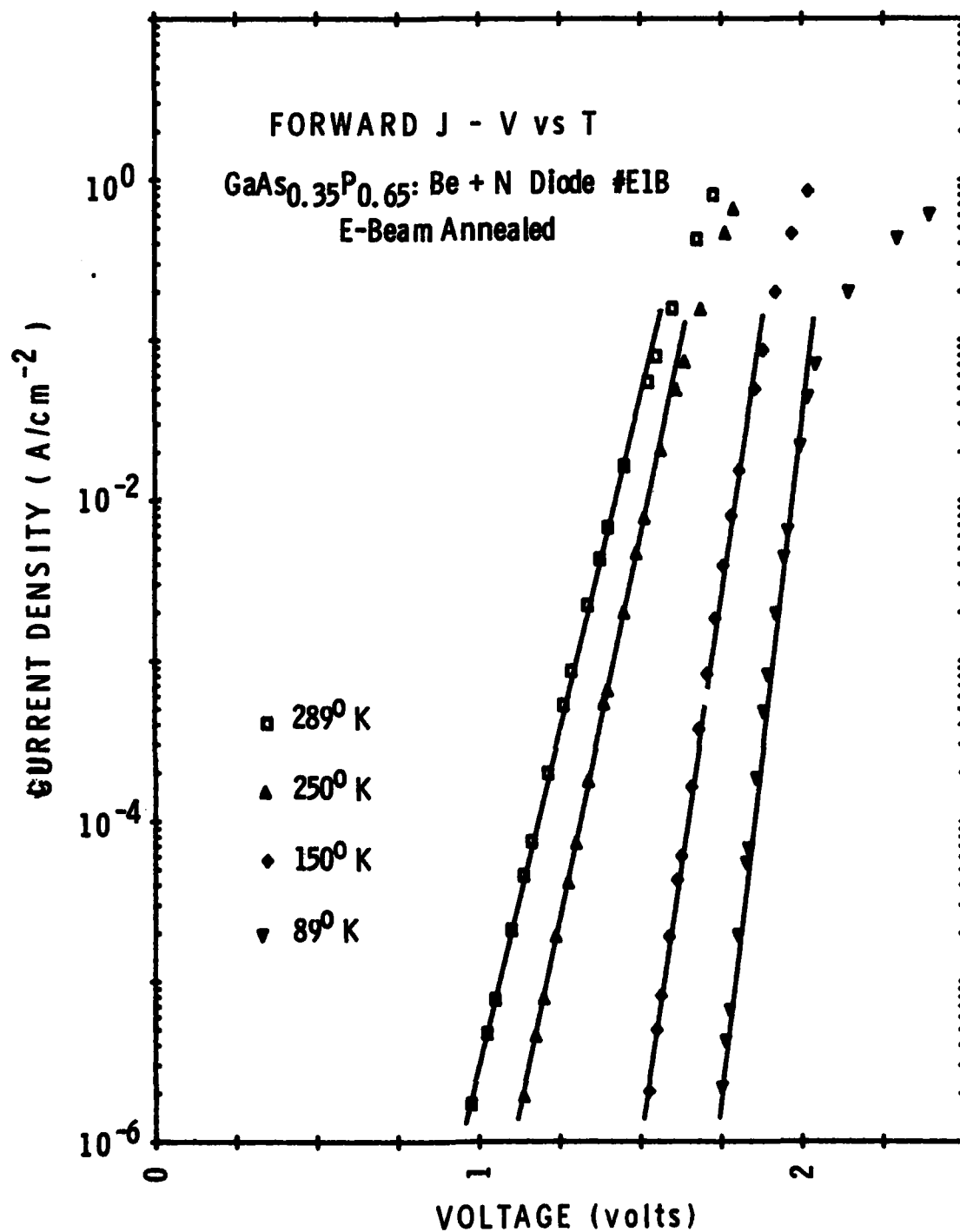


Fig. 5.8. Temperature dependent current density versus voltage characteristics for SLEB annealed device E1B. The solid lines drawn through each characteristic have ideality factors of about 2 at all temperatures. Note the shift in horizontal scale from figure 5.7.

DLTS analysis tends to confirm these findings. The two-diode method described in section 2.3.2 is used. A survey of the electron trap spectra on the n-type side of the junctions of two representative devices is shown in figure 5.9. Here the SLEB and furnace annealed DLTS signal are plotted logarithmically in the same units. Quiescent reverse bias of -10 V and bias reducing pulses of +10 V were used for both devices. Corrections for device area are included so that the relative magnitudes of these curves are indicative of the relative trap densities between devices. Also plotted are survey spectra of Day[71] measured on Al Schottky barriers fabricated on material identical to that used in this study. These data were measured under identical frequency conditions, but not necessarily the same bias. Therefore for comparison, Day's data have been normalized to the peak value of the beam annealed sample's spectra.

The SLEB annealed sample shows a single large peak, while the furnace annealed device shows significant signal all across the scan. The defect spectra of the unimplanted "nitrogen free" Schottky diode shows an amazing similarity to that of the beam annealed device. This defect (E_{81} , $E=E_c-0.41$ eV) has been associated with the dopant sulfur.[118] I conclude that these defects are intrinsic to the material and are not a product of the annealing. The average concentration of this trap can be estimated through [69]

$$N_T = 2 \cdot (N_d - N_a) \cdot \Delta C / C \quad (5.1)$$

to be about $1 \times 10^{16} \text{ cm}^{-3}$.

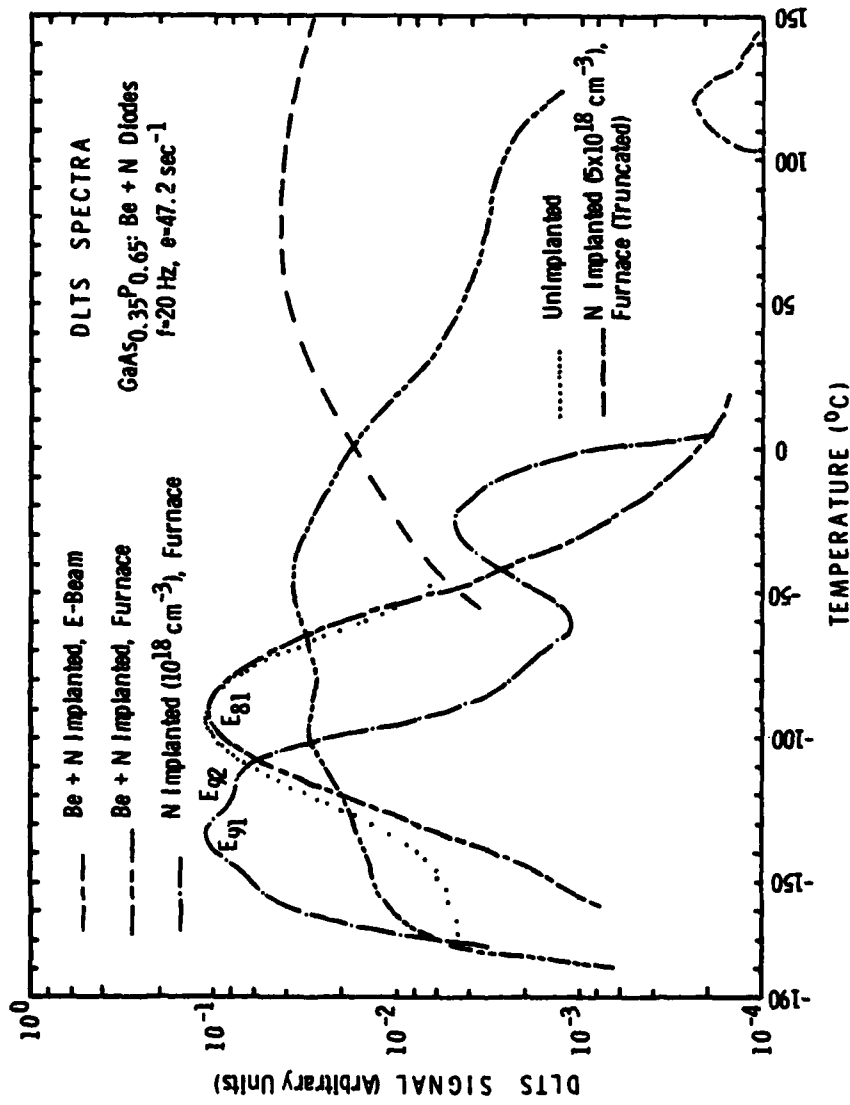


Fig 5.9. DLTS spectra for $\text{GaAs}_{0.35}\text{P}_{0.65}\text{:Be+N}$ diodes processed by SLEB and furnace annealing. Also shown are normalized spectra for unimplanted and N-implanted $x=0.65$ $\text{GaAs}_{1-x}\text{P}_x$ Schottky barrier diodes as measured by Day et al. [71]. Note the logarithmic vertical scale.

AD-A124 428

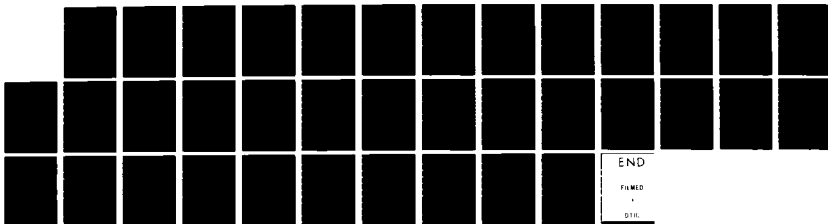
SWEPT LINE ELECTRON BEAM ANNEALING OF ION IMPLANTED
SEMICONDUCTORS(U) ILLINOIS UNIV AT URBANA COORDINATED
SCIENCE LAB K J SODA JUL 82 R-950 N00014-79-C-0424

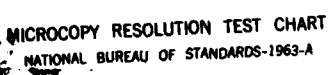
2/2

UNCLASSIFIED

F/G 20/12

NL





The influence of trap signal E_{81} is apparent in the furnace annealed Be + N diode spectra at about -95°C . This device also shows the effects of levels E_{91} and E_{92} observed in a nitrogen implanted Schottky diode.[71] Using equation 5.1 we may estimate the concentration of these defects to be about $2 \times 10^{15} \text{ cm}^{-3}$. Although identification is not absolutely conclusive, it is probable that these signals are due to implanted nitrogen which has diffused out of the original implanted profile and beyond the metallurgical junction during furnace annealing.

Under similar implantation and furnace annealing conditions, Chatterjee[113] found evidence of Be diffusion beyond the as-implanted distribution. This has probably occurred in the furnace annealed devices under study here. They show consistently high voltage drops at large forward currents. The average applied bias required for 10^{-1} A/cm^2 current density is 3.1 V for furnace annealed devices and only 1.5 V for SLEB annealed devices. This tends to indicate a higher sheet resistance due to spreading of the implanted profile. The nitrogen diffusion under consideration here must have proceeded at a faster rate than that of beryllium, since it is detected in the space charge beyond the metallurgical junction. It is significant that no nitrogen-related signal is detected in the SLEB annealed device. This coincides with the finding of the photoluminescence study of section 5.1.

Also observed is a broad signal band in the furnace annealed Be + N diode spectra at temperatures above -50°C . Day[71] has found similar broad defect peaks in nitrogen implanted $x=0.65 \text{ GaAs}_{1-x}\text{P}_x$. This is shown in the truncated $5 \times 10^{18} \text{ cm}^{-3}$ nitrogen implanted spectra of figure 5.9. (This truncated curve is identical to the 10^{18} N -implanted spectra below -80°C .) It is significant to note that the SLEB annealed

device shows no similar radiation damage signal spectra, even though the material was implanted to a factor of two larger peak nitrogen concentration and was beryllium implanted as well. However, we cannot be completely certain that there are no hole traps in the depletion layer since hole injection was not performed during DLTS analysis.

Along this same line of argument, we may not conclude that the defects observed here are directly responsible for the modes of current conduction discussed above. Holes injected into the n-side of these devices will dominate conduction. However, it is interesting that, these furnace annealed Be + N diodes, which possess a continuum of deep levels, also demonstrate tunneling current components. As an order of magnitude estimate, if a 200 Å thick layer contained an average of 1×10^{15} traps/cm³, each would need to recombine a hole-electron pair only once every 300 μ ses to support 10^{-6} A/cm² conduction. This is certainly not an unreasonably short lifetime.

5.2.3 Results and discussion: light emission characteristics

Although the principal purpose of these diodes was the study of redistribution phenomena by electrical techniques, their light emission characteristics also lend some support to the contentions of the preceding section. One would not expect large emission efficiencies in these devices. In this composition, GaAsP has an indirect gap, making bandedge radiative emission a low probability event. Nitrogen acts as an efficient isoelectronic trap of this composition, but the doping profile has not been optimized for maximum efficiency in these devices.

Light intensity (L) versus current data were taken by positioning the devices in a 180° polished aluminum reflector. This reflector was then attached to a Newport Model 880 radiometric detector system. The reflector/detector combination was designed to eliminate all background optical signals. Total optical power measurements were then made as a function of forward DC current. The data are corrected for photodetector response. Two representative device characteristics are shown in figure 5.10. Shown for reference are lines indicating emission proportional to current density and to current density squared.

The slopes of the characteristics shown are representative of all devices annealed by the respective techniques. In general, furnace annealed diodes all show $L \propto J^{n>1}$ behavior while all SLEB annealed devices show $L \propto J^{n \sim 1}$. This trend indicates that some space charge recombination current is contributing to the emission of the furnace annealed diodes, while diffusion current related emission dominates in the SLEB annealed case.[113] This finding is not inconsistent with the J-V measurements discussed earlier. Ohmic losses are considerable at the current densities where light intensity is large enough to measure. Therefore, we are not able to identify the dominant mode of conduction at these current levels. The average external quantum efficiency for the furnace annealed devices is about 5×10^{-6} photons/electron for the furnace annealed diodes and about 2.8×10^{-6} for SLEB annealed devices. A figure of about 2×10^{-5} is expected from published results in furnace diffused $x=0.65$ LEDs without nitrogen doping.[119]

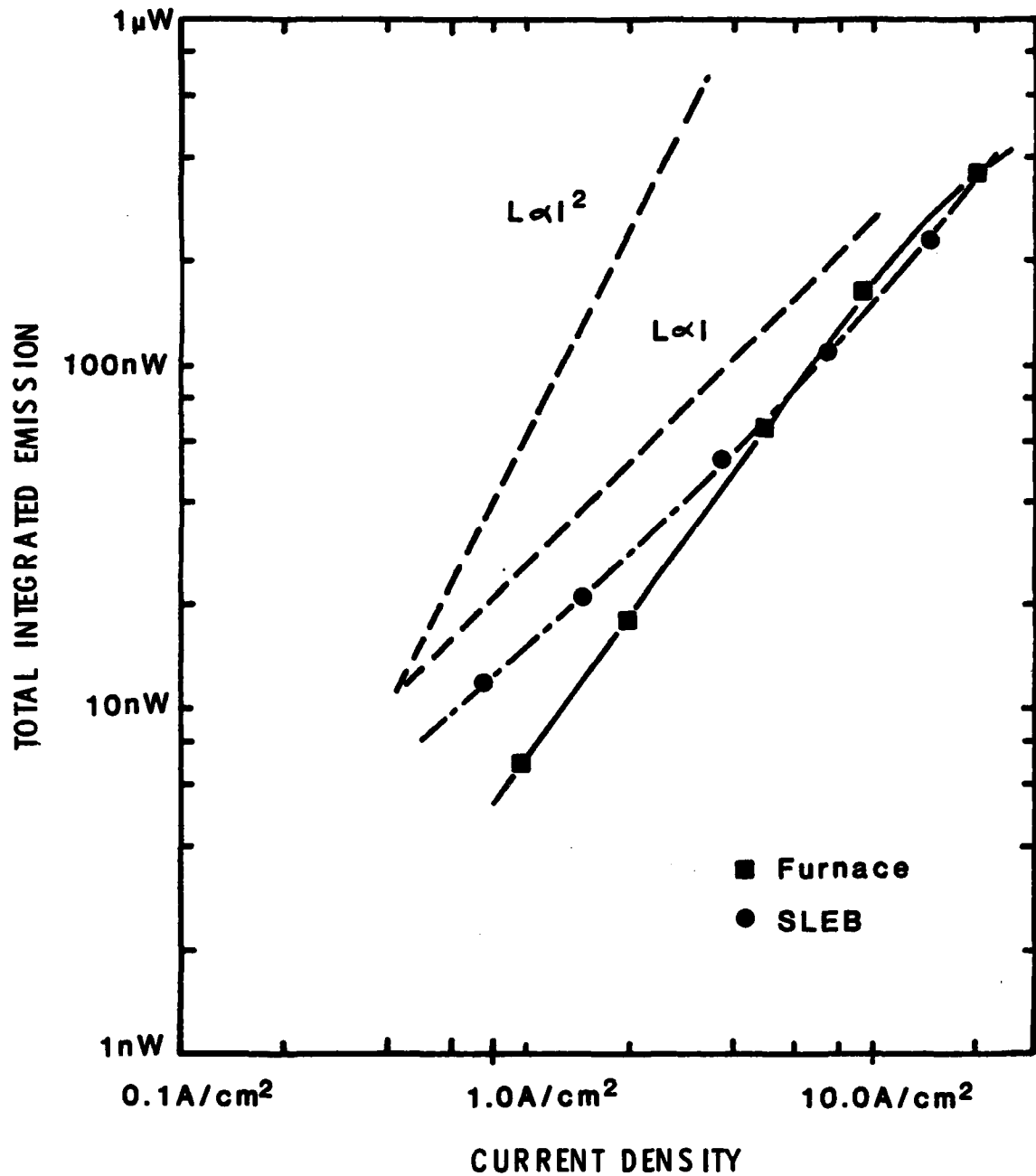


Fig 5.10. Total integrated electroluminescent emission versus current density for representative SLEB and furnace annealed GaAs_{0.35}P_{0.65}:Be+N diodes. Also shown are lines indicating $L \propto I$ and $L \propto I^2$ emission dependence.

Since nitrogen is known to exist in the space charge region of the furnace treated devices, one might expect that some isoelectronic trap emission might be observed. This occurs to some extent. The detection system described in section 5.1 was used to make electroluminescence measurements. The peak emission wavelength of the beam annealed device E1A 6018 \AA (2.060 eV), is consistent with that expected from measurements of Crawford et al. [120] for GaAsP without nitrogen doping. Very little current dependent emission shift is observed in this device from 17 to 40 A/cm^2 . Peak emission for the furnace annealed device T4A is nearly identical to E1A at low bias, but shifts over 70 \AA to 6078 \AA (2.040 eV) at 25 A/cm^2 . This wavelength corresponds roughly with the expected N_x (A-line) nitrogen emission. [120]

The results suggest again that some depletion region nitrogen involvement occurs in the case of the furnace annealed devices. It is possible that the nitrogen related emission also has some component from electrons injected into the p-side of the junction. The reduced doping gradient expected in the furnace annealed case would allow increased electron injection efficiency. The current dependence of the emission tends to confirm this proposition.

5.3 Summary and Conclusions

In this chapter it was demonstrated that SLEB annealing is effective in activating ion-implanted nitrogen in both direct and indirect gap composition $\text{GaAs}_{1-x}\text{P}_x$. Photoluminescence analysis shows that under some conditions nitrogen related emission can actually exceed that attainable by furnace annealing. Photoluminescence profiling demonstrates that SLEB annealing is also effective in restricting the migration of nitrogen and ion-implantation related damage to the original implanted layer.

Although this technique could not be used to verify this finding in $x=0.65$ composition material, electrical studies of Be + N implanted diodes do tend to confirm this finding. J-V, DLTS, L-J, and spectral emission characteristics all can be understood in terms of restricted motion of nitrogen and related damage during annealing. These data also show a lack of Be migration in SLEB treated devices, in contrast with the furnace annealed case.

CHAPTER 6 - SUMMARY AND RECOMMENDATIONS

In this study, the behavior of swept-line electron beam (SLEB) annealed, ion-implanted semiconductors has been studied in some detail. In general it is found that SLEB processing can be an effective and practical alternative to furnace annealing. SLEB treatment has been shown to be effective in annealing implantation related damage in silicon, especially in the as-implanted amorphous-crystalline transition region. This transition region damage has been shown to be resistant even to high temperature furnace annealing, and can act to skew dopant distributions through damage aided diffusion. These migration effects are much less pronounced in SLEB annealed amorphous silicon. SLEB induced activation of boron in this transition region has also been demonstrated. This has not been observed in furnace annealed silicon.

The success of this annealing technique is not limited to silicon. Photoluminescence studies have shown the effectiveness of the SLEB technique in activating implanted nitrogen in $\text{GaAs}_{1-x}\text{P}_x$. In some cases, nitrogen isoelectronic trap related emission intensities are actually larger than those observed from similarly prepared furnace annealed material. Photoluminescence profiling and p-n junction studies show that SLEB annealed material does not display dopant and implantation damage migration effects present in optimally prepared furnace annealed material.

Although this study demonstrates that SLEB annealing is an effective processing technique, a number of questions remain to be answered. The possibility of upscaling a line beam to treat industrial-size wafers was not completely investigated. A prototype electron gun with a four inch beam was built but could not be completely developed. As designed, however, it meets the criteria observed to be necessary

for successful large scale applications. First, it does not rely upon overlap of annealed areas, but rather treats large substrates in a single pass. Experiments with the electron gun described in chapter 2 show that stress marks develop on material adjacent to the beam track on wafers larger than the beam spot. No such stressing appear within the beam heated regions. Also, the long-line gun will deliver all of its energy in a thin (10 mil) line. This should improve annealing uniformity, especially on samples which are non-rectangular. If the sample is heated only within a thin line and is translated fast enough, significant lateral heat flow will not occur. This should limit hot spots on the substrates which occur when broader beam shapes are used.

The results discussed here represent only a relatively limited portion of the range of annealing parameters possible. The fact that annealing quality can exceed that achievable by conventional annealing should stimulate further study. The question of the exact process by which point defects are annealed has not been adequately answered. The degree of permanence of this annealing is unknown. Electric field dependent aging studies of SLEB annealed devices would be a useful investigation. Some obvious differences in the annealing conditions optimal for different semiconductors were noted during these studies. For example, multi-pass annealing depresses the active boron profiles in implanted Si, while it works quite well in implanted GaAsP. The electron range and implantation and damage distributions all undoubtedly affect the ultimate quality of treatment. Some theoretical treatment of beam-material interaction could lead to more predictable processing.

APPENDIX

TRAPSI PROGRAM DOCUMENTATION

TRAPSI is a FORTRAN program for computing defect depth profiles from DLTS measurements at fixed reverse bias and varying bias reducing pulse height. This program is designed for analysis of Schottky barriers fabricated on n-type silicon. Modifications can easily be made for other semiconductor materials. The general operating principles of TRAPSI were described in section 2.3.2.2. The appendix includes specific input requirements, a block by block description of operation, a copy of the program, and a sample output.

A.1 Input Requirements

The TRAPSI program requires three data types: (i) that which relates to the device in general; (ii) C(V) data for determination of fixed charge concentration; and (iii) the DLTS data relative to the defect level in question. Data may be entered indefinitely so that defect peaks of different activation energy and from different devices may be analyzed without restarting the program.

Immediately after execution, the program asks for type i data through the interactive terminal (#5). The data are: (The FORTRAN variable is listed after each entry.)

- a. Descriptive one line comment.
- b. Device area in cm^2 (AREA).
- c. Relative dielectric constant for the semiconductor (ER).

The static value may be used with confidence for Si, Ge and GaAs. Other

values may be more applicable for materials with relatively large dielectric relaxation times [121]

- d. Metal-semiconductor barrier height in volts (DPHBN).
- e. Density of states effective mass for electrons (MDEE) and holes (MDEH).
- f. Donor activation energy in electron volts. (EDON).

The program then asks for the file name which contains the C(V) data (type ii) for the device in question. This file must contain two columns of data, the left hand containing the capacitance in pf, the right hand the corresponding voltage in volts. Up to 100 data pairs may be entered. The last pair of data points in the file must both be zero. All negative voltages should be entered as negative numbers. All effective bias voltages and corresponding steady state capacitances used in the DLTS profiles should be included in this list. All static capacitance data are automatically reduced by 0.68 pf, the average parallel capacitance of a T0-18 header.

Since the fixed charge concentration is inversely proportional to dC/dV , it is important that enough static capacitance data be entered to produce good estimates of $N_d(x)$. The program has an internal criterion that dC/dV be calculated from capacitance values which differ by at least 1% and no more than 10% of the capacitance in question. If this criterion is not met, an error flag appears on the far left side of the output. C(V) data may be entered either largest or smallest value first, but must increase or decrease continuously.

The defect peak related data (type iii) are then entered. They are:

- a. Descriptive comment relative to this defect.
- b. Value of fixed DC reverse bias maintained during profiling, in volts. (VBIAS).
- c. The temperature in $^{\circ}\text{K}$ at which the peak trap signal occurs (TEMP).
- d. Total number of DLTS data points (CPTS).
- e. The value of the bias reducing puls height in volts (VR), the peak recorder displacement in cm (DISP(I)), the sensitivity of the lock-in amplifier in volts (S(I)), and the calibration factor in V/pf (CVF(I)).

The program will ask for data of type e repetitively until the total number of transient points (CPTS) have been recieved. After the last entry, the program will ask if another defect peak is to be analyzed. If so, it will ask for new type iii data. If not, another device may be analyzed by supplying new type i and ii data. A sample interactive output is shown on the following two pages. Entries made by the operator are underlined.

A.2 Block Description

A description of TRAPSI code is presented in this section. The line numbers found at the beginning of each entry correspond to these generated by the DEC FORTRAN editor as shown on the program listing found in section A.3.

Line 100-900: Descriptive comments.

Line 1000-1700: Variable, array and type declaration.

Line 1800-5200: Entry of type i data.

Line 5300-6900: Entry of file name containing C(V) data arrays

EXECUTE TRAPSI.FOR
 LINK: Loading
 [LNKXCT TRAPSI execution]
 ENTER ONE LINE COMMENT

PROFILE FOR E BEAM S. B. #31A
 ENTER DEVICE AREA (CM**2) - 1.32E-3
 ENTER RELATIVE DIELECTRIC CONST. - 11.8
 ENTER DELTA PHI B-N (VOLTS)=0.7
 DENSITY OF STATES EFFECTIVE MASSES OF COMMON
 SEMICONDUCTORS:

	ELECTRONS	HOLES
SI	1.1	.55
GAAS	.068	.5
GAASP 40%	.089	.5
GAASP INDIRECT	1.20	.5
GAP	1.20	.5

MDE FOR ELECTRONS=1.1
 MDE FOR HOLES=.55
 DONOR ACTIVATION ENERGY (EV)=0.044
 ENTER NAME OF C(V) DATA FILE: DEB31A
 C(V) DATA READ A-OK

ENTER 1 LINE COMMENT

PEAK I -- 0.32 EV
 VALUE OF DC BIAS (VOLTS)=-10.00
 ENTER TEMP OF PEAK(DEG K) 183.50
 ENTER DELTA CAP DATA. # OF PTS=1
 BIAS REDUCTING PULSE(VOLTS) V(1)=10.5
 ENTER VAL # 1 OF DISP (CM), SENS. (V), CONVER. FACT. (V/PF)

8.02 .020 .567
 VALUE # 1 OF PULSE= 10.50000
 OF DISP= 8.02000
 OF SENS= 0.02000
 OF CON. FACT.= 0.56700
 OK? -- 1=YES,0=NO: 1
 BIAS REDUCTING PULSE(VOLTS) V(2)=10.00
 ENTER VAL # 2 OF DISP (CM), SENS. (V), CONVER. FACT. (V/PF)

8.19 .020 .530
 VALUE # 2 OF PULSE= 10.00000
 OF DISP= 8.19000
 OF SENS= 0.02000
 OF CON. FACT.= 0.53000
 OK? -- 1=YES,0=NO: 1
 7 0.500 1.23290E+02 6.99860E-02 2.94509E-02 -6.24272E-04
 2.02015E-06 2.29572E+17 3.71246E+12
 BIAS REDUCTING PULSE(VOLTS) V(3)=4.50
 ENTER VAL # 3 OF DISP (CM), SENS. (V), CONVER. FACT. (V/PF)

8.27 .020 .542
 VALUE # 3 OF PULSE= 4.50000
 OF DISP= 8.27000
 OF SENS= 0.02000
 OF CON. FACT.= 0.54200
 OK? -- 1=YES,0=NO: 0
 BIAS REDUCTING PULSE(VOLTS) V(3)=9.5
 ENTER VAL # 3 OF DISP (CM), SENS. (V), CONVER. FACT. (V/PF)

8.27 .020
 VALUE # 30F PULSE= 9.50000
 OF DISP= 8.27000
 OF SENS= 0.02000
 OF CON. FACT.= 0.00000
 OK? -- 1=YES, 0=NO: 0
 BIAS REDUCTING PULSE(VOLTS) V(3)=9.5
 ENTER VAL # 3 OF DISP (CM), SENS. (V), CONVER. FACT. (V/PF)

8.27 .020 .542
 VALUE # 30F PULSE= 9.50000
 OF DISP= 8.27000
 OF SENS= 0.02000
 OF CON. FACT.= 0.54200
 OK? -- 1=YES, 0=NO: 1
 2 0.000 1.00880E+02 9.24775E-02 3.84820E-02 -2.65722E-04
 9.67390E-06 4.28362E+16 6.76468E+12
 BIAS REDUCTING PULSE(VOLTS) V(4)=9.0
 ENTER VAL # 4 OF DISP (CM), SENS. (V), CONVER. FACT. (V/PF)

8.19 .020 .545
 VALUE # 40F PULSE= 9.00000
 OF DISP= 8.19000
 OF SENS= 0.02000
 OF CON. FACT.= 0.36500
 OK? -- 1=YES, 0=NO: 1
 0 -0.500 7.32700E+01 9.36192E-02 4.34221E-02 2.28399E-04
 1.51893E-05 3.92206E+16 1.31186E+13
 0 -1.000 6.04500E+01 9.36192E-02 4.69120E-02 -3.45861E-03
 1.94826E-05 3.92578E+16 3.27133E+14
 IS THERE ANOTHER TRAP PEAK FOR THIS DEVICE?
 1=YES, 0=NO

0
 DO YOU WISH TO ANALYSE ANOTHER DEVICE?
 1=YES, 0=NO

0
 END OF EXECUTION
 CPU TIME: 1.96 ELAPSED TIME: 4:21.17
 EXIT

(CCV(I) and VCV(I)). Included are checks for end of file (line 6000), correction for parallel header capacitance (6300) and file overflow (6600).

Line 7000-7900: Entry of DLTS defect peak related comment.

Line 8000-9100: Entry of quiescent DC reverse bias (VBIAS) and search of corresponding value of static capacitance (CBIAS). If the search fails to find a VCV(I)=VBIAS, then CCV(2)=CBIAS.

Line 9200-10000: Entry of defect peak temperature (TEMP) and number of transient capacitance points. N_c , N_v , and E_g are calculated in the block.

Line 10100-10400: Initialize profile calculation accumulators.

Line 10500: Initialize the main DO loop for profile calculation.

Line 10600-10700: Reset dC/dV flags. (F, F1)

Line 19800: Test for $I = CPTS + 1$. If true, programs skips over transient capacitance data input steps. Note that DLTS data are received only when $1 \leq I \leq CPTS$, and values of trap concentration are calculated only when $2 \leq I \leq CPTS + 1$.

Line 10900-12300: Input and confirm values for the type iiie. (VR, DISP(I), S(I), CVF(I)). Largest values of bias reducing pulse (VR) must be entered first. Allowance is made to correct data if miskeyed. Effective bias (VDELC(I)) is calculated in line 11200.

Line 12400: Calculate Ith value of $\Delta C/C$ (DELCT(I)).

Line 12500: If $I=1$, VDLEC(0)=VBIAS. This step allows calculation of the fixed charge concentration (NB(1)) at the depletion depth corresponding to VBIAS.

Line 21600-13600: Search for the value of VCV(J) which equals VDELC(I-1). If the search fails, the flag F1 is set and the next closest

value of VCV is selected. If the selected value is the first or last in the array, the next value down or up the list is selected. This allows calculation of dC/dV .

Line 13700-15500: Search of the array $CCV(I)$. Beginning with the J th value selected in the previous block, values of CCV are identified which are at least 1% but not more than 10% different from the J th value. If the search does not find values to fit this criteria, flag F is set and first CCV value is selected which is at least 1% different from the J th value. These are designated $CCV(U)$ and $CCV(L)$.

Line 15600-15900: Values of dC/dV ($DCDV$) and fixed charge concentration ($NB(I-1)$) are calculated. Note that during each iteration, the $I-1$ value of NB and NT are calculated.

Line 16000-16300: Debugging print statements for NB and related variables. These lines may be deleted if desired.

Line 16400: In the case $I=1$, skip the blocks concerning trap concentration calculation.

Line 16500-19700: Calculate the location of the Fermi level. This is accomplished by solving the transcendental equation:

$$N_c \exp(-(E_c - E_v)/kT) = N_d / (1 + 2 \exp((E_f - E_d)/kT)) + N_v \exp((E_v - E_f)/kT) \quad A.1$$

The value of E_f is systematically varied until the difference between left and right hand sides of equation A.1 is less than 0.01% of E_g , or until 50 iterations are completed. In the latter case, an error message (line 19200) is printed and the program continues.

Line 19800-21800: This block calculates the depletion width $W(I)$. A basic derivation of the expression used is given here. We begin

with the expression for depletion width for a Schottky barrier:

$$\frac{\epsilon_r \epsilon_0}{q} (V_{bi} - \frac{kT}{q} - V) = \int_0^W x N_b(x) dx \quad A.2$$

where

$$V_{bi} = \phi_{bn} + \Delta\phi - (E_c - E_f)/q \quad A.3$$

Here V_{bi} is the built-in voltage, V is the applied bias, ϕ_{bn} is the Schottky barrier height, $\Delta\phi$ is the image force barrier lowering, N_b is the background fixed charge concentration. We may generalize this equation to:

$$\frac{\epsilon_r \epsilon_0}{q} (V_{bi} - \frac{kT}{q} - V_j) = \sum_{i=1}^l W_i N_b(V_i) [W_i - W_{i-1}] \quad A.4$$

$\lim_{l \rightarrow \infty}$

where $N_b(V_i)$ is the background fixed charge concentration at the depletion depth corresponding to V_i . If we let $(\epsilon_r \epsilon_0)/q = b$ and $V_{bi} - (kT/q) - V_j = v_n$, we may write:

$$bv_1 = N_b(V_1) W_1^2 \quad A.5$$

$$bv_2 = N_b(V_1) W_1^2 + N_b(V_2) [W_2^2 - W_2 W_1]$$

$$bv_n = N_b(V_1) W_1^2 + \dots + N_b(V_n) [W_n^2 - W_n W_{n-1}]$$

Subtracting the last two lines we have:

$$bv_n - bv_{n-1} = N_b(V_n) [W_n^2 - W_{n-1} W_n] \quad A.6$$

which may be solved quadratically for W_n if W_{n-1} and $N_b(V_n)$ are known.

W_1 is given by the first of equations A.5. This scheme is implemented in

lines 20100 through 20600. v_i is calculated in line 20000. In order to obtain the best estimate of W , $\Delta\phi$ is calculated iteratively (DO loop line 19900) based upon the latest value of W_n using:

$$\Delta\phi_i = \sqrt{\frac{qE}{4\pi\epsilon_o\epsilon_r}} = \left(\frac{q^2}{4\pi\epsilon_o^2\epsilon_r^2} \left[\sum_j^{i-1} \{N_b(v_j)W_j + N_b(v_j)(W_j - W_{j-1})\} \right] \right)^{1/2} \quad A.8$$

New values of W_n are found based upon this value of $\Delta\phi_i$. This process continues until the difference between successive calculations of W_n is less than 10^{-9} cm. We assign the term in brackets the label ACCDPT. The value of ACCDPT is accumulated for the next profile step in the variable ADDCP. Print statements 21300-21600 were for debugging and are not active.

Line 21900-22300: Calculate average value of $\delta(\Delta C/C)$ (DELC(I-1)). The I-2, I-1 and Ith values of DELC and VDELC are used. If I=2 or CPTS+1, only the I-1 and CPTS values of DELC and VDELC respectively are used.

Line 22400: Calculate trap concentration. See section 2.3.2.2.

Line 22500-23500: Print results of this profile step.

Line 23600-27700: Termination steps. The program asks if additional profiles or other devices are to be analyzed. If so, execution returns to lines 7000 and 1800 respectively.

This program was specifically written for silicon Schottky barriers. Modification for other semiconductor types requires (1) replacement of line 9700 with an expression to calculate E_g as a function of temperature

and (2) inclusion of ϵ_r in the calculation of $\Delta\phi$ in line 21200. Conversion for p-type semiconductors will require further modest modification.

A.3 TRAPSI Code and Sample Output

A copy of the TRAPSI code and a sample output follow. The sample output corresponds to the example interactive output found in section A.1.

```

00100 C TRAPSI.
00200 C
00300 C
00400 C THIS PROGRAM COMPUTES TRAP DEPTH PROFILES FROM A
00500 C SERIES OF DLTS SCANS OF VARYING BIAS REDUCTING
00600 C PULSE HEIGHTS. PROGRAM IS DESIGNED FOR S.B. ON
00700 C N-TYPE MATERIAL. PROGRAM COMPUTES DEPLETION
00800 C WIDTH FROM FIXED CAPACITANCE DATA WHICH YOU
00900 C MUST PROVIDE. THIS VERSION READS C(V) DATA FROM A DISK FILE.
01000 REAL S(50),CVF(50),DISP(50)
01100 REAL DELC(50),DELCT(50),VB(50),W(0:50)
01200 REAL AREA,ER,MDEE,MDEH,EGEF,VBIAS,CBIAS,VR
01300 REAL MI,NC,NV,EG,EF,EFDIFF,INC,EDONN,DELPHI,DPHIBN,WOLD
01400 REAL ACCDP,DCDV,CTEMP,PT1,PT2,PT3,ACCDPT
01500 REAL A(90),NT(50),NB(0:50),CCV(100),VCV(100),VDELQ(50)
01600 INTEGER CPTS,F,F1,J,K,I,U,L,Q,X,N,F2,NPOINT,O,T
01700 DOUBLE PRECISION B
01800 1 WRITE(5,10)
01900 10 FORMAT(1X,'ENTER ONE LINE COMMENT ',/)
02000 READ(5,20) A
02100 20 FORMAT(80A1)
02200 PRINT 30,A
02300 30 FORMAT(1X,80A1)
02400 WRITE(5,40)
02500 40 FORMAT(1X,'ENTER DEVICE AREA (CM**2) - ',%)
02600 READ(5,50) AREA
02700 50 FORMAT(G)
02800 WRITE(5,60)
02900 60 FORMAT(1X,'ENTER RELATIVE DIELECTRIC CONST. - ',%)
03000 READ(5,50) ER
03100 WRITE(5,65)
03200 65 FORMAT(1X,'ENTER DELTA PHI B-N (VOLTS)=-',%)
03300 READ(5,50) DPHIBN
03400 WRITE(5,70)
03500 70 FORMAT(1X,'DENSITY OF STATES EFFECTIVE MASSES OF COMMON'/
03600 C ' SEMICONDUCTORS: '/
03700 C ' ELECTRONS HOLES'/
03800 C ' SI 1.1 .55'/
03900 C ' GAAS .068 .5'/
04000 C ' GAASP 40% .039 .5'/
04100 C ' GAASP INDIRECT 1.20 .5'/
04200 C ' GAP 1.20 .5'/
04300 WRITE(5,80)
04400 90 FORMAT(1X,'MDE FOR ELECTRONS=-',%)
04500 READ(5,50) MDEE
04600 WRITE(5,90)
04700 90 FORMAT(1X,'MDE FOR HOLES=-',%)
04800 READ(5,50) MDEH
04900 WRITE(5,91)
05000 91 FORMAT(1X,'DONOR ACTIVATION ENERGY (EV)=-',%)
05100 READ(5,50) EDON
05200 WRITE(5,100)
05300 100 FORMAT(1X,'ENTER NAME OF C(V) DATA FILE: ',%)
05400 READ(5,105) B

```

```

05500 105  FORMAT(A9)
05600      OPEN (UNIT=20,DEVICE='DSK',ACCESS='SEQIN',FILE=B)
05700      DO 130 I=1,100
05800      READ(20,110) CTEMP,VCV(I)
05900 110  FORMAT(2G)
06000      IF (CTEMP.EQ.0.AND.VCV(I).EQ.0) 120,125
06100 120  NPOINT=I-1
06200      GO TO 138
06300 125  CCV(I)=CTEMP-0.68
06400 130  CONTINUE
06500      WRITE(5,131)
06600 131  FORMAT(1X,'C(V) DATA FILE TOO LARGE -- CONTINUING ANYWAY',/)
06700      GO TO 140
06800 138  WRITE(5,139)
06900 139  FORMAT(1X,'C(V) DATA READ A-OK',/)
07000 140  WRITE(5,141)
07100 141  FORMAT(1X,'ENTER 1 LINE COMMENT',/)
07200      READ(5,20) A
07300      PRINT 30,A
07400      PRINT 145
07500 145  FORMAT(2X,'F',3X,'V-REV',8X,'S.S. CAP',10X,'EC-EF',
07600      C 12X,'DELPHI',7X,'AVG. D(DC/C)/DV',4X,'DEP. WIDTH',
07700      C 5X,'DOPANT CONCNT.',5X,'TRAP CONCNT.',/,5X,'(VOLTS)',
07800      C 9X,'(PF)',12X,'(EV)',13X,'(VOLTS)',9X,'(1/VOLTS)',
07900      C 9X,'(CM)',12X,'(CM**-3)',10X,'(CM**-3)'
08000      WRITE(5,150)
08100 150  FORMAT(1X,'VALUE OF DC BIAS (VOLTS)=',$,)
08200      READ(5,50) VBIAS
08300      DO 160 I=1,NPOINT
08400      IF (VBIAS.EQ.VCV(I)) GO TO 180
08500 160  CONTINUE
08600      WRITE(5,170)
08700 170  FORMAT(1X,'VBIAS=VCV(I) NOT FOUND. C(VBIAS) SET TO C(2)',/)
08800      PRINT 170
08900      CBIAS=CCV(2)
09000      GO TO 181
09100 180  CBIAS=CCV(I)
09200 181  WRITE(5,190)
09300 190  FORMAT(1X,'ENTER TEMP OF PEAK(DEG K) ',$,)
09400      READ(5,50) TEMP
09500      NC=4.8290E15*MDEE**1.5*TEMP**1.5
09600      NV=4.8290E15*MDEH**1.5*TEMP**1.5
09700      EG=1.16-(7.02E-4*TEMP**2)/(1108+TEMP)
09800 200  WRITE(5,210)
09900 210  FORMAT(1X,'ENTER DELTA CAP DATA. # OF PTS=',$,)
10000      READ(5,50) CPTS
10100      WOLD=0.001E-5
10200      ACCDP=0
10300      ACCDPT=0.0
10400      W(0)=0
10500      DO 510 I=1,CPTS+1
10600      F=0
10700      F1=0
10800      IF (I.EQ.CPTS+1) GO TO 245
10900 219  WRITE(5,220) I

```



```

11000 220 FORMAT(1X, 'BIAS REDUCTING PULSE(VOLTS) V(', I3, ')=' , $)
11100 READ(5, 50) VR
11200 VDEL(I)=VBIAS+VR
11300 WRITE(5, 230) I
11400 230 FORMAT(1X, 'ENTER VAL #', I3, ' OF DISP (CM), SENS. (V),
11500 C CONVER. FACT. (V/FF)' , /)
11600 READ(5, 240) DISP(I), S(I), CVF(I)
11700 240 FORMAT(3(G))
11800 WRITE(5, 235) I, VR, DISP(I), S(I), CVF(I)
11900 235 FORMAT(1X, 'VALUE #', I3, ' OF PULSE=' , F12.5, /, ' OF DISP=' ,
12000 C F12.5, /, ' OF SENS=' , F12.5, /, ' OF CON. FACT.' , F12.5, /,
12100 C ' OK? -- 1=YES, 0=NO: ' , $)
12200 READ (5, 50) T
12300 IF (T.EQ.0) GO TO 219
12400 DELCT(I)=(S(I)*DISP(I)*.5650*.5)/(CVF(I)*CBIAS)
12500 IF (I.EQ.1) VDELC(0)=VBIAS
12600 245 DO 250 J=1, NPOINT
12700 IF (ABS(VDEL(I-1))-VCV(J)).LE.1E-5) GO TO 260
12800 250 CONTINUE
12900 F1=1
13000 MI=VDEL(I-1)
13100 DO 255 J=1, NPOINT
13200 IF (ABS(VDEL(I-1))-VCV(J)).LT.MI) 253, 255
13300 253 MI=ABS(VDEL(I-1)-VCV(J))
13400 Q=J
13500 255 CONTINUE
13600 IF (Q.EQ.NPOINT) J=Q-1
13700 IF (Q.EQ.1) J=2
13800 260 DO 270 K=1, NPOINT
13900 IF (K+J.EQ.NPOINT) GO TO 280
14000 IF (ABS(CCV(K+J)-CCV(J)).GT.(0.01*CCV(J))) GO TO 290
14100 270 CONTINUE
14200 280 U=K+J
14300 F=1
14400 GO TO 310
14500 290 IF (ABS(CCV(K+J)-CCV(J)).LE.(0.1*CCV(J))) 300, 290
14600 300 U=K+J
14700 310 DO 320 K=1, NPOINT
14800 IF (J-K.EQ.1) GO TO 330
14900 IF (ABS(CCV(J-K)-CCV(J)).GT.(0.01*CCV(J))) GO TO 340
15000 320 CONTINUE
15100 330 L=J-K
15200 F=1
15300 GO TO 360
15400 340 IF (ABS(CCV(J-K)-CCV(J)).LE.(0.1*CCV(J))) 350, 330
15500 350 L=J-K
15600 360 DCDV=((ABS(CCV(U)-CCV(J)))/(ABS(VCV(U)-VCV(J)))+
15700 C (ABS(CCV(J)-CCV(L)))/(ABS(VCV(J)-VCV(L))))/2
15800 NB(I-1)=CCV(J)**3/(1.418E-9*ER*AREA**2*DCDV)
15900 IF (NB(I-1).LT.0) NB(I-1)=ABS(NB(I-1))
16000 362 PRINT 361, NB(I-1), DCDV, CCV(J), CCV(U), CCV(L)
16100 WRITE (5, 361) NB(I-1), DCDV, CCV(J), CCV(U), CCV(L)
16200 361 FORMAT(' NB(I-1)=' , 1PE11.3, ' DCDV=' , 1PE11.3, ' CCV(J)=' ,
16300 C 2PE11.3, ' CCV(U)=' , 2PE11.3, ' CCV(L)=' , 2PE11.3)
16400 IF (I.EQ.1) GO TO 510

```

```

16500 363 INC=0.10*EG
16600 F2=1
16700 EF=0.50*EG
16800 DO 390 O=1,50
16900 PT1=EXP(-1.0*(EG-EF)/(8.6171E-5*TEMP))
17000 PT2=NB(I-1)/NC
17100 PT3=(1.0/(1.0+2.0*(EXP((EF-EG+EDON)/(8.6171E-5*TEMP))))))
17200 EFDIFF=PT1-PT2*PT3
17300 IF (0.EQ.1) GO TO 355
17400 GO TO 365
17500 355 SIGN=EFDIFF
17600 GO TO 385
17700 365 IF (F2.EQ.1) 370,380
17800 370 IF ((SIGN.LT.0.AND.EFDIFF.GT.0).OR.(SIGN.GT.0.AND.EFDIFF.
17900 C LT.0)) 371,372
18000 371 F2=-1
18100 SIGN=EFDIFF
18200 INC=0.1*INC
18300 GO TO 372
18400 380 IF ((SIGN.LT.0.AND.EFDIFF.GT.0).OR.(SIGN.GT.0.AND.
18500 C EFDIFF.LT.0)) 381,372
18600 381 F2=1
18700 SIGN=EFDIFF
18800 INC=0.1*INC
18900 372 IF (ABS(EFDIFF).LT.(EG*1E-4)) 400,385
19000 385 EF=EF+(INC*F2)
19100 390 CONTINUE
19200 WRITE(5,395) I,EFDIFF,EG,EF,NC,PT1,PT2,PT3,NB(I-1),DCDV
19300 395 FORMAT(1X,'EF ROUTINE UNABLE TO CONVERGE IN 50 ITERATIONS.
19400 C ',/,1X,'QUIT AT POINT:',I3,2X,'EFDIFF=',E11.3,2X,'EG=',E11.3,
19500 C ' EF=',E11.3,' NC=',E11.3,' PT1=',E11.3,' PT2=',E11.3,
19600 C ' PT3=',E11.3,' NB(I-1)=',E11.3,' DCDV=',E11.3)
19700 PRINT 395,I,EFDIFF,EG,EF,NC,PT1,PT2,PT3,NB(I-1),DCDV
19800 400 IF (I.EQ.2) DELPHI=0.01
19900 DO 450 O=1,50
20000 VB(I-1)=DELPHI+DPHIBN-(EG-EF)-VDEL(I-1)-TEMP*8.6171E-5
20100 IF (I.EQ.2) 410,420
20200 410 W(I-1)=SQRT(ER*5.527E5*VB(I-1)/NB(I-1))
20300 GO TO 440
20400 420 TERM=(SQRT(W(I-2)**2+4.0*5.527E5*ER*(VB(I-1)-VB(I-2))
20500 C /NB(I-1))/2.0)
20600 W(I-1)=W(I-2)/2+TERM
20700 IF (W(I-1).GE.0) 440,430
20800 430 W(I-1)=W(I-2)/2-TERM
20900 440 IF (ABS(W(I-1)-WOLD).LT.0.0001E-5) GO TO 460
21000 WOLD=W(I-1)
21100 ACCDPT=(W(I-1)-W(I-2))*NB(I-1)+ACCDP
21200 DELPHI=4.325E-8*SQRT(ACCDPT)
21300 C WRITE (5,441) W(I-1),VB(I-1),TERM,ACCDPT,DELPHI,VDEL(I-1)
21400 C PRINT 441,W(I-1),VB(I-1),TERM,ACCDPT,DELPHI,VDEL(I-1)
21500 C FORMAT(' W(I-1)=',E12.4,' VB(I-1)=',E12.4,' TERM=',E12.4,
21600 C ' ACCDPT=',E12.4,' DELPHI=',E12.4,' VDEL(I-1)=',E12.4)
21700 450 CONTINUE
21800 460 ACCDP=ACCDPT
21900 IF (I.EQ.2.OR.I.EQ.CPTS+1) 470,480

```

```

22000 470 DELC(I-1)=(DELCT(I)-DELCT(I-1))/(VDELCT(I)-VDELCT(I-1))
22100 GO TO 490
22200 480 DELC(I-1)=(((DELCT(I)-DELCT(I-1))/(VDELCT(I)-VDELCT(I-1))
22300 C ))+((DELCT(I-1)-DELCT(I-2))/(VDELCT(I-1)-VDELCT(I-2))))/2
22400 490 NT(I-1)=ABS(1.809E-6*NB(I-1)*NB(O)*W(I-1)**2*DELC(I-1)/ER)
22500 IF (F.NE.1.AND.F1.NE.1) X=0
22600 IF (F.NE.1.AND.F1.EQ.1) X=1
22700 IF (F.EQ.1.AND.F1.NE.1) X=2
22800 IF (F.EQ.1.AND.F1.EQ.1) X=3
22900 EGEF=EG-EF
23000 WRITE (5,500) X,VDELCT(I-1),CCV(J),EGEF,DELPHI,DELC(I-1),
23100 C W(I-1),NB(I-1),NT(I-1)
23200 500 FORMAT(2X,I1,2X,F7.3,7(5X,1PE12.5))
23300 PRINT 500,X,VDELCT(I-1),CCV(J),EGEF,DELPHI,DELC(I-1),
23400 C W(I-1),NB(I-1),NT(I-1)
23500 510 CONTINUE
23600 PRINT 511,AREA
23700 511 FORMAT(///,1X,"DEVICE AREA=",1PE12.5,"CM**2")
23800 PRINT 512,ER
23900 512 FORMAT(1X,"RELATIVE DIELECTRIC CONST.=",F6.2)
24000 PRINT 513,DPHIBN
24100 513 FORMAT(1X,"DELA PHI B-N=",F6.2,"(VOLTS)")
24200 PRINT 514,MDEE,MDEH
24300 514 FORMAT(1X,"DENSITY OF STATES EFFECTIVE MASS FOR ELECTRONS=",
24400 C F4.2," AND OF HOLES=",F4.2)
24500 PRINT 515,EDON
24600 515 FORMAT(1X,"DONOR ACTIVATION ENERGY=",F5.3,"(EV)")
24700 PRINT 516,TEMP
24800 516 FORMAT(1X,"TEMPERATURE OF PEAK=",F6.2,"(DEG K)")
24900 PRINT 517,VBIAS
25000 517 FORMAT(1X,"DC REVERSE BIAS=",F7.2,"(VOLTS)")
25100 PRINT 520
25200 520 FORMAT(/," FLAG CODES: 0 - NO DIFFICULTY; 1 - COULD
25300 C NOT MATCH A C(V) DATA POINT TO THIS VALUE OF VREV;
25400 C 2 - DELTA C/DELTA V CRITERIA NOT MET;"/," 3 - BOTH
25500 C CONDITIONS 1 & 2 APPLY."/,"//,30X,"CAPACITANCE DATA
25600 C USED ABOVE"/,"/,6X,"V-REV",8X,"HEIGHT",9X,"SENSITIVITY",
25700 C 5X,"CONVER. FACT.",8X,"DELC/C"/,"/,5X,"(VOLTS",9X,
25800 C "(CM)",11X,"(VOLTS)",11X,"(V/PF)",11X,"(PF/V)")
25900 DO 540 M=1,CPTS
26000 PRINT 530,VDELCT(M),DISP(M),S(M),CVF(M),DELCT(M)
26100 530 FORMAT(5X,F7.3,5(5X,1PE12.5))
26200 540 CONTINUE
26300 PRINT 545
26400 545 FORMAT(////////)
26500 WRITE(5,550)
26600 550 FORMAT(1X,"IS THERE ANOTHER TRAP PEAK FOR THIS DEVICE?"/,
26700 C 1X,"1=YES,0=NO"/,/)
26800 READ(5,50) N
26900 IF (N.EQ.1) GO TO 140
27000 WRITE(5,560)
27100 560 FORMAT(1X,"DO YOU WISH TO ANALYSE ANOTHER DEVICE?"/,
27200 C 1X,"1=YES, 0=NO"/,/)
27300 READ(5,50) N
27400 IF (N.EQ.1) 570,580

```

27500	570	CLOSE (UNIT-20, DEVICE='DSK', ACCESS='SEQIN', FILE=B)
27600		GO TO 1
27700	580	END

PROFILE FOR E BEAM S. O. 0314

P	V-REV (VOLTS)	S.O. CAP (PF)	EC-EF (EV)	DELPHI (VOLTS)	AVG. DILOC/CJ/OV (1/VOLTS)	DEP. WIDTH (CM)	DOPANT CONCENT. (CM ⁻³)	TRAP CONCENT. (CM ⁻³)
1	0.500	1.2320E+02	6.9906E-02	2.9450E-02	-6.2827E-04	2.0201E-06	8.2937E+17	3.7124E+12
2	0.000	1.0000E+02	9.2477E-02	3.9402E-02	-2.6372E-04	9.6730E-06	4.8850E+16	9.7646E+12
3	-0.500	1.3270E+01	9.3619E-02	4.3821E-02	2.2939E-04	1.5193E-05	3.9220E+16	1.3110E+13
4	-1.000	6.8450E+01	9.3619E-02	4.6918E-02	-3.4586E-03	1.9482E-05	3.9257E+16	3.2713E+14

DEVICE AREA 1.3200E-03 CM²
 RELATIVE DIELECTRIC CONST. = 11.00
 DELTA PHI S-O 0.75 (VOLTS)
 DENSITY OF STATES EFFECTIVE MASS FOR ELECTRONS = 1.10 AND OF HOLES = .55
 DONOR ACTIVATION ENERGY .844 (EV)
 TEMPERATURE OF PEAK = 103.58 (DEG K)
 DC REVERSE BIAS = -10.00 (VOLTS)

FLAG CODES: 0 = NO DIFFICULTY; 1 = COULD NOT MATCH A C(V) DATA POINT TO THIS VALUE OF VREV; 2 = DELTA C/DELTA V CRITERIA NOT MET;
 3 = BOTH CONDITIONS 1 & 2 APPLY.

V-REV (VOLTS)	HEIGHT (CM)	CAPACITANCE DATA SENSITIVITY (VOLTS)	USED ABOVE CONVER. FACT. (V/PF)	DELTA C (PF/V)
0.500	0.0200E+00	2.0000E-02	3.6700E-01	3.3740E-03
0.000	0.1900E+00	2.0000E-02	3.3800E-01	3.6376E-03
-0.500	0.2700E+00	2.0000E-02	3.4200E-01	3.4866E-03
-1.000	0.1900E+00	2.0000E-02	3.4500E-01	3.4586E-03

REFERENCES

1. M.F. Hamer, A.G. Cullis, D.V. McCaughan, J.M. Keen, H.C. Webber and N.G. Chew, "Laser and Thermal Annealing of Ion-Implanted P-Type Dopants in Silicon", MRS79*, p. 241.
2. M. Tamura, N. Natsuaki, and T. Tokuyama, "Laser Annealing of High Dose P⁺, As⁺, B⁺, O⁺ and C⁺ Implanted Silicon", MRS79*, p.247.
3. W.K. Chu, S.R. Mader, and E. Rimini, "Structure Stability of Arsenic-Implanted Si After Pulsed Laser Irradiation", MRS79*, p. 253.
4. J.S. Williams, A.P. Pogany, D.G. Beanland, D.J. Chivers, M.J. Kenny, A. Rose, and M.D. Scott, "Pulsed Laser Annealing Effects in High Dose Rate Silicon Implants", MRS80⁺, p. 169.
5. G.E.J. Eggermont, Y. Tamminga and W.K. Hofker, "Recrystallization Threshold and Impurity Redistribution for Nd:YAG Laser-Annealed Ion-Implanted Silicon", EC80**, p. 371.
6. H. Baumann, K. Bethge, W. Fuss, E.F. Krimmel, R. Langfeld, A. Lutsch, H. Runge and S. Witkowski, "Laser and Electron Beam Annealing of Buried Layers Produced by MeV Ion Implantation", EC80**, p. 152.
7. N.H. Sheng, M. Mizuta, and J.L. Merz, "EBIC Investigation of Defects Induced in CW Beam-Annealed Si", MRS80⁺, p. 155.
8. J.F. Gibbons, "Applications of Scanning cw Lasers and Electron Beams in Silicon Technology", EC80**, p. 1.
9. N.J. Shah, R.A. McMahon, J.G.S. Williams, and H. Ahmed, "Multiple-Scan E-Beam Method Applied to a Range of Semiconducting Materials", MRS80⁺, p. 201.
10. H. Boroffka, E.F. Krimmel, M. Lindner and H. Runge, "The Origin of Leakage Current of Laser and Electron Beam Annealed Diodes", EC80**, p. 178.
11. J.L. Regolini, N.M. Johnson, R. Sinclair, T.W. Sigmon, and J.F. Gibbons, "Physical Properties of Ion-Implanted SEM-Annealed Silicon", MRS79*, p. 297.

*MRS 79 refers to: Laser and Electron Beam Processing of Materials edited by C.W. White and P.S. Percy, Academic Press, New York, 1980.

+MRS 80 refers to: Laser and Electron-Beam Solid Interactions and Material Processing, edited by J.F. Gibbons, L.D. Hess, and T.W. Sigmon, Elsevier North Holland, New York, 1981.

**EC80 refers to: Laser and Electron Beam Processing of Electronic Materials, edited by C.L. Anderson, G.K. Celler, and G.A. Rozgonyi, the Electrochemical Society Inc, Princeton N.J., 1980

12. D.R. Myers, P. Roitman, S. Mayo, and D. Horowitz, "Electronic Properties of Ion-Implanted Silicon Annealed with Microsecond Dye-Laser Pulses", MRS79*, p. 285.
13. D.K. Sadana, M.C. Wilson, G.R. Booker and J. Washburn, "Regrowth Behavior of Three Different Damage Structures in P^+ Implanted and Subsequently Laser Annealed Si", EC80**, p. 344.
14. F.H. Eisen, "Laser and Electron Beam Annealing of GaAs", MRS79*, p. 309.
15. K. Gamo, Y. Yuba, A.H. Oraby, K. Murakami, S. Namba and Y. Kawasaki, "Laser Annealing Effects in Ion-Implanted GaAs", MRS79*, p. 322.
16. P.A. Pianetta, C.A. Stolte and J.L. Hansen, "Pulsed E-Beam and Ruby Laser Annealing of Ion-Implanted GaAs", p. 328.
17. C.L. Anderson, H.L. Dunlap, L.D. Hess, G.L. Olson, and K.V. Vaidyanathan, "Annealing of Implanted Layers in Compound Semiconductors by Localized Beam Heating Techniques", MRS79*, p. 334.
18. I. Golecki, M.A. Nicolet, J.L. Tandon, P.M. Asbeck, D.K. Sadana, and J. Washburn, "Transient Annealing of GaAs by Electron and Laser Beams", EC80**, p. 467.
19. G.L. Olson, C.L. Anderson, H.L. Dunlap, L.D. Hess, R.A. McFarlane and K.V. Vaidyanathan, "Laser annealing of Ion Implanted Gallium Arsenide", EC80**, p. 467.
20. D.H. Lowndes, J.W. Cleland, W.H. Christie, and R.E. Eby, "Pulsed Ruby Laser Annealing of Zn, Mg, Se, and Si Ion Implants in Semiconducting GaAs", MRS80*, p. 223.
21. P. Pianetta, J. Amano, G. Woolhouse, and C.A. Stolte, "Behavior of Metastable Te Donor Concentrations in Q-Switched Ruby Laser Annealed GaAs", MRS80*, p. 239.
22. G.M. Martin, M. Steers, C. Venger, F. Simondet, and S. Rigo, "Annealing of Te-Implanted GaAs Layers Using a Nd-YAG Laser Beam of Large Dimension", MRS79*, p. 360.
23. K.V. Vaidyanathan, C.L. Anderson, B.M. Barrett, H.L. Dunlap and L.D. Hess, "Pulsed Electron Beam Annealing of Ion Implanted GaAs", EC80**, p. 458.
24. J. Narayan, "Structural Defects in Laser-and Electron-Beam-Annealed Silicon", MRS79*, p. 397.

25. S.P. Weeks, G.K. Cellar, and H.J. Leamy, "Laser Epitaxy over Buried Layers", MRS80⁺, p. 427.
26. G.K. Cellar, H.J. Leamy, D.E. Aspones, C.J. Doherty, T.T. Sheng, and L.E. Trimble, "Laser Crystallization of Deposited Silicon Films", MRS80⁺, p. 435.
27. R. Shah, H.W. Lam, D.L. Crostwait and A.F. Tasch Jr., "MOSFET Fabrication and Physical Characterization of Pulsed Laser Annealed Polysilicon on SiO₂ and Si₃N₄", EC80^{**}, p. 235.
28. J.A. Roth, G.L. Olson, S.A. Kokorowski, and L.D. Hess, "Laser-Induced Solid-Phase Epitaxy of Silicon Films ", MRS80⁺, p. 413.
29. S.C. Danforth, F. Van Gieseon, J.S. Haggerty, and I. Kohatsu, "Laser Induced Controlled Nucleation and Growth Process for Large Grained Polycrystalline Silicon", MRS80⁺, p. 443.
30. R. Fastow, H.J. Leamy, G.K. Celler, Y.H. Wong, and C.J. Doherty, "Laser Growth of Thin Silicon Crystals in Patterned Structures", MRS80⁺, p. 495.
31. K.J. Soda, R.M. DeJule, and B.G. Streetman, "C-V and Capacitance Transient Analysis of Self-Implanted Amorphous Si Layers Regrown by Swept Line Electron Beam (SLEB) Annealing", MRS80⁺, p. 353.
32. L.C. Kimerling, H.J. Leamy and K.A. Jackson, "Photo-Induced Zone Migration (PIZM) in Semiconductors", EC80^{**}, p. 247.
33. D.E. Davies, T.G. Ryan, J.P. Lorenzo, and E.F. Kennedy, "Pulse Diffused N⁺ Layers in GaAs", MRS80⁺, p. 247.
34. H. Ishiwara, S. Saitoh, K. Mitsui, and S. Furukawa, "Laser Annealing of the Double-Hetero Si(111)/CoSi₂/Si Structure", MRS80⁺, p. 525.
35. A. Armigliato, P. De Luca, M. Finetti, and S. Solmi, "Characterization of Al-Si Ohmic Contacts Obtained on Shallow Junctions by Laser and Electron Beam Annealing", MRS80⁺, p. 329.
36. G.M. Martin, A. Mitonneau, M. Cathelin, S. Makran-Ebeid, C. Venger, D. Barbier, A. Laugier, and A. Einstein, "Optimization of Pulsed Annealing Techniques for GaAs Integrated Circuits", MRS80⁺, p. 299.
37. E. Eckhardt, C.L. Anderson, M.N. Colburn, L.D. Hess and R.A. Jullens, "A Comparison of Chemical and Structural Characteristics of In-Au:Ge Ohmic Contacts to GaAs Produced by Bulk Heating and Localized Laser Heating", EC80^{**}, p. 445.

38. S.W. Chiang, Y.S. Liu, and R.F. Reihl, "Formation of SiC, Si₃N₄ by SiO₂ by High-Dose Ion Implantation and Laser Annealing", MRS80⁺, p. 407.
39. Y.I. Nissin and J.F. Gibbons, "CW Laser Annealing of Low Dose Si Implants in GaAs", MRS80⁺, p. 275.
40. P.M. Sandow, "The Effects of Laser Annealing on the Leakage Currents and Recombination Factors of Arsenic Implanted Junctions", EC80^{**}, p. 187.
41. T.O. Sedgwick, P.M. Solomon and H.J. Vollmer, "CW Argon Ion Laser Annealed B and As Implanted Diodes in Oxide Defined Si Devices", MRS80⁺, p. 337.
42. T.O. Yep, R.T. Fulk and R.A. Powell, "Scanned Electron Beam Annealing of Boron-Implanted Diodes", MRS80⁺, p. 345.
43. R.A. McMahon and H. Ahemd, "Scanning Electron Beam Processing of Devices", EC80^{**}, p. 130.
44. E.F. Krimmel, H. Lamatsch, and H. Runge, "Electron Beam Annealing of Implanted Diodes and Polysilicon Layers", EC80^{**}, p. 161.
45. A.C. Greenwald, R. Dolan, and S. Tobin, "Pulsed Electron Beam Processing of Silicon Devices", MRS80⁺, p. 321.
46. N. Natsuaki, T. Miyazaki, M. Ohkura, T. Nakamura, M. Tamura, and T. Tokuyama, "Silicon Bipolar Transistors Fabricated Using Ion Implantation and Laser Annealing", MRS80⁺, p. 375.
47. T.C. Teng, Y. Shiau, Y.S. Chen, C. Skinner, J. Peng, and L. Palkuti, "Characterization of Ion-Implanted SiO₂ Properties Applicable to Laser Processing", MRS80⁺, p. 391.
48. J.D. Speight, A.E. Glaccum, D. Machin, R.A. McMahon, and H. Ahemd, "Scanning E-Beam Annealing of MOS Devices", MRS80⁺, p. 383.
49. J.C. Muller, P. Stiffert, J. Michael and E. Fabre, "Characterization of Silicon Layers Implanted by Low Speed Molecular Ions and Annealed by a Pulsed Laser", MRS79*, p. 278.
50. R. Stuck, E. Fogarassy, A. Grob, J.J. Grob, J.C. Muller and P. Siffert, "Properties of P-N Junctions Prepared on Antimony Covered Silicon by Laser Induced Diffusion", EC80^{**}, p. 193.
51. M. von Allmen, "Coupling of Beam Energy in Solids", MRS79*, p. 6.

52. H.E. Bishop, "Electron-Solid Interactions and Energy Dissipation", from Quantative Scanning Electron Microscopy, edited by B.D. Holt, M.D. Muir, P.R. Grant and I.M. Boswana, Academic Press, p. 41, 1974.
53. T.E. Everhart and P.H. Hoff, "Determination of Kilovolt Electron Energy Deposition vs Penetration Distance in Solid Material", Joru. of Appl. Phys., 42, p. 5837, 1971.
54. G.G. Bentini, R. Balloni, P.G. Merli, L. Pedulli, I. Vecchi and F. Zignoni, "Characterization of Implanted Layers after Laser and Electron Beam Annealing", MRS79*, p. 272.
55. J.L. Benton, L.C. Kimerling, G.L. Miller, D.A.H. Robinson, and G.K. Celler, "Electronic Properties of Laser Annealed Silicon", AIP50⁺⁺, p. 543.
56. J.L. Benton, C.J. Doherty, S.D. Ferris, L.C. Kimerling, H.J. Leamy and G.K. Celler, "Post Illumination Annealing of Defects in Laser Processed Silicon", MRS79*, p. 430.
57. E. Rimini, P. Baeri, S.U. Compisano and G. Foti, "Ruby Laser Pulse Effect in Ion-Implanted Semiconductors", AIP50⁺⁺, p. 259.
58. E.F. Kennedy, S.S. Lau, I. Golecki, J.W. Mayer, W. Tseng, J.A. Minnucci, and A.R. Kirkpatrick, "Pulsed Electron Beam Annealing of Ion-Implanted Silicon Layers", AIP50⁺⁺, p. 470.
59. C. Hill, "Laser Annealing of Device Sturctures", EC80^{**}, p. 26.
60. M. Mizuta, N.H. Sheng, J.L. Merz, A. Lietoila, R.B. Gold and J.F. Gibbons, "Electron-Beam-Induced Current Investigation of CW Laser Annealed Silicon", Appl. Phys. Lett., Vol. 37, p. 154, 1980.
61. D.E. Davies, Rome Air Development Center, USAF, Private Communication.
62. K.L. Brown and G.W. Tautfest, "Faraday-Cup Monitors for High-Energy Electron Beams", Review of Sci. Instrum., 27, 696, 1956.
63. H. Bruining, Physics and Applications of Secondary Electron Emission, Pergamon Press, New York, 1954.
64. E.J. Sternglass, "Backscattering of Kilovolt Electrons from Solids", Phys. Rev., 95, 345, 1954.
65. M.Y. Tsai, "Studies of High Dose Ion-Implantation in Silicon", Phd Thesis, Univ. of Illinois, NTIS #ADA069779, 1978.

⁺⁺AIP 50 refers to: Laser-Solid Interactions and Laser Processing-1978, edited by S.D. Ferris, H.J. Leamy and J.M. Poate. American Institute of Physics, New York, 1979.

66. JEOL JSM 35-SDC Selective Area Diffraction Components Instruction Manual.
67. D.C. Joy, "Electron Channeling Patterns in the SEM", Chapter 6 from Quantitative Scanning Electron Microscopy, edited by B.D. Holt, M.D. Muir, P.R. Grant and J.M. Boswana, Academic Press, London, p. 131, 1974.
68. D.V. Lang, "Deep-level Transient Spectroscopy: A New Method to Characterize traps in semiconductors", J. of Appl. Phys., 45, p. 3023, 1974.
69. G.L. Miller, D.V. Lang and L.C. Kimerling, "Capacitance Transient Spectroscopy", Ann. Rev. Mater. Sci., p. 377, 1977.
70. D.S. Day, M.J. Helix, K. Hess and B.G. Streetman, "Deep level transient spectroscopy for diodes with large leakage currents", Rev. Sci. Instrum., 50, 1571, 1979.
71. D.S. Day, "Studies of Electron Traps in GaAs and GaAsP by Deep Level Transient Spectroscopy", Phd Thesis, Univ. of Illinois, 1980.
72. D.S. Day, M.Y. Tsai, B.G. Streetman and D.V. Lang, "Deep-level transient spectroscopy: System effects and data analysis", J. of Appl. Phys., 50, 5093, 1979.
73. D.V. Lang, "Fast capacitance transient apparatus: Application to ZnO and O centers in GaP p-n junctions", J. of Appl. Phys., 45, p. 3014, 1974.
74. W.V. McLevige, P.K. Chatterjee and B.G. Streetman, "Versatile double A.C. Hall Effect system for profiling impurities in semiconductors", J. Phys. E. Sci. Instrum., 10, 335, 1972.
75. L.J. van der Pauw, "A method of measuring specific resistivity and Hall effect of discs of arbitrary shape", Phillips Res. Repts., 13, 1, 1958.
76. J.W. Mayer, O.J. Marsh, G.A. Shirfrin and R. Baron, "Ion-Implantation of Silicon: II Electrical evaluation using Hall-effect measurements", Can. J. Phys., 45, 4073, 1967.
77. K.B. Wofstirn, "Hole and Electron mobilities in doped silicon from radiochemical and conductivity measurements", Phys. Chem. Solids, 16, p. 279, 1960.
78. L. Csepregi, J.W. Mayer and T.W. Sigmon, "Channeling effect measurements of the recrystallization of amorphous Si layers on crystal Si", Phys. Letts., 54A, 157, 1975.

79. L. Csepregi, E.F. Kennedy, T.J. Galligher, J.W. Mayer and T.W. Sigmon, "Reordering of amorphous layers of Si implanted with ^{31}P , ^{75}As and ^{11}B ions", J. Appl. Phys., 48, 4234, 1977.
80. M.Y. Tsai, B.G. Streetman, P. Williams and C.A. Evans Jr., "Anomalous migration of fluorine and electrical activation of boron in BF_2^+ implanted silicon", Appl. Phys. Letts., 32, 144, 1978.
81. M.Y. Tsai and B.G. Streetman, "Recrystallization of implanted amorphous silicon layers. I. Electrical properties of silicon implanted with BF_2^+ or $\text{Si}^+ + \text{B}^{++}$ ", J. Appl. Phys., 50, 183, 1979.
82. M.Y. Tsai, D.S. Day, B.G. Streetman, P. Williams, and C.A. Evans Jr., "Recrystallization of implanted amorphous silicon layers. II. Migration of fluorine in BF_2^+ -implanted silicon", J. of Appl. Phys., 50, 188, 1979.
83. L.C. Kimerling, "Influence of deep traps on the measurement of free-carrier distributions in semiconductors by junction capacitance techniques", J. of Appl Phys., 45, 1839, 1974.
84. J. Krynicky and J.C. Bourgoin, "Defect Annealing in Phosphorus Implanted Silicon: A DLTS Study", Appl. Phys., 18, 275, 1979.
85. L.C. Kimerling, "New Developments in Defect Studies in Semiconductors", IEEE Trans. Nuc. Sci., NS-23, 1497, 1976.
86. L.C. Kimerling, P. Blood and W.M. Gibson, "Defect states in proton-bombarded silicon at $T < 300^\circ\text{K}$ ", Inst. Phys. Conf. Ser., 46, 273, 1979.
87. L.C. Kimerling and J.L. Benton, "Defects in Laser Processed Semiconductors", MRS79*, p. 385.
88. K.L. Wang, Y.H. Lee and J.W. Corbett, "Defect distribution near the surface of electron-irradiated silicon", Appl. Phys. Letts., 33, 547, 1978.
89. P. Baruch, "Radiation defects and impurity diffusion in Si", Inst. of Phys. Conf. Procd., 31, 126, 1977.
90. J.S. Williams, "Comparison of Laser and Furnace Annealing Mechanisms for Regrowth of Ion-Implanted Amorphous Silicon Layers", EC80**, p. 249.
91. T. Yu, K.J. Soda, and B.G. Streetman, "Annealing of nitrogen-implanted $\text{GaAs}_{1-x}\text{P}_x$ by a swept-line electron beam", J. Appl. Phys., 51, 4399, 1980.
92. A.C. Greenwald, A.R. Kirkpatrick, R.G. Little and J.A. Minnucci, "Pulsed-electron-beam annealing of ion-implantation damage", J. Appl. Phys., 50, 783, 1979.

93. R.A. McMahon and H. Ahmed, "A Scanning Electron Beam Annealing System", EC80^{**}, p. 123.
94. R.S. Nelson, "The Clustering of Defects in Irradiated semiconductors", Inst. of Phys. Conf. Procd., 31, 164, 1977.
95. M.D. Matthews and S.J. Ashley, "The dynamic observation of the formation of defects in silicon under electron and proton irradiation", Philos. Mag., 27, 1313, 1973.
96. V.N. Mordkovich, S.P. Solov'ev, E.M. Temper and V.A. Kharchenko, "Radiation annealing of defects in neutron bombarded silicon", Sov. Phys. Semi. (USA), 8, 666, 1974.
97. N.N. Gerasimenko, "Monocrystal-amorphous radiation induced transitions", Inst. of Phys. Conf. Ser., 31, p. 164, 1977.
98. H.L. Fraser, "Threshold Voltage for Damage in Si Under Electron Bombardment", Scripta Metallurgica, 11, 47, 1977.
99. S. Hinckley, H. Mora and J.C. Kelly, "Subthreshold Defect Generation and Annealing in Silicon by Intense Electron Beam Bombardment", Phys. Stat. Solidi, A, 51, 419, 1979.
100. L.J. Cheng, and J.W. Corbett, "Defect Creation in Electronic Materials", Procd. of the IEEE, 62, 1208, 1974.
101. J.C. Irvin, "Resistivity of Bulk Silicon and Diffused Layers in Silicon", Bell Sys. Tech. Jour., 41, 387, 1968.
102. S.M. Sez and J.C. Irvin, "Resistivity, Mobility and Impurity Levels in GaAs, Ge and Si and 300° K", Sol. State Elect., 11, 599, 1968.
103. D.K. Brice, Ion Implantation Range Energy Deposition Distributions, Vol. I, IFI/Plenum Data Co., N.Y., 1975.
104. J. Lindhard, M. Scharff and H. Schiott, "Range Concepts and Heavy Ion Ranges. Notes on Atomic Collisions. II.", K. Danske Vidensk. Selsk. Mat. Fys. Med. (Denmark), 33, 39, 1963.
105. D.J. Wolford, B.G. Streetman, W.Y. Hsu, J.D. Dow, R.J. Nelson and N. Holonyak, Jr., "Evidence for Radiative Recombination in GaAs_{1-x}P_x: N (0.28<x<0.45) Involving an Isolated Nitrogen Impurity State Associated with the Γ_1 Minimum", Phys. Rev. Letts., 36, 1400, 1976.
106. R.J. Nelson, N. Holonyak, Jr., J.J. Coleman, D. Lazarus, W.O. Groves, D.L. Keune, M.G. Craford, D.J. Wolford and B.G. Streetman, "The Effects of Composition and Pressure on the Nitrogen Isoelectronic Trap in GaAs_{1-x}P_x", Phys. Rev. B., B14, 685, 1976.

107. D.J. Wolford, B.G. Streetman, R.J. Nelson and N. Holonyak Jr., "Stimulated Emission on N ("A-line") Recombination Transitions in N-Doped GaAs_{1-x}P_x", Appl. Phys. Letts., 28, 711, 1976.
108. D.J. Wolford, B.G. Streetman, W.Y. Hsu, J.D. Dow, R.J. Nelson and N. Holonyak Jr., "Identification of Recombination Luminescence Transitions in N-Doped GaAs_{1-x}P_x", Solid State Comm., 19, 741, 1976.
109. R.E. Anderson, D.J. Wolford and B.G. Streetman, "Nitrogen Implantation in GaAs_{1-x}P_x. II. Annealing Properties", J. Appl. Phys., 48, 2453, 1977.
110. D.J. Wolford, R.E. Anderson, and B.G. Streetman, "Nitrogen Implantation in GaAs_{1-x}P_x. I. Photoluminescence Properties", J. Appl. Phys., 48, 2442, 1977.
111. E.W. Williams and R.A. Chapman, "Temperature Dependence of Photoluminescence in Cadmium-Doped Epitaxial GaAs", J. Appl. Phys., 38, 2547, 1967.
112. J. Chevallier, H. Mariette, D. Diguët and G. Loibland, "Direct Experimental Observation of Band-Structure Effects in GaP As_{1-x}N Alloys by Radiative Lifetime Measurements", Appl. Phys. Letts., 28, 375, 1976.
113. P.K. Chatterjee, "Acceptor Behavior of Implanted Beryllium in Gallium Arsenide and Gallium Arsenide Phosphide", Phd Thesis, University of Illinois, Report # UILU-ENG 76-2209, 1976.
114. M.J. Helix, K.V. Vaidyanathan, B.G. Streetman, H.B. Dietrick and P.K. Chatterjee, "RF Plasma Deposition of Silicon Nitride Layers", Thin Solid Films, 55, 143, 1978.
115. M.R. Lorenz and M. Pilkuhn, "Preparation of Solution-Grown Epitaxial p-n Junctions in GaP", J. Appl. Phys., 37, 4094, 1966.
116. R.J. Archer, R.C.C. Leite, A. Yariv, S.P.S. Porto and J.M. Whelan, "Electron-hole and Electron-impurity Band Tunneling in GaAs Luminescent Junctions", Phys. Rev. Letts., 10, 483, 1963.
117. A.H. Herzog, W.O. Groves and M.G. Crawford, "Electroluminescence of Diffused GaAs_{1-x}P_x Diodes with Low Donor Concentrations", J. Appl. Phys., 40, 1830, 1969.
118. R.A. Cravan and D. Finn, "The Sulfur-related Trap in GaAs_{1-x}P_x", J. Appl. Phys., 50, 6334, 1979.

119. J.C. Cambell, N. Holonyak Jr., M.G. Crawford and D.L. Keune, "Band Structure Enhancement and Optimization of Radiative Recombination in $\text{GaAs}_{1-x}\text{P}_x\text{:N}$ ", J. Appl. Phys., 45, 4543, 1974.
120. M.G. Crawford, R.W. Shaw, A.H. Herzog and W.O. Groves, "Radiative Recombination Mecahnisms in GaAsP Diodes With and Without Nitrogen Doping", J. Appl. Phys., 43, 4075, 1972.
121. S.M. Sez, Physics of Semiconductor Devices, Wiley-Interscience, New York, 1969.
122. A.J. Rosa, "Luminescent and Electrical Properties of Sodium Implanted Zinc Selenide Phd Thesis, University of Illinois 1975.

VITA

Kenneth James Soda was born 3 January, 1952 in Chicago, Illinois. He entered the United States Air Force Academy in June of 1969. In 1973, he completed his studies for the Bachelor of Science degree in Electrical Engineering. He was a distinguished graduate and received a regular Air Force Commission. He then attended the University of California, Berkeley, earning a Master of Science degree, also in Electrical Engineering in 1974.

From 1974-1977, then Lieutenant Soda was assigned to the Air Force Weapons Laboratory, Kirtland AFB, NM. Here his duties centered upon nuclear radiation effects on electro-optic devices and fiber optic materials. Upon completion of this assignment, he was awarded the Air Force Commendation Medal.

In August of 1977, he began studies at the University of Illinois at Urbana-Champaign. He is presently assigned to the Rome Air Development Center, Hanscom AFB, MA. He currently holds the rank of Captain.

Mr. Soda is a member of the Institute of Electrical and Electronics Engineers.